

Wet compression with a twin screw compressor prototype

K. Guðmundsdóttir

Technische Universiteit Delft



WET COMPRESSION WITH A TWIN SCREW COMPRESSOR PROTOTYPE

by

K. Guðmundsdóttir

4631617

in partial fulfillment of the requirements for the degree of

Master of Science
in Mechanical Engineering

at the Delft University of Technology,
to be defended publicly on Tuesday August 21, 2018 at 14:00 .

Supervisor:	Dr. ir. C.A. Infante Ferreira	TU Delft
Thesis committee:	Dr. O. Moulton,	TU Delft
	Dr. ir. R. Pecnik,	TU Delft
	Ir. V. Gudjonsdottir,	TU Delft

This thesis is confidential and cannot be made public until August 21, 2023.

An electronic version of this thesis is available at <http://repository.tudelft.nl/>.

ABSTRACT

Energy consumption has been steadily increasing over the past years and many studies have been done on possible future trends. Most studies agree that this increase of energy needs is not slowing down anytime soon. Heat pumps can be used to reduce energy requirements in some sectors of the industry. By improving components of the heat pump cycle, such as the compressor, it is possible to get smaller energy needs to combat the constantly rising energy consumption in the world. With this study the possibility of improving operation on a twin screw compressor, that could lead to less energy usage, will be examined.

First a literature study was conducted where various thermodynamic property and compressor models were reviewed. While there are many thermodynamic models available for an ammonia-water mixture not all focus on properties such as temperature, enthalpy and pressure, which were among the main properties needed for this study. For convenience a model was chosen that was already converted to fit with a software such as Matlab. The next part was more important, to explore possible models to build on for the compressor. Some models were too simple to get the desired results, while others were too complex for the amount of details known. The models used a couple different methods, which could be partly combined.

The main objective of this study was to develop a quick model for an oil free twin screw compressor. The computational time of the model was to be kept as low as possible so that the model could be used for quick estimations and optimizations of the process. This was done by using a simple geometry focusing on the volume curve and port sizes, that can easily be changed by scaling the process as needed. The leakage paths follow the same pattern and can also be scaled for different projects. The whole model was done in Matlab, with thermodynamic properties of the ammonia water mixture implemented by [Rattner and Garimella](#) and in some cases the physical properties were imported by Refprop through Fluidprop. The model covers all stages of the compressor process: suction, compression and discharge phase. The model was validated by comparing general trends seen in oil free twin screw compressors using different working fluids.

The quick computational time allows for many different features to be examined in a short time to get a general idea of how the compressor would react to them. While using models with more detailed geometries one test can take hours compared to minutes with the model of this study. From the model search it was concluded that for this level of model a finite volume method would be the best option for this study. Various methods were explored to solve the governing equations, counting a few integrated solvers in Matlab and some numerical procedures for ODEs. The method that was chosen as the best for this system was the Euler method. All methods had in common was that the step size needed to be very small, for smaller geometries they needed to be even smaller in some sections of the compressor. To account for that the model was adjusted to accept variable steps. The variable steps allowed for smaller steps around the beginning and end of compression and thus lowering computational time. The main output of the model is the efficiency of the compressor and the Coefficient Of Performance (COP) of the cycle.

The model was tested for various operating conditions to determine how it, and the compressor, would respond. The main result is that the vapor quality should be kept rather low, around 40%, to achieve the highest efficiencies. The performance is also better with higher rotational speeds, however higher speeds also mean more mass flow through the whole system and increased mechanical losses. This means that up to a certain point the rotational speed can be increased until it starts decreasing the efficiency. It was also seen that the ideal ammonia concentration is around 33-35wt%, at higher or lower values the coefficient of performance decreases.

As some preliminary work for future experiments the experimental cycle was set up using pumps and heat exchangers to simulate the compressor. This included verifying the calibrations of sensors, confirming that correct data was read from sensor to LabView and getting the system leakproof. This cycle was also implemented in Matlab so that the cycle could be tested. From those tests the conclusion is that after going through the separator and the vapor and liquid streams being mixed back together the temperature decreases around

60 degrees usually, and there is a small increase in vapor quality around 2-3%.

Later on when the compressor will be connected this data can predict how much the outlet of the compressor should be cooled down in order for the inlet of the compressor to be acceptable.

ACKNOWLEDGEMENTS

First, I would like to thank my supervisors, Dr. ir C.A. Infante Ferreira and Ir. V. Guðjónsdóttir for their exemplary supervision and excellent help. While our weekly meetings seemed daunting at first the guidance from them was priceless. In our meetings, you helped me by reflecting on my work and kept me on track, from start to finish.

My gratitude for all the friends I have made here in Delft and for helping me get some well earned distractions when needed, both during work hours and outside of them. Thanks to my family for always believing in me, even when I didn't. My gratitude for all the phone calls and messages from Iceland, it really helped me think about something else for a change. Special thanks to my closest family and boyfriend for all their help and all the visits where you made me feel like a queen.

Finally, I would like to thank TU Delft, the Energy and Process Department, all the teachers, staff and fellow students for making this journey what it was.

*K. Guðmundsdóttir
Delft, August 2018*

CONTENTS

Nomenclature	ix
1 Introduction	1
1.1 Background	1
1.2 Research question	4
1.3 Approach to problem	4
2 Theory	5
2.1 Thermodynamic properties of Ammonia-Water mixture	5
2.1.1 Rattner and Garimela / Ziegler and Trepp equations	5
2.1.2 Free enthalpy model	7
2.1.3 Patek and Klomfar equations	8
2.1.4 Comparison	8
2.2 Compressor	9
2.2.1 Single screw compressor	9
2.2.2 Twin screw compressor	10
3 Model	11
3.1 Wet compression with complex geometry	11
3.2 Thermodynamic model	14
3.2.1 Large temperature glide in resorber	15
3.2.2 Large temperature glide in desorber	15
3.3 General model	15
3.4 Model using a volume curve	18
3.5 Suction and discharge ports	20
3.6 Possible leakage paths	23
3.7 Model comparison	26
4 Implementation of compressor model	29
4.1 Control Volume	30
4.2 Implementation	30
4.3 Validation of the model	34
5 Model Results	37
5.1 Effect of ammonia concentration	37
5.2 Effect of clearances	40
5.3 Effect of discharge pressure	42
5.4 Effect of vapor quality at suction	44
5.5 Effect of rotational speed	46
6 Experimental setup	51
6.1 Preparing the experiments	52
6.2 Matlab prediction cycle	53
6.3 Cycle predictions	55
7 Discussion	59
7.1 Performance of compressor	59
7.2 Model Discussion	66
8 Conclusions and recommendations	69
8.1 Conclusions	69
8.2 Recommendations	70

A Appendix	71
A.1 Coefficients used for free enthalpy method by Mejbri and Bellagi	71
A.2 Coefficients for Patek and Klomfar correlations	72
Bibliography	75

NOMENCLATURE

A	Cross sectional area	m^2
a	Velocity	ms^{-1}
A_c	Distance between rotor centers	mm
a_s	Speed of sound	ms^{-1}
C	Flow coefficient	
\bar{C}_p	Isobaric molar heat capacity	$Jmol^{-1}K^{-1}$
C_p	Isobaric heat capacity	$Jkg^{-1}K^{-1}$
d	Outside diameter of rotor	mm
F	Load	N
G	Molar free enthalpy	$Jmol^{-1}$
g_L	Gibbs energy	Jkg^{-1}
H	Total enthalpy of homogeneous working mixture	J
h	Specific enthalpy	Jkg^{-1}
\bar{h}	Molar enthalpy	$kJkmol^{-1}$
l	Length of rotor	mm
M	Molar mass	$kgkmol^{-1}$
m	Mass of mixture	kg
\dot{m}	Mass flow	$kg s^{-1}$
n	Compressor rotational speed	rpm
n_m	Number of lobes of male rotor	
p	Pressure	Pa
Q	Energy	J
q	Vapour quality	
\dot{Q}	Rate of heat transfer	Js^{-1}
R	Ideal gas constant	$Jmol^{-1}K^{-1}$
r	Radius of shaft	mm
s	Specific entropy	$Jkg^{-1}K^{-1}$
\bar{s}	Molar entropy	$kJkmol^{-1}K^{-1}$
T	Temperature	K

t	Time	s
T_b	Arbitrary factor of temperature reduction	
U	Heat transfer coefficient	$Jm^{-2}K^{-1}$
u	Internal energy	Jkg^{-1}
V	Volume	m^3
v	Specific volume	m^3kg^{-1}
\bar{v}	Molar volume	m^3kmol^{-1}
\dot{V}	Volume flow rate	m^3s^{-1}
W	Work	Jkg^{-1}
\dot{W}	Power	Js^{-1}
w_e	Elastic radial load	N/m
x	Concentration of ammonia	
\bar{x}	Molar fraction of ammonia in liquid phase	
y	Step size	
\bar{y}	Molar fraction of ammonia in gas phase	
z	Number of lobes on rotor	

Abbreviations

<i>COP</i>	Coefficient of performance
<i>OECD</i>	Organisation for Economic Co-operation and Development

Greek

α	Stop angle	
Δ	Difference	
δ	Lip contact thickness	mm
η	Efficiency	
μ	Coefficient of friction	
$\bar{\mu}$	Chemical potential	$kJkmol^{-1}$
ω	Angular rotational speed	
ρ	Density	kgm^{-3}
τ	Inverse of reduced temperature	
φ	Shaft rotation angle	$^\circ$
ζ	Resistance coefficient	

Superscripts

E	Excess
id	Ideal

Subscripts

0	Initial value
1	Male rotor
2	Female rotor
<i>A</i>	Ammonia
<i>b</i>	Compressor body
<i>be</i>	Bearings
<i>Bubble</i>	Bubble point
<i>c</i>	Critical
<i>Comp</i>	Compression
<i>cond</i>	condensing
<i>Dew</i>	Dew point
<i>Dis</i>	Discharge
<i>dis</i>	discharge
<i>disp</i>	Displacement
<i>f</i>	Friciton
<i>G</i>	Gas phase
<i>HT</i>	Heat Transfer
<i>in</i>	Inlet
<i>ind</i>	indicated
<i>inst</i>	Installation
<i>is</i>	Isentropic
<i>iso</i>	isothermal
<i>L</i>	Liquid phase
<i>l</i>	Leakage
<i>lub</i>	Lubricant
<i>max</i>	Maximum
<i>out</i>	Outlet
<i>p</i>	Pump
<i>s</i>	Shaft
<i>se</i>	Seals
<i>suc</i>	Suction
<i>th</i>	Theoretical
<i>vol</i>	Volume
<i>W</i>	Water

1

INTRODUCTION

The largest problem in the world today is how quickly energy demand is increasing. By finding more efficient and less energy consuming solutions it is possible to handle this increase better. With this study a new compressor prototype is examined to see if that can achieve better results than current options on the market.

1.1. BACKGROUND

In these times with new technology being developed constantly and increasing number of people using the products, the need for energy in the world is increasing rapidly. The International Energy Outlook published by Energy Information Administration in the U.S. regularly has a reference case looking at the expected energy demand from 2012 to 2040 [22].

In Figure 1.1 the overall energy consumption is shown, at ten year intervals, with real values from 1990 to 2012 and estimated values up until 2040, these values were estimated in the year 2016.

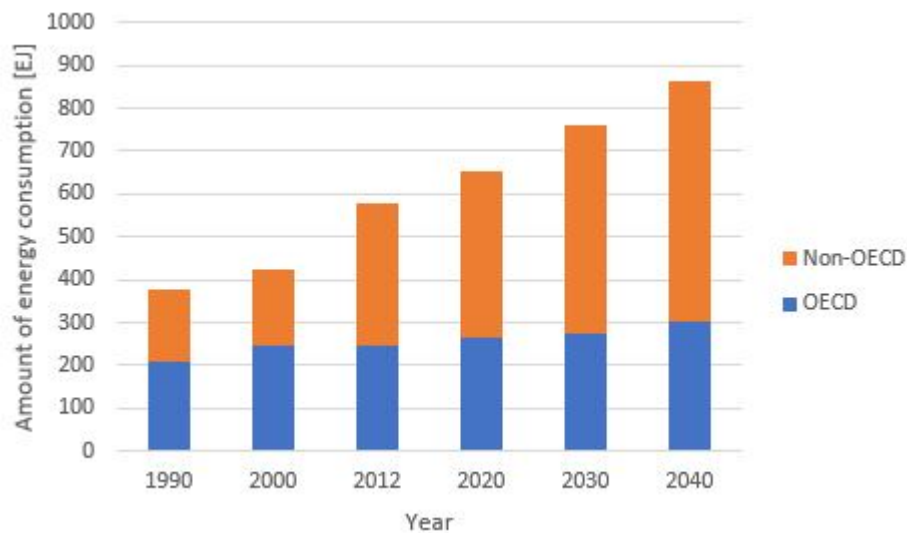


Figure 1.1: World energy consumption from 1990-2040 [EJ] [22]. Real values up until 2012 after that values are estimated. Comparing OECD and non-OECD countries with a noticeable increase for non-OECD over the years.

The scale is shown in ExaJoule and is split into OECD and non-OECD countries. OECD stands for Organisation for Economic Co-operation and Development and is an intergovernmental economic organisation with 35 countries as members. It was founded in 1960 to stimulate economic progress and world trade. Most of the OECD countries have high income economies and most are considered as developed countries.

In 2012 the total consumption of marketed energy was nearly 580 EJ, and according to this estimation it will have a 48% increase by the year 2040.

However, the majority of the increase is coming from the non-OECD countries. Even though many of them have not been regarded as developed countries yet, they are getting closer and with potential increased energy needs. As can be seen in Figure 1.1 while the total difference may be 48%, for non-OECD countries in 2012 to 2040 the difference was close to 70% while the OECD countries had a total rise of 18% over the same period[22].

It is clear that the need for energy is only going to increase steadily. Thus it is important to try to find new technologies that can achieve the needed output, while still needing equal or less amount of energy input.

However, this model was redone with improvements in 2017. In that model the estimated value of overall world energy consumption in 2040 is 776 EJ [23] which has decreased considerably from the estimation of roughly 844 EJ in 2040 done in 2016. Where the difference for non-OECD countries dropped from almost 70% of the change to 41% and within OECD countries from 18 to 9%.

While this difference is partly due to better model conditions, it can also decrease with new technologies that result in better energy efficiency. Proving the need to find better solutions.

The energy use is divided over many fields. The largest consumer of delivered energy is the industry sector. When combined the energy use of industry in the world is over 50% of the total delivered energy. This sector is expected to have an increase of 0.7% a year from 2015 to 2040.

Another contender in energy consumption is due to transportation. In 2017 the annual increase of energy consumption due to transportation was around 1% a year. With this growth essentially been due to the non-OECD countries, as they are expanding faster than the OECD countries. However, at this point in time the OECD countries are responsible for around 55% of the actual energy used for transportation. In 2040 it is estimated that these two groups are close to equal in transport energy usage.

Residential and commercial buildings use around 20% of the total energy worldwide. With the same reference case as before it was calculated that in the next 20 years the delivered energy for buildings will grow around 1.1% a year for non-OECD countries, or around three times the growth within the OECD countries. This is as said before higher because of increasing development in those countries that have not been as advanced in that area before.

In Figure 1.2 the distribution between the three largest energy consumers is shown, this accounts for about 80% of the consumed energy, while 20% is split into sectors with much less usage, such as agriculture. It can be seen from this chart that the consumption is rising rather steadily in these three largest fields. From this, the difference between industry, transport and buildings is quite clear.

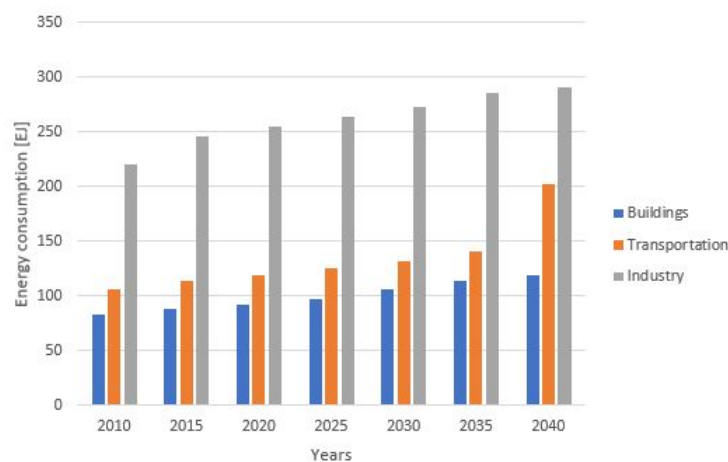


Figure 1.2: Major contribution to the final energy consumption worldwide [23]. The three biggest contributors are shown here, they are industry, transportation and buildings in that order. Up until 2015 is calculated, while after that all values are estimated.

It is also interesting to compare this overall energy usage in the world with distribution of energy in the Netherlands, shown in Figure 1.3.

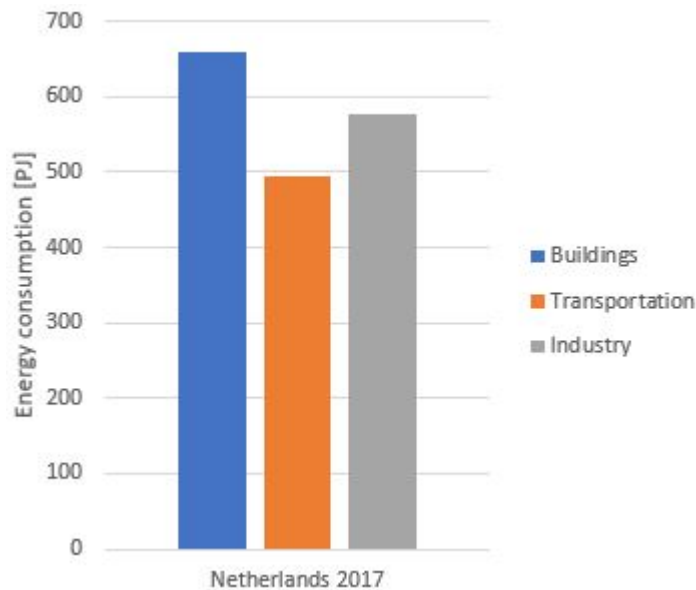


Figure 1.3: Major contribution to the final energy consumption in Netherlands [6] in 2017. Here they are buildings, industry and transportation in that order. This is different order than the worldwide distribution with more energy being used for the building sector.

The total usage of the Netherlands was around 2050 PJ in 2017, where the majority around 32% is consumed by buildings then 28% is used by the industry. The distribution between sectors is seen in Figure 1.4. These numbers are quite different from the world's consumption, while overall in the world industry is clearly the largest user, the three main sectors are much closer together with industry only being the second largest user. It is possible that this difference relates to what these two different reference cases include in the energy consumption of the industry sector. For example if all manufacturing is considered in both cases, even that which can be performed with other methods that don't require as much energy.

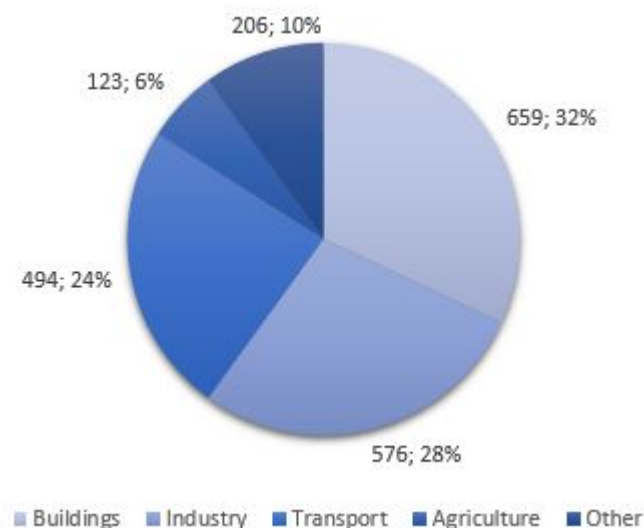


Figure 1.4: Distribution of final energy use between sectors in Netherlands [PJ] [6]. Here the smaller contributors are also considered in the total distribution.

In the Netherlands it is possible e.g. to apply heat pumps in all levels of industry from bulk distillation in chemical industry to simple process on farms or greenhouses [1].

Currently heat pumps are rarely used in industry. However, by using heat pumps it is possible to reduce energy requirements in various parts of the industry. This is done by increasing the COP which could hopefully help in decreasing the payback period. In this study a part of the heat pump cycle, the compressor, is studied in more detail. The objective is to increase the coefficient of performance of the heat pump cycle. Getting to the best efficiency of these pumps is a big factor in decreasing energy usage. Thus this is a probable way to reduce energy consumption in this field. Compressors in general are used frequently in industry, which is the field that is, as shown in this chapter, the largest contributor to energy consumption. By having an effective heat pump cycle energy consumption can be decreased drastically, thus by finding new technologies and improving those already available the increase of energy demand in the industry can be slowed down.

1.2. RESEARCH QUESTION

Can a heat pumps utilizing wet compression without liquid injection achieve similar or better efficiencies as processes with liquid injection. By using liquid injection experiments have obtained efficiencies of around 70% [18] [3].

The objective is to develop a model that can simulate the performance of the compressor, with minimum computational time. By using simplified geometries and calculation methods the computational time can go from a few hours to 15 minutes. This model can be used as a preliminary testing module, where results can be achieved quickly.

1.3. APPROACH TO PROBLEM

First the heat pump cycle is simulated, with special focus on the compressor. This simulation will be done in Matlab utilizing a model made with elements from various other papers, mostly from Zaytsev [26] and Chamoun et al. [4]. During the study the process is assumed to be homogeneous. Later this simulation will be validated by experiments, however, in this study the compressor was not available so validation is done by comparing the model results to trends of oil free twin screw compressors.

Since the compressor was not available the experimental part focuses on getting the experimental setup ready with some preliminary tests on various equipments and finding what problems must be solved before the compressor is connected. The main focus is to get the appropriate conditions at the compressor inlet from the heat pump cycle. To predict how the cycle will behave a Matlab script is written and used to predict the outcomes.

2

THEORY

The general cycle that is being researched for this project is a compression-resorption heat pump cycle. The focus in this research is on the compressor, more specifically wet compression, instead of the more researched dry compression. This is partly because when using non azeotropic mixtures, such as ammonia (NH_3) and water, wet compression becomes a more attractive option since for those heat pumps the desorption process is often incomplete [10]. This is however only true if the isentropic efficiency of the compressor is higher than 70%

When using a non-azeotropic mixture, condensation and evaporation take place at non constant temperatures, as opposed to the fairly constant temperatures for pure refrigerants. This leads to an extra degree of freedom, which results in two degrees of freedom in total for non azeotropic mixtures; the temperature as a function of pressure and the liquid concentration.

With this a rather big advantage for mixtures is that the operating temperature range can be controlled with the concentration.

2.1. THERMODYNAMIC PROPERTIES OF AMMONIA-WATER MIXTURE

In order to simulate wet compression it is necessary to have proper values of the thermodynamic properties of ammonia-water mixture. A comfortable way is to use programs such as REFPROP [11] to look up the correct values at each stage in the model. It is also a quicker but more technically difficult possibility to calculate the properties manually.

Experimental studies of this mixture started in the 1860's [17]. In this mixture ammonia is the volatile component. The use of an ammonia and water refrigerant mixture is quite convenient for heat pumps with the possibility of high temperatures. It can allow heat rejection temperature of 80-160°C. Not only can the concentration of the mixture control the temperature glide, as noted for non azeotropic mixtures, but also the concentration can be varied for different processes.

Some other advantages that make ammonia water a good refrigerant for heat pumps are reliability and good partial load behaviour [27].

2.1.1. RATTNER AND GARIMELA / ZIEGLER AND TREPP EQUATIONS

Ziegler and Trepp [27] developed a model to compute properties of this mixture. There are two separate equations for liquid and gas phases, that can be linked with the following equations.

$$T_L = T_G \quad (2.1)$$

$$\bar{\mu}_{L,A} = \bar{\mu}_{G,A} \quad (2.2)$$

$$p_L = p_G \quad (2.3)$$

$$\bar{\mu}_{L,W} = \bar{\mu}_{G,W} \quad (2.4)$$

The Gibbs free energy of a phase is the sum of all contributions from the pure component [27]. The Gibbs free energy of a liquid two component mixture is shown in Equations 2.5 and 2.6 [26].

$$g_L = (1 - \bar{x})\bar{\mu}_{L,W} + \bar{x}\bar{\mu}_{L,A} \quad (2.5)$$

$$\left(\frac{\partial g_L}{\partial \bar{x}}\right)_{p,T} = \bar{\mu}_{L,A} - \bar{\mu}_{L,W} \quad (2.6)$$

Where \bar{x} is the mole concentration, of ammonia. When Equations 2.5 and 2.6 are solved together the result is the chemical potential for each component, as can be seen in Equations 2.7 and 2.8.

$$\bar{\mu}_{L,A} = g_L + (1 - \bar{x})\left(\frac{\partial g_L}{\partial \bar{x}}\right)_{p,T} \quad (2.7)$$

$$\bar{\mu}_{L,W} = g_L - \bar{x}\left(\frac{\partial g_L}{\partial \bar{x}}\right)_{p,T} \quad (2.8)$$

Then by using the same method to get to the gas phase equations, Equations 2.1,2.2, 2.3 and 2.4 can be rewritten in more detail as is shown in Equation 2.9-2.12

$$T_L = T_G \quad (2.9)$$

$$p_L = p_G \quad (2.10)$$

$$g_L + (1 - \bar{x})\left(\frac{\partial g_L}{\partial \bar{x}}\right)_{p,T} = g_G + (1 - \bar{y})\left(\frac{\partial g_G}{\partial \bar{y}}\right)_{p,T} \quad (2.11)$$

$$g_L - \bar{x}\left(\frac{\partial g_L}{\partial \bar{x}}\right)_{p,T} = g_G - \bar{y}\left(\frac{\partial g_G}{\partial \bar{y}}\right)_{p,T} \quad (2.12)$$

Next Ziegler and Trepp [27] showed that Gibbs energy for liquid and gas can be written as explicit functions of phase pressure, temperature and molar concentration. Then it is possible to express other thermodynamic properties with the Gibbs energy. Molar volume, entropy and enthalpy are shown in Equations 2.13, 2.14 and 2.15

$$\bar{v} = \left(\frac{\partial g_L}{\partial p}\right)_{T,x} \quad (2.13)$$

$$\bar{s} = -\left(\frac{\partial g_L}{\partial T}\right)_{p,x} \quad (2.14)$$

$$\bar{h} = -T^2\left(\frac{\partial g_L}{\partial T}\right)_{p,x} \quad (2.15)$$

These equations are applicable for both phases. Then the molar specific value of state parameters is converted into mass specific. In order to do this the molar specific value is divided by the molar mass. By using Equations 2.16 and 2.17 the molar mass for gas and liquid phase can be found.

$$M_L = M_A * \bar{x} + M_W(1 - \bar{x}) \quad (2.16)$$

$$M_G = M_A * \bar{y} + M_W(1 - \bar{y}) \quad (2.17)$$

Next is to find the mass fraction of liquid and vapour, and when they are found it is possible to calculate the specific volume, entropy and enthalpy of the mixture.

2.1.2. FREE ENTHALPY MODEL

In 2006 Mejbri and Bellagi [14] researched the thermodynamic properties of ammonia-water mixtures and defined three different approaches. An empirical Gibbs free enthalpy model, another using the Patel-Teja cubic equations of state and one using the PC-SAFT equation of state. Mejbri and Bellagi found the free enthalpy model to be the most flexible and able to describe the thermodynamic surface of the ammonia water mixture up to 80 bar and 500 K, this range should be suitable for the current study.

In binary mixtures the molar free enthalpy can be expressed as a function, shown in Equation 2.18

$$G(\tau, p, \bar{x}) = (1 - \bar{x})G_W(\alpha_W\tau, p) + \bar{x}G_A(\alpha_A\tau, p) + \frac{RT_b}{\tau}(\bar{x}\ln(\bar{x}) + (1 - \bar{x})\ln(1 - \bar{x})) + G^E(\tau, p, \bar{x}) \quad (2.18)$$

$$\alpha = \frac{T_c}{T_b} \quad (2.19)$$

The constant α is defined as shown in Equation 2.19, using the corresponding critical temperature for ammonia or water. Additionally the Gibbs free energy function for a pure fluid is shown in Equation 2.20

$$G(\tau, p) = \bar{h}(\tau_0, p_0) - \frac{T_c}{\tau}\bar{s}(\tau_0, p_0) + T_c \int_T^{T_0} \frac{\bar{C}_p(\tau, p_0)}{\tau^2} d\tau - \frac{T_c}{\tau} \int_T^{T_0} \frac{\bar{C}_p(\tau, p_0)}{\tau} d\tau + \int_{p_0}^p \bar{v}(\tau, p) dp \quad (2.20)$$

In this model the liquid and vapour phases are first examined separately and then put together by using the equalities in chemical potential at the vapour liquid equilibrium [14].

Equations 2.21 and 2.22 show the molar volume and isobaric heat capacity for the liquid phase, with coefficients a_i and b_i as adjustable parameters which are shown in Appendix A.1 .

$$V_L(\tau, p) = a_1 + a_2 p + \frac{a_3}{\tau} + \frac{a_4}{\tau^2} \quad (2.21)$$

$$C_{pL}(\tau, p) = b_1 + \frac{b_2}{\tau} + \frac{b_3}{\tau^2} \quad (2.22)$$

For the vapour phase a virial equation of state is used, shown in Equation 2.23, with the virial constants B and C.

$$Z = 1 + B'p + C'p^2 \quad (2.23)$$

In order to find constants B and C the following equations are necessary.

$$B' = \frac{\tau B}{RT_c} \quad (2.24)$$

$$C' = \frac{\tau^2(C - B^2)}{(RT_c)^2} \quad (2.25)$$

$$B(\tau) = \beta_1\tau^{\beta_2} + \beta_3\tau^{\beta_4} \quad (2.26)$$

$$C(\tau) = \beta_5\tau^{\beta_6} \quad (2.27)$$

Now to find the real gas molar isobaric heat capacity deduced from that of ideal gas, shown in Equation 2.28

$$C_{pG}(\tau, p_0) = C_p^{id}(\tau) - \int_0^{p_0} \left(\frac{\partial^2 \bar{v}}{\partial T^2} \right)_p dp \quad (2.28)$$

Where the general model shown in Equation 2.29 is used for the ideal value of C_p .

$$\frac{C_p^{id}}{R} = c_0 + \sum_k c_k \frac{(\theta_k \tau^2) e^{\theta_k \tau}}{(1 - e^{\theta_k \tau})^2} \quad (2.29)$$

β_i , c_i and θ_i are adjustable coefficients that are shown in Appendix A.1.

The reference state, τ_0 , p_0 , is a vapour liquid equilibrium state, the relation between references is obtained with Equation 2.30.

$$\bar{s}_L(\tau_0, p_0) = \bar{s}_G(\tau_0, p_0) \frac{\tau_0}{T_c} (-bar{a}r h_G(\tau_0, p_0) - \bar{h}_L(\tau_0, p_0)) \quad (2.30)$$

Next is to look at the excess of molar free enthalpy, which is a function of temperature, pressure and molar composition. For the vapour phase it is possible to consider it as an ideal solution while for the liquid phase the Redlich-Kister direction is used [14]. Putting this together Equation 2.31 is obtained for the excess.

$$G^E(\tau, p, x) = \frac{RT_b}{\tau} x(1-x)(f_1(\tau, p) + (2x-1)f_2(\tau, p) + (2x-1)^2 f_3(\tau, p)) \quad (2.31)$$

The constants f_i are functions of temperature and pressure and can be found with the following equations, with γ_i as adjustable coefficients whose values are shown in Appendix A.1.

$$f_1(\tau, p) = \gamma_1 + \gamma_2 p + \gamma_3 p^2 + (\gamma_4 + \gamma_5 p)\tau + (\gamma_6 + \gamma_7 p)\tau^2 + \left(\frac{\gamma_8}{\tau} + \frac{\gamma_9}{\tau^2}\right)p \quad (2.32)$$

$$f_2(\tau, p) = \gamma_{10} + \gamma_{11} p + \gamma_{12} p^2 + (\gamma_{13} + \gamma_{14} p)\tau \quad (2.33)$$

$$f_3(\tau, p) = \gamma_{15} + \gamma_{16} p + \gamma_{17} \tau \quad (2.34)$$

2.1.3. PATEK AND KLOMFAR EQUATIONS

In 1995 Patek and Klomfar [16] put forth five equations to describe vapour liquid equilibrium properties of the ammonia water mixture, they can be found in Equations 2.35-2.39. Where the dew point is defined as when the first drop of liquid is formed and the bubble point is when the first vapour bubble is formed.

$$T_{bubble}(p, \bar{x}) = T_0 \sum_i a_i (1 - \bar{x})^{m_i} \left(\ln \left(\frac{p_0}{p} \right) \right)^{n_i} \quad (2.35)$$

$$T_{dew}(p, \bar{y}) = T_0 \sum_i a_i (1 - \bar{y})^{m_i/4} \left(\ln \left(\frac{p_0}{p} \right) \right)^{n_i} \quad (2.36)$$

With Equation 2.37 the composition of the vapour phase can be found.

$$\bar{y}(p, \bar{x}) = 1 - \exp \left(\ln(1-x) \sum_i a_i \left(\frac{p}{p_0} \right)^{m_i} \bar{x}^{n_i/3} \right) \quad (2.37)$$

$$h_L(T, \bar{x}) = h_0 \sum_i a_i \left(\frac{T}{T_0} - 1 \right)^{m_i} \bar{x}^{n_i} \quad (2.38)$$

$$h_G(T, \bar{y}) = h_0 \sum_i a_i \left(1 - \frac{T}{T_0} \right)^{m_i} (1 - \bar{y})^{n_i/4} \quad (2.39)$$

The coefficients, a_i , m_i , n_i needed for these five equations can be found in Appendix A.2.

2.1.4. COMPARISON

In 2012 Türkmen [21] made comparisons with Fluidprop and the models by Ziegler and Trepp and Patek and Klomfar. He compared the most used thermodynamic properties such as dew and bubble point temperatures, density, entropy, enthalpy and specific heat capacity.

When comparing the saturated liquid and vapour temperatures between Patek and Klomfar and Fluidprop the deviation is very low for the saturated liquid, while it is a bit higher for the saturated vapour however it reaches a maximum of 1% when the concentration of ammonia is high.

Next he compared the enthalpy values at saturated liquid and vapour, here it was possible to compare both Patek and Klomfar and Ziegler and Trepp to Fluidprop. Both models had quite similar values to each

other with the deviation from Fluidprop increasing with added ammonia concentration. Similar to the temperature the deviation is higher for saturated vapour.

When comparing the density of the mixture it was only available with [Ziegler and Trepp](#) and as for the other properties the deviation is around 1% which is within an acceptable range. Entropy was also compared at the saturated conditions. There the deviation increases rather steadily with increased ammonia concentration, but still within acceptable range so this method is adequate.

The largest deviation appears when comparing the specific heat capacity. There the error in the liquid phase reaches up to 4% for high concentration of ammonia while the error is only around 1% for up to 80% ammonia, which is considerably higher than this study is expected to go, so this deviation should not be a problem. [Türkmen](#) made some comparisons in this sector with [M. Conde Engineering](#) [12] but did conclude that [Ziegler and Trepp](#) was the best way to determine the heat capacity [21].

As mentioned at the start of this section, the program Refprop [11] is often used to calculate thermodynamic properties as it is easily connected with Matlab [13]. However, Refprop has problems finding certain values while in the two phase region, which this study uses for the most part. It has also rather slow calculations, specially compared to [Ziegler and Trepp](#) which [Rattner and Garimella](#) [17] has an open source script with all equations needed to calculate available. With the conclusion from [Türkmen](#) in mind, the script from [Rattner and Garimella](#) is used for the bulk of the calculations, except for cases where properties such as entropy are used as input, then Refprop is used instead.

To conclude this section on possible thermodynamic models, most properties will be calculated either with [Ziegler and Trepp](#) or Refprop. The model by [Mejbri and Bellagi](#) is mostly focusing on the heat capacity which as shown by [Türkmen](#) is also possible with minimal deviations by using the model of [Ziegler and Trepp](#). As the model by [Mejbri and Bellagi](#) hasn't been proven against concrete values, and there is not a lot of experimental data regarding it, the model by [Ziegler and Trepp](#) will be chosen instead.

By using the equations connected to these two main models the thermodynamic properties can be calculated for the two phase region by using the saturated liquid and vapour conditions.

2.2. COMPRESSOR

There are many possible ways to perform the compression process, with the main categories under mechanical compressors being positive displacement and dynamic compressors. It is important to have the correct compressor for each task in order to achieve the best efficiency.

In this study it is already possible to rule out quite a number of compressor possibilities as this compressor must be compatible with two phase input instead of pure gas.

In 2003 Zaytsev made a comparison of many possible types of compressors that could possibly be used for wet compression [26]. When having high liquid levels, screw compressors are generally more tolerant than other compressors such as centrifugal compressors, as they have no blades or valves that the liquid could damage. Making them ideal candidates for wet compression. They can be single screw or with two rotors called twin screw.

2.2.1. SINGLE SCREW COMPRESSOR

A positive displacement compressor, with one main rotor and a couple of gate rotors. Only the main rotor is driven. With positive displacement the compression is achieved by positive reduction of gas volume inside a closed cavity, when the volume gets smaller the pressure rises. The compression happens in the volume of the cavity by a groove of the main rotor, a tooth of the gate rotor and the inside of the cavity. It has built in volume ratio and no valves. The axial load resting on the main rotor is balanced, since both rotor faces are under suction pressure, thus resulting in lower bearing loads [26].

The isentropic efficiency can be viewed as a function of the pressure ratio and a built in volume ratio.

2.2.2. TWIN SCREW COMPRESSOR

In a twin screw compressor there are two helical rotors, a male and female that fit together[26]. Generally only the male rotor is driven by an outside force which turns the female one. However when using oil free compressors the rotation of the two rotors is driven through timing gears on each rotor [8]. This is done since there is no oil between the two rotors, so there is not a lot of lubrication between them except just from the working fluid. Therefore, it is better to minimize the contact between the rotors by using synchronization of the rotors with gears instead of the male rotor turning the female one.

The twin screw compressor falls under the category of positive displacement compressors, with rotary functions. Originally it was invented to have a high speed positive displacement that did not suffer from surging.

Universally there are two types of twin screw compressors, with or without liquid injection. This liquid can be for example oil or water, and is used for cooling, sealing and lubrication. The liquid assists in lubricating bearings and closing the cavities. In an oil free compressor there is no oil in the process side except just to lubricate bearings and seals, which are separated from the process side.

The twin screw compressor has a much wider flow rate capacity than the single screw, which can emulate the reciprocating or centrifugal compressors. The volumetric efficiency for screw compressors tends to be rather high and for twin screw it can go from 85% to 95%. The isentropic efficiency has a bit of a larger range, going from 50 to 80%, which is still competitive with other potential compressors.

In this case the compressor needs to be oil-free and without any liquid injected into the compressor. Making the twin screw a better choice than a single screw. The compressor should be oil free as the process of separating the oil from the working fluid can be quite tedious when working with two phase flow. In 1981 [15] another possibility was introduced, to spray the liquid into the compressor inlet in order to dissolve or remove unwanted particles from the vapour. This method will be partly used in this process before the compressor inlet in order to achieve homogeneous state before entering the compressor.

3

MODEL

In order to be able to simulate the results of the cycle it is necessary to have a good model for all the needed parameters. For the purpose of this project, a couple of possible models for the compression cycle were researched and compared. The following sections will discuss possible models as well as the selected model.

Important parameters are the volumetric and isentropic efficiency, temperature and pressure values, as well as keeping an eye on possible leakages.

3.1. WET COMPRESSION WITH COMPLEX GEOMETRY

In 2003 [Zaytsev](#) proposed a simulation model for an oil-free two phase twin screw compressor. In this simulation an ammonia water mixture was used as the working fluid [26].

First this model looks into the thermodynamic part of the system. It is built on the conservation laws for a chosen control volume and the equation of state. With the geometry of the compressor it can predict the shaft angle dependent thermodynamic parameters of the working mixture and compressor performance characteristics. Those characteristics can include the volumetric and isentropic efficiency as well as the flow rate and compression power.

The chosen control volume is the volume of one cavity, that is formed by the two rotors and the compressor housing. As this type of compressor falls under positive displacement it can be assumed that the control volume can be schematically represented as a cylindrical chamber with piston in and out flows. It should also be assumed that within this chamber the pressure is uniform.

Here a homogeneous pT model is used, based on the assumption that the liquid and the vapour are in equilibrium. This gives the following conservation equations seen in Equations 3.1, 3.2 and 3.3.

$$dm = \sum_{k=1}^l dm_{in,k} - \sum_{k=1}^n dm_{out,k} \quad (3.1)$$

$$d(mx_0) = \sum_{k=1}^l x_{0in,k} dm_{in,k} - x_0 \sum_{k=1}^n dm_{out,k} \quad (3.2)$$

$$\delta Q + \sum_{k=1}^l h_{in,k} dm_{in,k} - h \sum_{k=1}^n dm_{out,k} = dH - V dp \quad (3.3)$$

Here m is for mass of mixture, H is the total enthalpy of homogeneous working mixture, h is the specific enthalpy, Q is transferred heat from the compressor to the mixture and x_0 is the concentration of ammonia in the mixture. This transferred heat is neglected when using the actual model as the heat is presumed to not be a big factor in the total outcome.

Equation 3.1 can be rewritten as Equation 3.4

$$dm = \frac{1}{v} dV + V d\left(\frac{1}{v}\right) \quad (3.4)$$

Where v is the specific volume, that is a function of pressure, temperature and overall concentration x_0 . By differentiating this equation by the shaft rotation angle Equation 3.5 is found.

$$\frac{dm}{d\varphi} = \frac{1}{v} \frac{dV}{d\varphi} - \frac{V}{v^2} \left(\left(\frac{\partial v}{\partial p} \right)_{T,x} \frac{dp}{d\varphi} + \left(\frac{\partial v}{\partial T} \right)_{p,x} \frac{dT}{d\varphi} + \left(\frac{\partial v}{\partial x_0} \right)_{p,T} \frac{dx_0}{d\varphi} \right) \quad (3.5)$$

By looking at the two mass conservation equations, combining them and rearranging terms Zaytsev got the following mass conservation equation shown in Equation 3.6.

$$\frac{dp}{d\varphi} = \frac{1}{\left(\frac{\partial v}{\partial p} \right)_{T,x}} \left(\frac{v}{m} \left(\sum_{k=1}^n \left(\frac{dm_{out}}{d\varphi} \right)_k - \sum_{k=1}^l \left(\frac{dm_{in}}{d\varphi} \right)_k \right) + \frac{1}{m} \frac{dV}{d\varphi} - \left(\frac{\partial v}{\partial T} \right)_{p,x} \frac{dT}{d\varphi} - \left(\frac{\partial v}{\partial x_0} \right)_{p,T} \frac{dx_0}{d\varphi} \right) \quad (3.6)$$

Then by doing the same differentiation for the ammonia mass conservation and rearranging some terms leads to Equations 3.7 and 3.8.

$$m \frac{dx_0}{d\varphi} + x_0 \frac{dm}{d\varphi} = \sum_{k=1}^l x_{0,in,k} \left(\frac{dm_{in}}{d\varphi} \right)_k - x_0 \sum_{k=1}^n \left(\frac{dm_{out}}{d\varphi} \right)_k \quad (3.7)$$

$$\frac{dx_0}{d\varphi} = \frac{1}{m} \left(\sum_{k=1}^l x_{0,in,k} \left(\frac{dm_{in}}{d\varphi} \right)_k - x_0 \sum_{k=1}^n \left(\frac{dm_{out}}{d\varphi} \right)_k \right) \quad (3.8)$$

However, in this model Zaytsev had a liquid injection, which changes the concentration of ammonia. In the current study there is no liquid injected thus the concentration of ammonia does not change and all derivations of x_0 can be neglected.

Now differentiating the final conservation equation, one of energy, with the same angle as before gives Equation 3.9

$$m \frac{dh}{d\varphi} + h \frac{dm}{d\varphi} = \frac{\partial Q}{\partial \varphi} + \sum_{k=1}^l h_{in,k} \left(\frac{dm_{in}}{d\varphi} \right)_k - h \sum_{k=1}^n \left(\frac{dm_{out}}{d\varphi} \right)_k + V \frac{dp}{d\varphi} \quad (3.9)$$

Now the specific enthalpy of the mixture can be considered as a function of pressure, temperature and concentration of the mixture and can thus be rewritten as Equation 3.10

$$\begin{aligned} m \left(\left(\frac{\partial h}{\partial p} \right)_{T,x} \frac{dp}{d\varphi} + \left(\frac{\partial h}{\partial T} \right)_{p,x} \frac{dT}{d\varphi} + \left(\frac{\partial h}{\partial x_0} \right)_{p,T} \frac{dx_0}{d\varphi} \right) + h \frac{dm}{d\varphi} \\ = \frac{\partial Q}{\partial \varphi} + \sum_{k=1}^l h_{in,k} \left(\frac{dm_{in}}{d\varphi} \right)_k - h \sum_{k=1}^n \left(\frac{dm_{out}}{d\varphi} \right)_k + V \frac{dp}{d\varphi} \end{aligned} \quad (3.10)$$

In thermodynamics there is a relation for partial derivative of enthalpy by pressure, which is shown in Equation 3.11

$$\left(\frac{\partial h}{\partial p} \right)_{T,x} = v - T \left(\frac{\partial v}{\partial T} \right)_{p,x} \quad (3.11)$$

Now by using this relation and the previously defined equations it is possible to get to the derivative of temperature by shaft rotation angle. This formula is shown in Equation 3.12.

$$\begin{aligned} \frac{dT}{d\varphi} = \frac{T \left(\frac{\partial v}{\partial T} \right)_{p,x} \left(\frac{v}{m} \left(\sum_{k=1}^n \left(\frac{dm_{out}}{d\varphi} \right)_k - \sum_{k=1}^l \left(\frac{dm_{in}}{d\varphi} \right)_k \right) + \frac{1}{m} \frac{dV}{d\varphi} - \left(\frac{\partial v}{\partial x_0} \right)_{p,T} \frac{dx_0}{d\varphi} \right)}{\left(\frac{\partial v}{\partial p} \right)_{T,x} \left(\frac{\partial h}{\partial T} \right)_{p,x} + T \left(\frac{\partial v}{\partial T} \right)_{p,x}^2} \\ + \frac{\frac{\partial Q}{\partial \varphi} + \sum_{k=1}^l (h_{in,k} - h) \left(\frac{dm_{in}}{d\varphi} \right)_k - m \left(\frac{\partial h}{\partial x_0} \right)_{p,T} \frac{dx_0}{d\varphi}}{m \left(\frac{\partial h}{\partial T} \right)_{p,x} + \frac{mT}{\left(\frac{\partial v}{\partial p} \right)_{T,x}} \left(\frac{\partial v}{\partial T} \right)_{p,x}^2} \end{aligned} \quad (3.12)$$

Now the simplified governing equations can be found and are shown in Equations 3.13 and 3.14. Without liquid injection Equation 3.8 is left out.

$$\frac{dp}{d\varphi} = \frac{1}{\left(\frac{\partial v}{\partial p}\right)_{T,x}} \left(\frac{v}{m} \left(\sum_{k=1}^n \left(\frac{dm_{out}}{d\varphi} \right)_k - \sum_{k=1}^l \left(\frac{dm_{in}}{d\varphi} \right)_k \right) + \frac{1}{m} \frac{dV}{d\varphi} - \left(\frac{\partial v}{\partial T} \right)_{p,x} \frac{dT}{d\varphi} \right) \quad (3.13)$$

$$\frac{dT}{d\varphi} = \frac{T \left(\frac{\partial v}{\partial T} \right)_{p,x} \left(\frac{v}{m} \left(\sum_{k=1}^n \left(\frac{dm_{out}}{d\varphi} \right)_k - \sum_{k=1}^l \left(\frac{dm_{in}}{d\varphi} \right)_k \right) + \frac{1}{m} \frac{dV}{d\varphi} \right) + \frac{\partial Q}{\partial \varphi} + \sum_{k=1}^l (h_{in,k} - h) \left(\frac{dm_{in}}{d\varphi} \right)_k}{\left(\frac{\partial v}{\partial p} \right)_{T,x} \left(\frac{\partial h}{\partial T} \right)_{p,x} + T \left(\frac{\partial v}{\partial T} \right)_{p,x}^2} + \frac{m \left(\frac{\partial h}{\partial T} \right)_{p,x} + \left(\frac{mT}{\left(\frac{\partial v}{\partial p} \right)_{T,x}} \left(\frac{\partial v}{\partial T} \right)_{p,x} \right)^2} \quad (3.14)$$

This model is very detailed and can find pressure, temperature and concentration of the mixture by using numerical integration of these governing equations. However in order to run the model it is a necessity to run it alongside a model of the compressor itself. There rises the biggest problem with this kind of detailed model, it needs to have access to the geometry of the compressor which for this study will not be available.

For the time being a simpler model should suffice, but the possibility of assuming certain aspects of the geometry in order to use more complex models is a viable option.

After the relevant properties have been found with the conservation equations listed above the next step is to find the efficiencies of this cycle. Zaytsev published, alongside the conservation equations, which efficiencies he used and how they were found.

The isentropic and indicated power is found with Equations 3.15 and 3.16.

$$\dot{W}_{is} = \dot{m}(h_{is} - h_{suc}) \quad (3.15)$$

Here the h_{is} is the value of the discharge enthalpy under isentropic compression while h_{suc} is the enthalpy at the suction port.

$$\dot{W}_{ind} = z_1 \frac{n}{60} \int p dV \quad (3.16)$$

The last power that is found is for the shaft, which combines all the power that affects the process, including all frictions considered. This is shown in Equation 3.17

$$\dot{W}_s = \dot{W}_{ind} + \dot{W}_{f,comp} + \dot{W}_{f,se} + \dot{W}_{f,be} \quad (3.17)$$

The shaft power combines the indicated power and friction in the seals, bearings and in compressor which happens between the two rotors. As in this study the two rotors rotate by using timing of gears, instead of the male rotor turning the female rotor, that friction factor can be neglected.

Friction in seals is found by adding together the friction torques of seal elastic force and pressure force. This is shown in Equation 3.18 where the pressure difference is across the seal, in bar.

$$\dot{W}_{f,se} = 2\pi r^2 \omega \mu (w_e + \delta \Delta p) \quad (3.18)$$

Then the bearing friction is found with Equation 3.19.

$$\dot{W}_{f,be} = r \omega \mu F_{be} \quad (3.19)$$

Now with all the different power equations accounted for the compressor efficiencies can be calculated. Equation 3.20 shows the indicated efficiency of the compressor while Equation 3.21 is the isentropic efficiency.

$$\eta_{is,comp} = \frac{\dot{W}_{is}}{\dot{W}_{ind}} \quad (3.20)$$

$$\eta_{is,inst} = \frac{\dot{W}_{is}}{\dot{W}_s} \quad (3.21)$$

Finally the volumetric efficiency is found with Equation 3.22. Here the specific volume at the suction is multiplied with the mass change over the compressor which results in the real volume, this is divided by the ideal maximum cavity volume as found with the volume curve.

$$\eta_{vol} = \frac{v_{suc} \int \frac{dm}{d\varphi} d\varphi}{V_{max}} \quad (3.22)$$

3.2. THERMODYNAMIC MODEL

In 2014 van de Bor et al. [24] proposed a general thermodynamic model for the performance of a compression resorption heat pump. This model uses an ammonia water mixture and has the following assumptions.

1. Resorber outlet temperature is 5 K higher than process temperature
2. Either desorber inlet temperature is 5 K lower than the process outlet temperature and more than 5 K lower than the inlet temperature or vice versa
3. No significant pressure loss in both heat exchangers
4. Isentropic efficiency of the compressor is 70%
5. Electric drive efficiency is 100%
6. No heat loss to surroundings

In this model the ammonia concentration can be varied from 0.5 to 99.5% as well as the vapour quality at the resorber inlet, which varies from 10 to 100%.

With Equations 3.23, 3.24 and 3.25 the resorber inlet, or compressor outlet, can be found as a function of the resorber outlet, which in this case was assumed to be saturated liquid.

$$p_{resorber} = f(T_{resorber,out}, q = 0, x) \quad (3.23)$$

$$T_{resorber,in} = f(p_{resorber}, q_{resorber,in}, x) \quad (3.24)$$

$$h_{resorber,in} = f(p_{resorber}, q_{resorber,in}, x) \quad (3.25)$$

Here the expansion valve, from resorber outlet to desorber inlet, is treated as an isenthalpic flash such that the enthalpy stays the same. The relation is shown in Equation 3.26.

$$h_{desorber,in} = h_{resorber,out} = f(T_{resorber,out}, q = 0, x) \quad (3.26)$$

After this the method can go two ways, depending on whether the temperature glide is larger over the resorber or desorber.

3.2.1. LARGE TEMPERATURE GLIDE IN RESORBER

First the pressure in the desorber is found with Equation 3.27. Where $T_{desorber,in}$ comes from the original assumption, that it is 5 K lower than the process outlet condition.

$$p_{desorber} = f(T_{desorber,in}, h_{desorber}, x) \quad (3.27)$$

Now to start a initial condition must be set such that the conditions at the compressor outlet in a theoretical case, with 100% isentropic efficiency, is on the same line as the entropy of the inlet condition.

$$h_{desorber,out,0} = f(p_{desorber}, s_{desorber,out,initial}, x) \quad (3.28)$$

Now everything must be iterated until the values for isentropic enthalpy obtained from Equations 3.29 and 3.30 are converged.

$$h_{desorber,out} = \frac{h_{resorber,in,is} - \eta_{is} h_{resorber,in}}{1 - \eta_{is}} \quad (3.29)$$

$$h_{desorber,out} = f(p_{desorber}, s_{desorber}, x) \quad (3.30)$$

With these iterations it is now possible to find the temperature at the desorber outlet with Equation 3.31.

$$T_{desorber,out} = f(p_{desorber}, h_{desorber,out}, x) \quad (3.31)$$

If it happens that the temperature is higher than the process temperature, when accounting for the required temperature driving force, the corresponding concentration of ammonia can be discarded. Another possibility if this happens could also be to increase the temperature at the desorber inlet.

3.2.2. LARGE TEMPERATURE GLIDE IN DESORBER

With this method the first step is to set the temperature at the desorber outlet with the value of the process temperature minus the temperature driving force and then assuming a entropy value at the outlet of the desorber.

Again an initial value must be decided now with Equation 3.32.

$$h_{desorber,out,initial} = f(T_{desorber,out}, s_{desorber,out,initial}, x) \quad (3.32)$$

Like previously this is iterated until the same value comes from both equations 3.29 and 3.32. Then the pressure and outlet enthalpy are found with Equations 3.33 and 3.34. Then with that the temperature is also found as shown in Equation 3.35

$$h_{desorber} = f(T_{desorber,out}, s_{desorber,out}, x) \quad (3.33)$$

$$p_{desorber} = f(T_{desorber,out}, s_{desorber,out}, x) \quad (3.34)$$

$$T_{desorber,in} = f(p_{desorber}, h_{desorber,in}, x) \quad (3.35)$$

This model focuses only on the inlet and outlet conditions without looking into the geometry or inner workings of the compressor at all.

3.3. GENERAL MODEL

In the paper by Chamoun et al. [4] a twin screw compressor with liquid injection was modelled using the following assumptions. While these assumptions should work with the model needed for this study, the part of liquid injection must be left out as there is no injection in this study.

- Constant inlet velocity during the suction process
- No pressure drop during the suction process

- Pressure and enthalpy are homogeneous throughout the working space at any instant
- Pressure pulsations in the suction and discharge processes are neglected

The assumptions listed above simplify calculations quite a bit, since the suction and discharge phases are constant and the mass flow into the compressor is known and assumed to be constant, mass lost or gained during suction and discharge is not accounted for. This makes for quicker calculations and is ideal for the initial run of the compressor model, when leakages are not accounted for, in order to get values throughout the process to work with. When leakages are added, it is interesting to see how they can affect the suction or discharge phase. Thus, the assumption of a constant suction and discharge are only used for the first run and after that those phases can have small variations.

As in many models before, the ideal control volume for a twin screw compressor, a cavity between the rotors and the housing, is used. In order to simplify it can be represented by an analogy for a piston compressor [4], as can be seen in Figure 3.1.

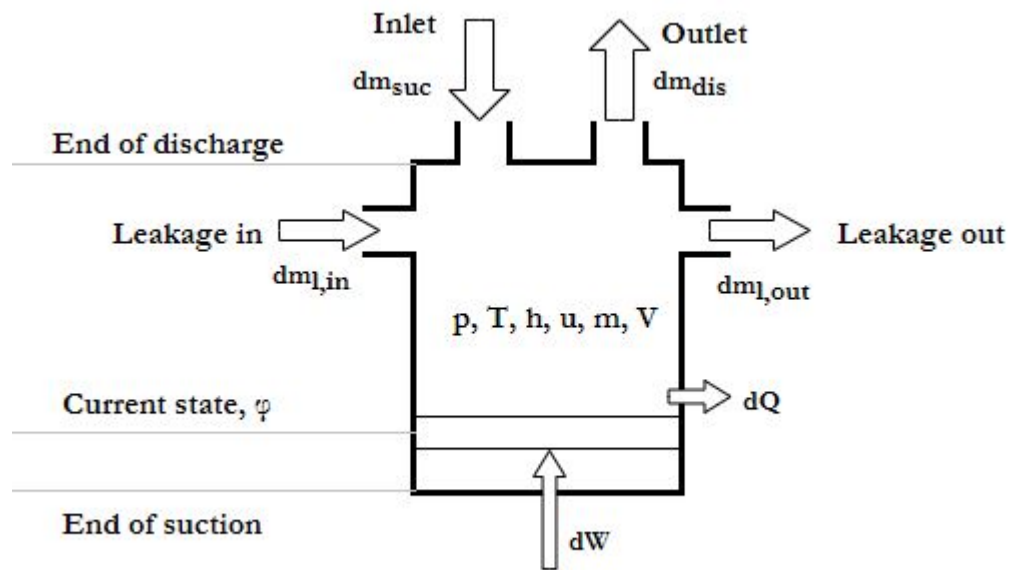


Figure 3.1: Simplified control volume for the compression process

To start with, the first law of thermodynamics is applied to the refrigerant in this control volume, presented in terms of the rotational angle of the rotor φ , this is shown in Equation 3.36.

$$\frac{d(mu)}{d\varphi} = \sum \frac{dm_{in}}{d\varphi} h_{in} - \sum \frac{dm_{out}}{d\varphi} h_{out} + \frac{dW}{d\varphi} + \frac{dQ}{d\varphi} \quad (3.36)$$

The mass balance can be defined by Equation 3.37, where the sum of inflow and outflow includes the leakages.

$$\frac{dm}{d\varphi} = \sum \frac{dm_{in}}{d\varphi} - \sum \frac{dm_{out}}{d\varphi} \quad (3.37)$$

With this mathematical model it is possible to obtain the operating volume instantaneously, by using the rotational angle. With an angular rotational speed, $\omega = \frac{d\varphi}{dt}$, Equations 3.36 and 3.37 can be expressed as Equations 3.38 and 3.39.

$$\omega \frac{d(mu)}{d\varphi} = \sum \dot{m}_{in} h_{in} - \sum \dot{m}_{out} h_{out} - \omega p \frac{dV}{d\varphi} + \dot{Q} \quad (3.38)$$

$$\omega \frac{dm}{d\varphi} = \sum \dot{m}_{in} - \sum \dot{m}_{out} \quad (3.39)$$

In order to analyse the leakage flow rates the grooves adjacent to the working chamber must be known with respect to the rotation angle [4]. The inlet and outlet leakage flows are shown in Equations 3.40 and 3.41.

$$\dot{m}_{l,in} = C_l A_l \sqrt{2\rho_{\varphi+\frac{2\pi}{nm}} \left(p_{\varphi+\frac{2\pi}{nm}} - p_{\varphi} \right)} \quad (3.40)$$

$$\dot{m}_{l,out} = C_l A_l \sqrt{2\rho_{\varphi} \left(p_{\varphi} - p_{\varphi-\frac{2\pi}{nm}} \right)} \quad (3.41)$$

For one revolution, the sum of volumes occupied by the total masses at the end of the suction process is equal to the displacement volume of one groove of the compressor [4]. Mass and specific enthalpy can be calculated with Equations 3.42, 3.43 and 3.44

$$m = m_{suc} + m_{l,in} \quad (3.42)$$

$$mh = m_{suc}h_{suc} + m_{l,in}h_{l,in} + Q_{in} \quad (3.43)$$

$$m = \rho V_{disp} \quad (3.44)$$

Where V_{disp} is the volume of displacement per revolution and Q is heat from the environment. It is assumed that at the suction pressure the process is isobaric. The mass that is lost due to leakage can be calculated with Equation 3.45

$$m_{l,in} = \dot{m}_{l,in} t_{suc} \quad (3.45)$$

During the compression process the inlet and outlet ports are treated as closed and the governing equations used to calculate various thermodynamic properties are found, such as pressure and specific enthalpy. These properties are found in each control volume, for each rotational angle, during the compression. By using finite volume calculations the compressor volume is split into N equal parts. After this Equations 3.42, 3.43 and 3.44 can be discretized and linearized for each control volume.

The mass and energy balances used in the model are shown in Equations 3.46 and 3.47

$$a \frac{\Delta p}{\Delta \varphi} + b \frac{\Delta h}{\Delta \varphi} + c \frac{\Delta V}{\Delta \varphi} = \dot{m}_{l,in} - \dot{m}_{l,out} \quad (3.46)$$

$$d \frac{\Delta p}{\Delta \varphi} + e \frac{\Delta h}{\Delta \varphi} + f \frac{\Delta V}{\Delta \varphi} = \dot{m}_{l,in}h_{l,in} - \dot{m}_{l,out}h_{l,out} + \dot{Q}_{in} \quad (3.47)$$

Where the coefficients a , b , c , d , e and f are shown in 3.48 and 3.49.

$$a = V \left(\frac{\partial \rho}{\partial p} \right)_h \omega \quad b = V \left(\frac{\partial \rho}{\partial h} \right)_p \omega \quad c = \rho \omega \quad (3.48)$$

$$d = V \left(\left(\frac{\partial \rho}{\partial p} \right)_h - 1 \right) \omega \quad e = V \left(\rho + h \left(\frac{\partial \rho}{\partial h} \right)_p \right) \omega \quad f = (h\rho)\omega \quad (3.49)$$

$$\dot{Q} = UA_{HT}(T - T_b) \quad (3.50)$$

Now it is time to look into efficiencies, mostly volumetric and isentropic or power efficiency. The mass flow rate can be found with Equation 3.51

$$\dot{m} = m_{suc} \frac{n}{60} n_m \quad (3.51)$$

The power of the compressor can be set forth as shown in Equations 3.52, 3.53 and 3.54.

$$\dot{W}_{ind} = -n_m \frac{n}{60} \int_{cycle} p dV \quad (3.52)$$

$$\dot{W}_{iso} = \dot{m} R T_{suc} \ln \left(\frac{p_{dis}}{p_{suc}} \right) \quad (3.53)$$

$$\dot{W}_{is} = \dot{m} (h_{is,cond} - h_{suc}) \quad (3.54)$$

With this the isothermal and isentropic efficiencies can be found with

$$\eta_{iso} = \frac{\dot{W}_{iso}}{\dot{W}_{ind}} \quad (3.55)$$

$$\eta_{is} = \frac{\dot{W}_{is}}{\dot{W}_{ind}} \quad (3.56)$$

In this model most of the properties are found as a function of the rotation angle of the male rotor. It is possible to define a volume curve for the compression process and use the values at specific rotational angles for calculations.

3.4. MODEL USING A VOLUME CURVE

In 2017 Tian et al. [20] presented a numerical investigation on mass and heat transfer in an oil free twin screw compressor. As many other models this one also implemented liquid injection which will be neglected here. The mass and energy conservation equations are simple, what goes in should go out. The energy balance is shown in Equation 3.57.

$$\dot{m}_{suc} h_{suc} + \dot{W}_s = \dot{m}_{dis} h_{dis} + \dot{Q}_{lub} \quad (3.57)$$

It is assumed that the heat lost, released from the compressor, is all taken away by the bearing lubricant \dot{Q}_{lub} shown in Equation 3.58

$$\dot{Q}_{lub} = \dot{V}_{lub} \rho_{lub} C_{p,lub} \Delta T_{lub} \quad (3.58)$$

The isentropic efficiency is found with Equation 3.59

$$\eta_{is} = \frac{\dot{W}_{is}}{\dot{W}_s} \quad (3.59)$$

For the compressor model some aspects of the geometry must be known or estimated. The required properties are shown in Table 3.1

Table 3.1: Main parameters of compressor geometry

Compressor Design parameters
Number of lobes on male rotor
Number of lobes on female rotor
Outside diameter of rotors, d
Length of rotors, l
Centre distance of rotors, A_c
Rotation speed of male rotor, n
Shaft rotation angle of male rotor, φ

Figure 3.2 shows a schematic look into how the male and female rotors could be designed. Generally the female rotor has more lobes than the male one, so when in this hypothetical setup the female rotor makes five rotations the male rotor has six rotations.

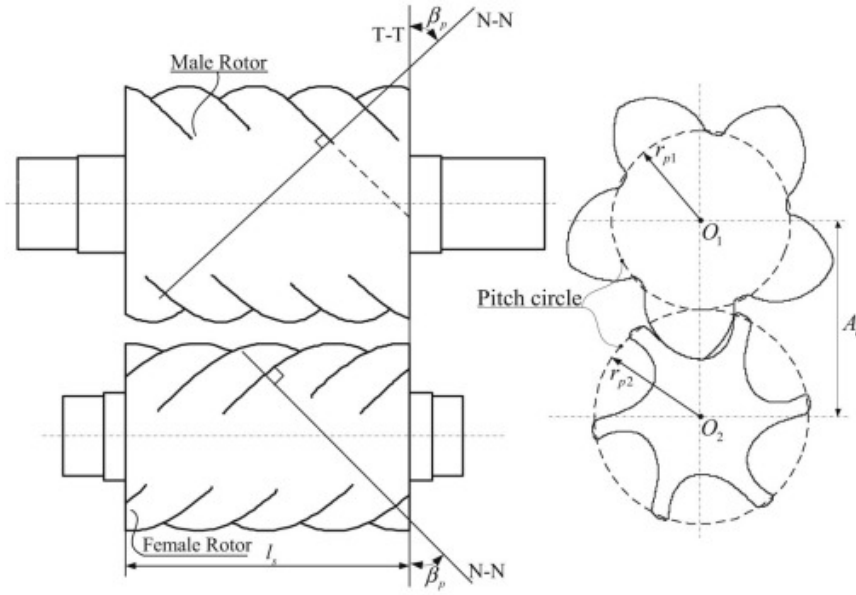


Figure 3.2: Schematic figure of how the rotors can be designed [25]

This model utilized a bit of a different approach to leakages as is shown in Equation 3.60

$$\dot{m}_l = \rho a A_l = \sqrt{\frac{p_{out}^2 - p_{in}^2}{a_s^2 \left(\zeta + 2 \ln \frac{p_{out}}{p_{in}} \right)}} \quad (3.60)$$

During the compression the equivalent volume of the practical discharge gas approaches the theoretical compression volume [20]. The time this takes is shown in Equation 3.61.

$$t_{comp} = \frac{60}{n} \frac{\varphi(V_{dis}) - \varphi(V_{th})}{360} \quad (3.61)$$

3.5. SUCTION AND DISCHARGE PORTS

In 1995 Tang [19] found a theoretical shape for a suction port of the twin screw compressor, which can be seen in Figure 3.4. This geometry was based of the volume curve he also found which is shown in Figure 3.3.

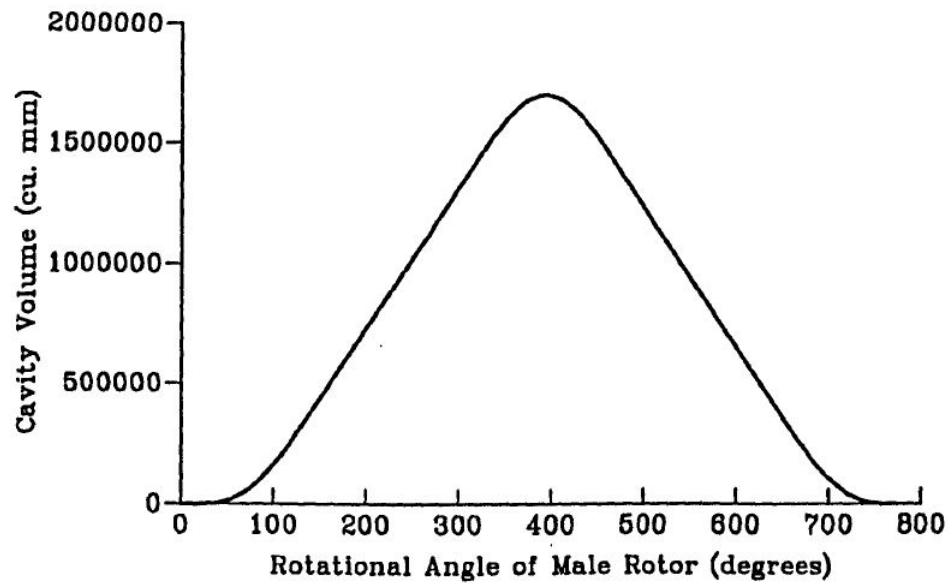


Figure 3.3: Theoretical volume curve for one cavity in the compressor [19].

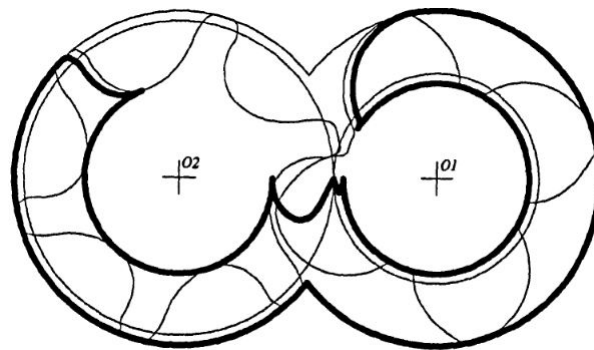


Figure 3.4: Theoretical suction port [19]

This shape is found by the meshing line on the end plane and the rotational angle of the male rotor, where the volume of the cavity is at maximum. On the female rotor there should only be one definite suction stop angle, which is calculated with Equation 3.62.

$$\alpha_{2,suc} = \alpha_{1,suc} \frac{z_1}{z_2} + \frac{360^\circ}{z_2} \quad (3.62)$$

If the angle is bigger or smaller than this stop angle it can result in less efficiency of the compressor. In Figure 3.5 the suction port area is shown as a function of the rotational angle. It is clear that for most angles the area is roughly 5000 square millimeter for this geometry

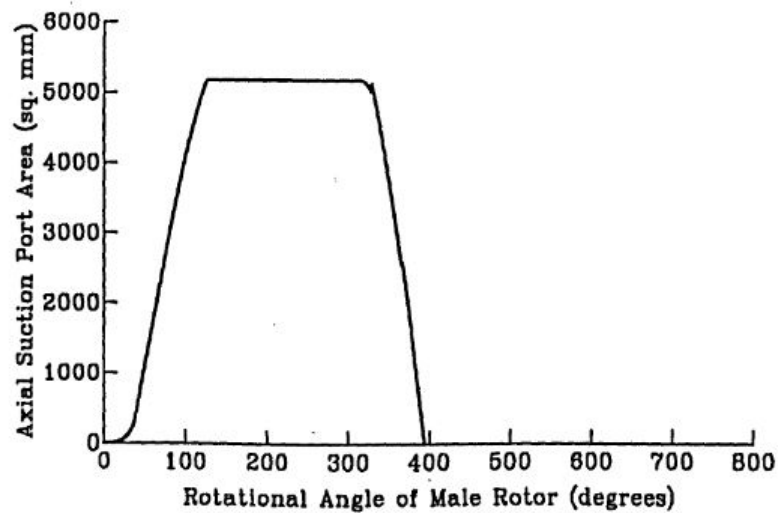


Figure 3.5: Area of axial suction port as function of rotational angle of rotor [19]

As can be expected, from the general shape of compressors, the axial suction port is larger than the discharge port. Which makes the suction resistance low. If needed it is possible to reduce that resistance even more by adding a radial suction port. Figure 3.6 shows the port size as a function of the rotational angle, for this port the area has more definite changes between different angles.

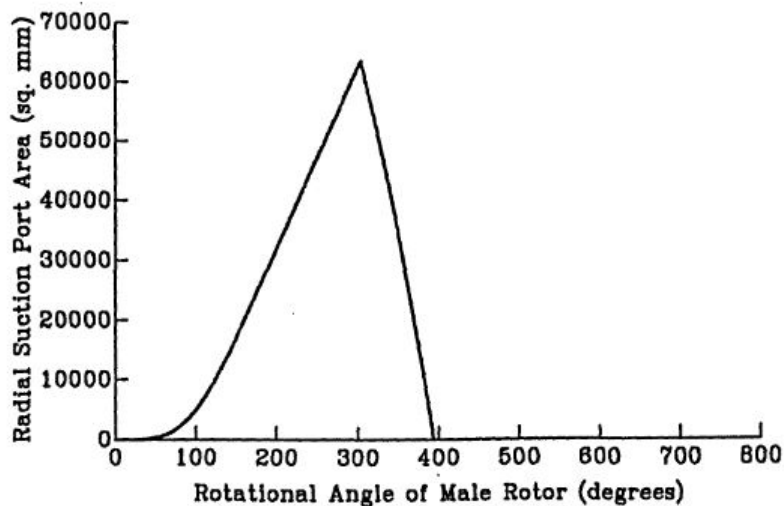


Figure 3.6: Area of radial suction port as function of rotational angle [19]

Tang [19] also quantified the theoretical axial discharge port shape. It is obtained by the meshing line on the end plane and the designed volume ratio. The theoretical shape is shown in Figure 3.7 and Figure 3.8 shows the axial discharge port area as a function of the male rotational angle.

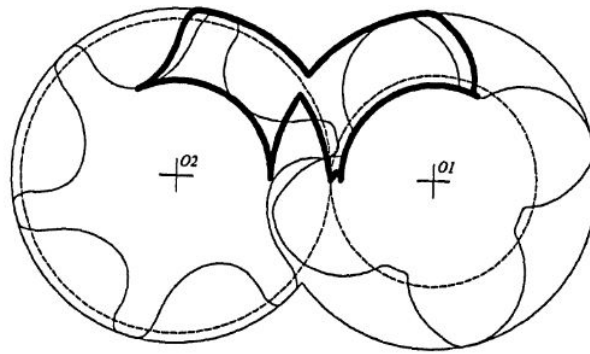


Figure 3.7: Theoretical area of discharge port [19]

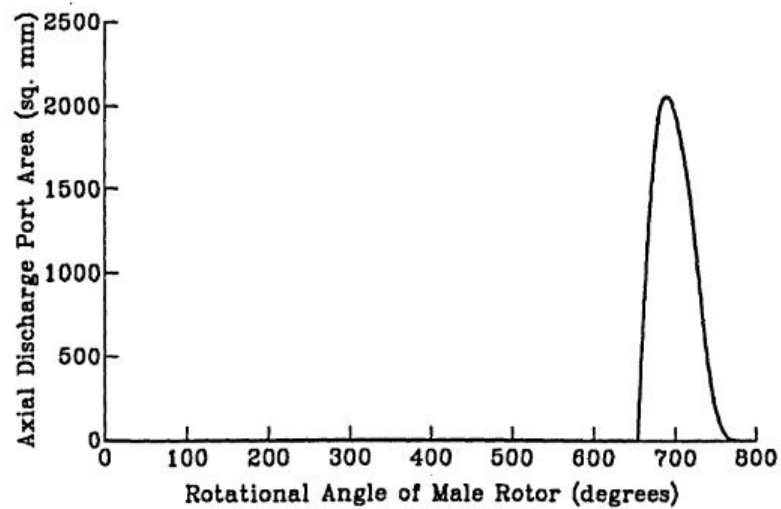


Figure 3.8: Axial discharge port as function of rotational angle [19]

In the discharge end it is also possible to have a radial port. With that it is feasible to reduce the discharge flow resistance. If needed slide valves can also be applied to control capacity. Position of the slide valves affects the shape and area of the radial discharge ports. The slide valve by-pass is closed under full load conditions but partially open under partial loads. In Figure 3.9 the radial discharge ports and the slide valve by pass ports are shown as function of the rotational angle.

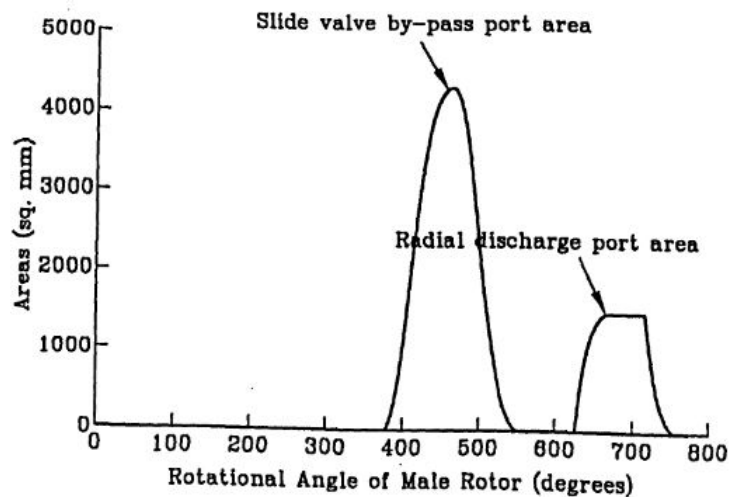


Figure 3.9: Area of slide valve by pass and radial discharge ports as function of rotation angle of rotor [19]

However in the compressor intended for this study there is no slide valve, so for implementation that geometry will be left out.

Zaytsev [26] also did some analysis on the geometry of this type of compressor. He utilizes very similar port shapes as well as the shape of the graphs made as function of the rotational angle. The main difference between these two is the size of the compressor. Zaytsev had a rather small compressor, especially when compared to the one used by Tang [19] which is roughly five times larger, according to the port areas.

The current compressor has a minimum inflow of $90 \text{ m}^3/\text{h}$ and a maximum of $400 \text{ m}^3/\text{h}$. The two models are used together to scale the geometry close to the size of the compressor size.

3.6. POSSIBLE LEAKAGE PATHS

Between the compressor housing and the grooves of the two helical rotors there is always a bit of clearance, this must exist to compensate for machining tolerance, force deflection and thermal expansion [4]. Through this space it is possible for some of the working fluid to leak through. In the model it is necessary to try to account for these leakages and all possible pathways should be looked into. In 1995 Tang [19] identified 6 possible leakage paths for a twin screw compressor utilizing the same control volume of a cavity bounded by the housing, housing bores and helical rotors.

Path 1 Contact line between male and female rotors.

Path 2 Sealing lines between the rotor tips and housing bores

Path 3 The cusp blow hole

Path 4 The compression start blow hole

Path 5 Clearance between the end plate and the rotor end face at the suction end

Path 6 The clearance between the end plate and the rotor end face at the discharge end

In Figure 3.10 the location and connection between the different leakage paths is schematically given.

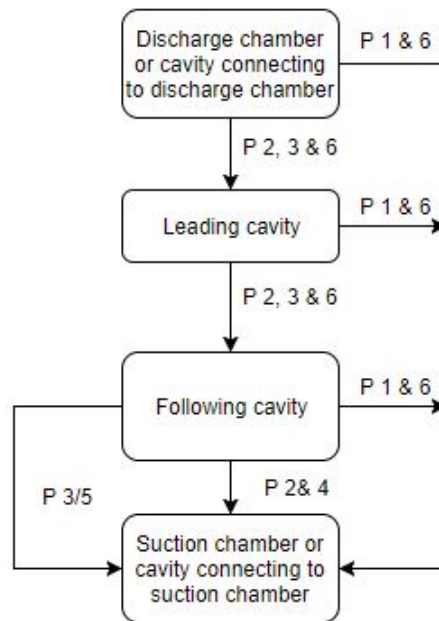


Figure 3.10: Schematic diagram of possible leakage paths in a twin screw compressor[19]

For this current study path 5, leakages at the end plate at the suction side, is neglected as the pressure changes in the suction cavity are quite small. Tang [19] plotted the various sealing lines and areas for the blow holes which can be used for calculations.

In Figure 3.11 the contact line between male and female rotor is shown. This path is one of the major components of leakage inside the compressor. The area of this path is found by multiplying this contact line with the clearance between the rotors. In order to keep things simple an average clearance is assumed, since it might be a bit different in different places of the rotors. This clearance is generally rather small, here around 50 micrometer will be used.

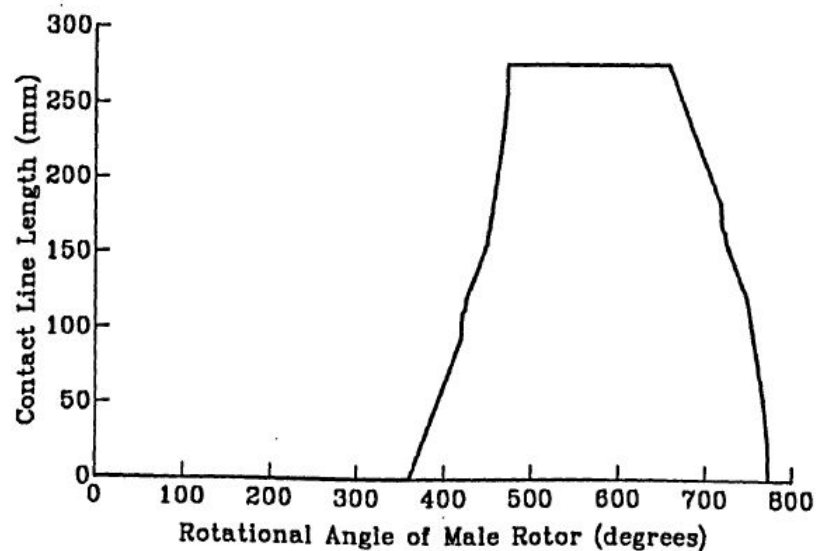


Figure 3.11: Length of contact line over the compressor [19]

The next leakage path is between the male and female rotor tips and the housing bore, this is found similarly as the contact line by using the sealing line and average clearance. The sealing lines for both male and female rotors are shown in Figure 3.12.

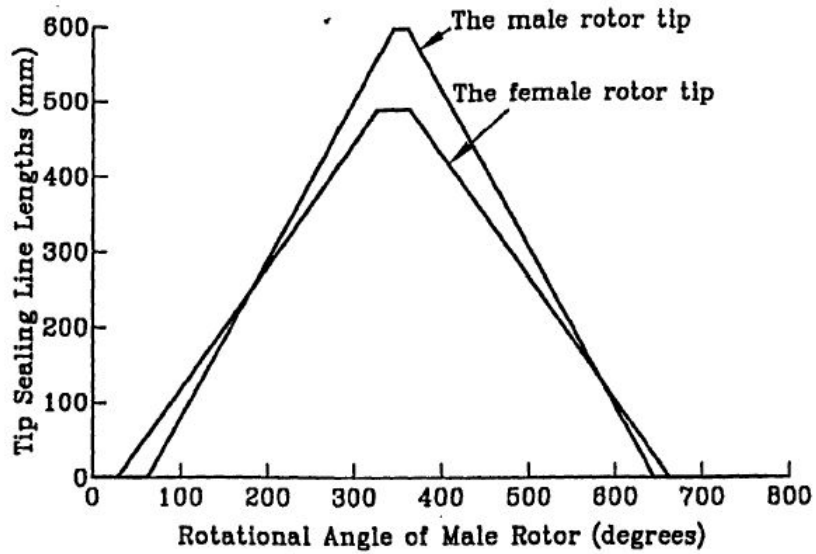


Figure 3.12: Sealing lines for male and female rotor tips [19]

Figures 3.13 and 3.14 show the area of the blow hole for the high and low pressure sides, the low pressure side also being called the start of compression. This area forms between the rotor tips and the housing cusp [19].

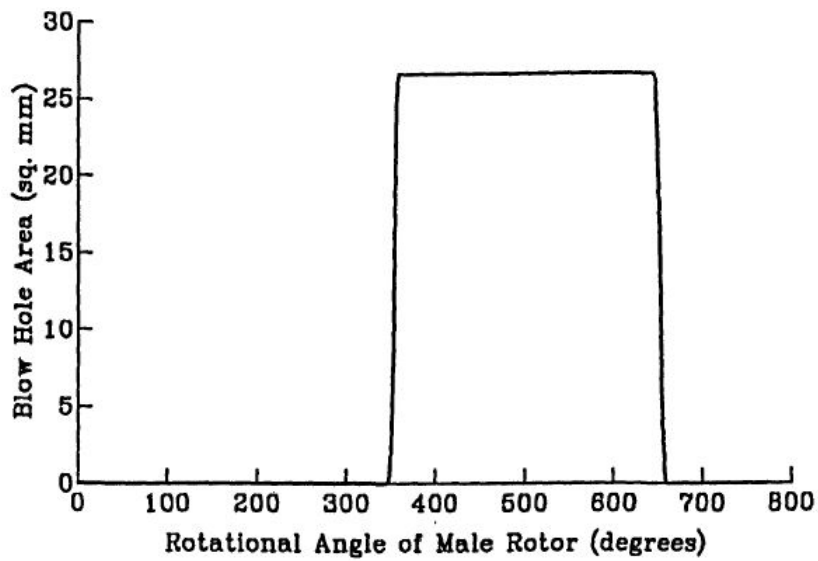


Figure 3.13: Area of blow hole [19]

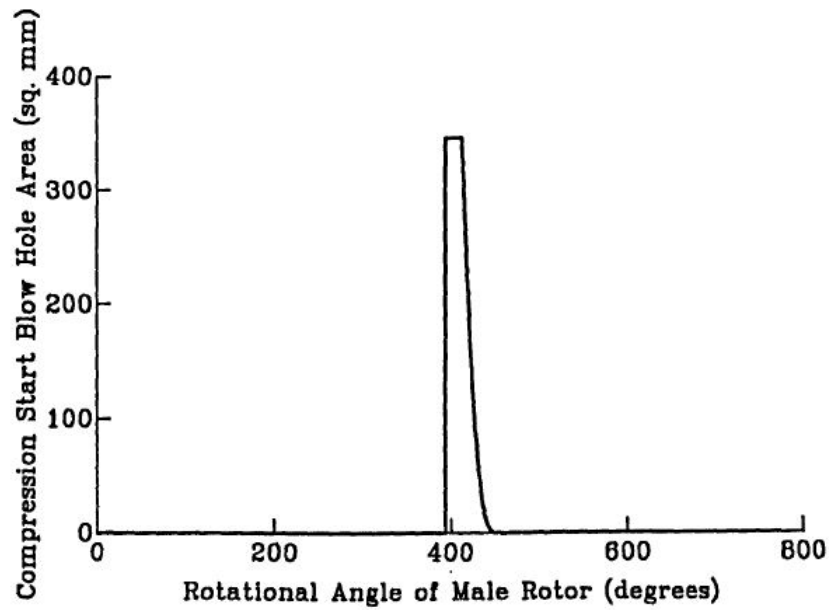


Figure 3.14: Blow hole area at start of compression [19]

The final leakage path is related to the end planes and is divided into four curves. Each curve, shown in Figure 3.15 is multiplied with an average clearance in order to find the leakage area.

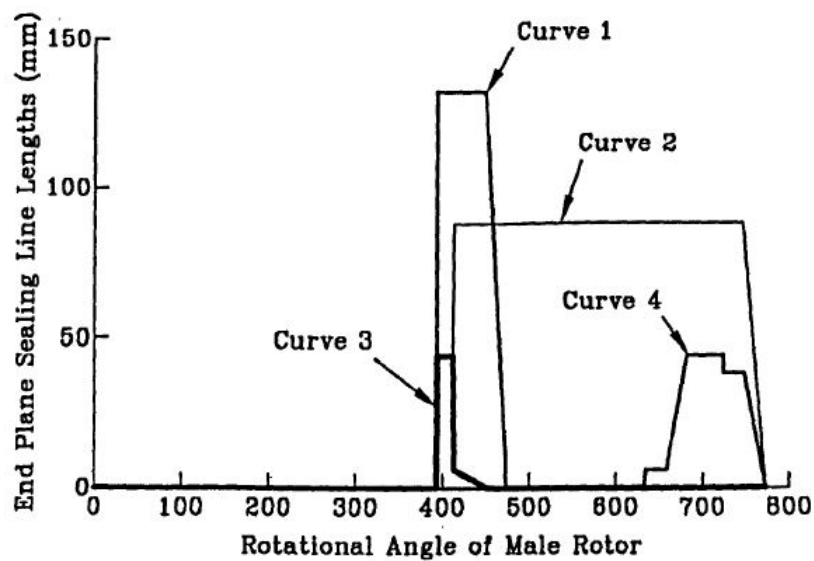


Figure 3.15: Contact lines for all possible end plane leakages [19]

Curve 1 is the length of the rotor end plane sealing line at the suction side. Curve 2 is the sealing line between the leading cavity to the following. Then during the beginning of compression curve 3 shows the sealing line from the discharge chamber to the enclosed cavity. Finally for the leakages that go straight from the discharge to suction phase have the sealing line shown with curve 4.

3.7. MODEL COMPARISON

In the past sections a few models have been put forward, all with different possibilities and various difficulty levels as well as needed inputs. Comparison of these models is listed in Table 3.2.

Table 3.2: Comparison table for the possible models

Model	Works with liquid	Accounts for leakages	Has experimental data	Calculates required efficiencies	Geometry of compressor required
Zaytsev	Liquid refrigerant	Yes	Yes, some	Yes	Yes, very detailed geometry used
van de Bor et al	Liquid refrigerant	No	Has some data, not during compression process	No	No
Chamoun et al	Yes	Yes	Yes, some	Yes	Vaguely used, not detailed
Tian et al	Yes	Yes	Data from experiments	Yes	Used, quite general
Tang	Oil or liquid refrigerant	Yes	Yes	Yes	Uses geometry, with some assumptions

First the quite detailed model from Zaytsev [26] was examined. His model is very detailed and requires rather accurate details regarding the geometry. It was designed to be used with liquid injection but that part has been left out. However considering the overall comprehensiveness of this model, it would need more detail than is available in this study.

Alternatively the model by van de Bor et al. [24] is probably too simple, as it is only focusing on the conditions before and after the compressor and not at all what is happening during compression. However, it is still possible that this model might be partially used for those general conditions.

The next two models from Chamoun et al. [4] and Tian et al. [20] both seem to be a nice fit for this study. They do model the actual compression process, without being too dependent on an exact geometry. In the end the model by Chamoun et al. might be more applicable since it is more clearly focused on compressor side while the second model has more focus on droplets formed during the process, which will not be looked into in much detail here.

Finally to model the leakages the models by Chamoun et al., Tian et al. and Tang [19] do all look into the possible leakages. The first two models do so quite quickly with a single equation while Tang does look more deeply into where and how those leakages are happening.

Tang did also find an approach to the geometry of the compressor which is quite general and could be used for this study.

4

IMPLEMENTATION OF COMPRESSOR MODEL

After looking through all the possible models and deciding which one would be appropriate for the current study, the next step is to implement it.

As stated in the model comparisons in Chapter 3.7 the model by [Chamoun et al. \[4\]](#) seemed to be the best solution. By keeping the equations and solving methods simple, the calculation time can be shorter than in some more complex approaches.

In Figure 4.1 a general overview of the inputs and outputs of the model are shown. It also displays the flow between different components. In order to get the thermodynamic properties of the mixture at various pressures and temperatures the model by [Ziegler and Trepp \[27\]](#) is used by taking properties from the current control volume and returning the needed properties back into the model.

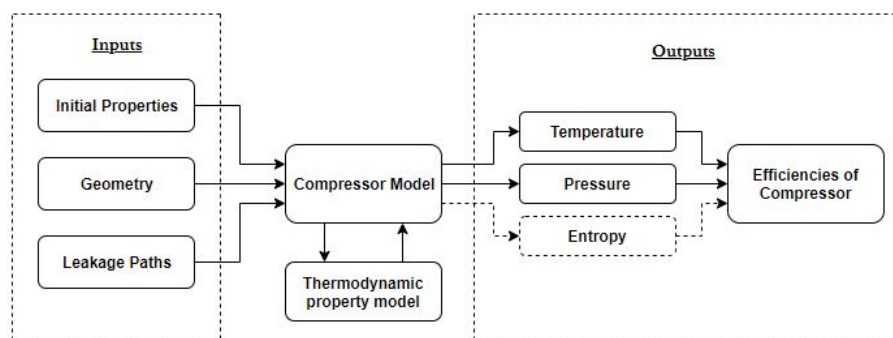


Figure 4.1: General overview of the model components. With three main inputs, the inlet properties such as temperature and pressure, general geometry of the compressor and the leakage paths. The calculation model in the middle which uses the thermodynamic model from [Ziegler and Trepp \[27\]](#) and returns the desired outputs used in efficiency calculations.

The software Matlab [13] was selected to build the model, as it should be easily able to do the level of calculation needed and if necessary could connect with Refprop [11] for properties that could not be found with the model of [Ziegler and Trepp \[27\]](#).

The model by [Chamoun et al. \[4\]](#) was previously determined as the most suitable approach, in practice it did not work quite as expected. With only their approach the model results did not converge. This was solved by merging it together with another model, different pieces of the two models used together. The more simple solving strategy from [Chamoun et al. \[4\]](#), small sections evaluated at a time and added together, is used to solve the conservation equations derived by [Zaytsev \[26\]](#).

Some knowledge of the compressor geometry is needed for the calculations, [Zaytsev \[26\]](#) has a way of calculating close to exact geometry this however needs a lot of information about the actual geometry. This

information is not always readily available, thus a simpler approach is preferred. A rough estimation of the volume curve, leakage paths and port areas is enough for this level of model details. As was suggested during the comparisons in Chapter 3.7 Tang [19] constructed graphs for all leakage paths in the compressor at all rotational degrees. Comparing the volume, leakage and port areas between Zaytsev and Tang they seem to be comparable and related to the different sizes of compressors.

The graphs from Tang [19] are used as a format, which can be referenced to get the value at a specific position for the calculations in the model. Using this format it is possible to scale the compressor size, and change the start or stop angles for different compressors.

4.1. CONTROL VOLUME

Here the solving method utilizes finite volume to calculate the changes during the compression process, by using conservation equations for mass and energy. The compressor cavity is divided into multiple small finite control volumes of equal sizes. By splitting the cavities into such small units it is possible to use simpler steps for calculation as it is done inside each control volume.

Initially the maximum for each control volume was the size of one degree of rotation. However, in order to be certain that the results are stable the size of each control volume needs to be even smaller. After running various tests the range where results start to become stable is around 8000 and 40000 steps. This can then differ a bit with different input conditions.

The time it takes to run through the simulation is linked with the number of control volumes, with fewer and bigger units the simulation can finish faster. However, they cannot be too big as the results can be higher than they should be as they have not reached convergence.

With smaller geometries the control volume becomes more sensitive. When the step size is too small the calculations can explode and then the results are skewed. For this reason the step size was improved to be able to include various step sizes. With this it was possible to have smaller step sizes where needed and the results still converge correctly and with quicker computational time.

4.2. IMPLEMENTATION

In this section generation of the model is explained, as well as what steps the process goes through.

First an initial cycle of the compression process must be run, in order to get values throughout the compression process to work with at later stages. After those values are obtained then the leakages and heat can be added to the process. Now using the previous cycle for calculations the whole process is iterated until the change between cycles is within 0.01 Pa. In Figure 4.2 this process is described.

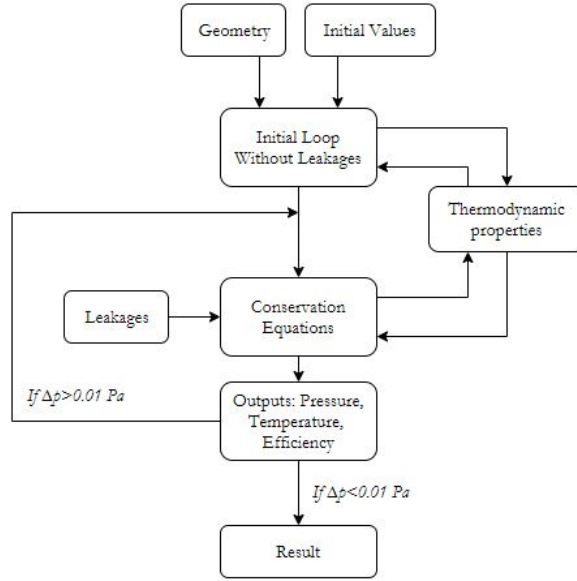


Figure 4.2: More detailed representation of the compressor model. The geometry and initial values are used for the initial loop without leakages to get values to start with at all points in the compressor. The output from the initial loop is used in the main model which iterates until the values have converged, or the pressure difference between iterations is less than 0.01 Pascal. Both models use the thermodynamic model.

The pressure and temperature of the inlet are put in as initial conditions in order to start the first simulation. The use of the compressor geometry is simplified for more convenient and quick calculations and mainly the volume curve is used. These components are then inputs for the initial cycle.

A number of assumptions must be made to start the simulation. During the initial cycle no leakages are accounted for, as the pressure in the following cavity must be known for those calculations. Thus the suction and discharge phase are assumed to be constant.

During the compression phase conservation equations for mass and energy are solved for the change in pressure and temperature for each step. The difference is added to the current value of temperature or pressure to calculate the value in the next step. Then the new pressure and temperature values are used with the thermodynamic model to find the other properties.

As the mass flow into the system is not known and properties are considered stable throughout the suction process the density is constant and can be found by using the pressure and temperature at the inlet. Then with the maximum volume known from the volume curve the mass at the start of compression can be calculated with Equation 4.1

$$m = \frac{V_{max}}{\rho} \quad (4.1)$$

Now that the mass is known, it is possible to rewrite the equation inside the compression cycle so that it uses the current volume and the mass to find the specific volume at the present place inside the compressor which is used in the conservation equations.

To solve the mass and energy conservation equations various partial differentials of the thermodynamic properties are needed. In order to calculate this a five-point stencil based algorithm, which is often used in numerical analysis, is used. It uses the point, where the partial derivative is taken, and its four neighbors to write finite difference approximation to derivatives [5]. For this study only the first order derivative is needed, using the five-point method the partial derivative can be found with the formula shown in Equation 4.2 [5]. Where y is the space between points in the grid and x is the current position.

$$f^{(1)} = \frac{f(x-2y) - 8f(x-y) + 8f(x+y) - f(x+2y)}{12y} \quad (4.2)$$

In the current model there are three partial derivatives used, $\frac{\partial h}{\partial T}(x,p)$, $\frac{\partial v}{\partial p}(x,T)$ and $\frac{\partial v}{\partial T}(x,p)$. The thermodynamic models need three inputs in order to calculate a property, two are kept constant while the third varies during the five point method calculations. As this study uses a constant ammonia concentration, x , that is always one of the constant variables and the other is either pressure or temperature depending on the derivative.

Thus, the variable y in Equation 4.2 is either change in temperature, when the partial derivative is dependent on temperature, or pressure for the other case. These properties have different limits on the step size, y , for them to stay consistent without large deviation. These limits were iterated until a good step size was found for each value.

Now the only thing left is to solve the conservation equations for the change in temperature and pressure. To do this the Euler method is used, which is a first order numerical procedure often used to solve ordinary differential equations. Equation 4.3 shows the forward finite difference formula that is used to calculate the change in pressure or temperature over the change in rotational degree of the male rotor.

$$f'(\varphi) = \frac{f(\varphi + d\varphi) - f(\varphi)}{d\varphi} \quad (4.3)$$

This can be used as the conservation equations are both first order derivatives and the step size used is very small. For each step in the compressor this method is used to find temperature and pressure in the next step.

The Euler method equation is then rearranged so that the next step is calculated by using the derivative, step size and value of the current step.

When the initial cycle has run its course, the base values for the whole compression process are available and can be used for further calculations.

In order to calculate the leakages in and out of the current position the pressure in the next or previous cavity is needed, depending on whether the fluid is leaking in or out. As was shown in Figure 3.10 the leakages flow from the discharge end and towards the suction, this happens because of the pressure difference between the cavities. The flow goes from the high pressure side to the low pressure side through the corresponding leakage path depending on where in the compressor it is flowing.

With the leakages accounted for, the full conservation equations can be used as are shown in equations 4.5 and 4.4.

$$\frac{dT}{d\varphi} = \frac{T \left(\frac{\partial v}{\partial T} \right)_{p,x} \left(\frac{v}{m} \left(\sum_{k=1}^n \left(\frac{dm_{out}}{d\varphi} \right)_k - \sum_{k=1}^l \left(\frac{dm_{in}}{d\varphi} \right)_k \right) + \frac{1}{m} \frac{dV}{d\varphi} \right) + \frac{\partial Q}{\partial \varphi} + \sum_{k=1}^l (h_{in,k} - h) \left(\frac{dm_{in}}{d\varphi} \right)_k}{\left(\frac{\partial v}{\partial p} \right)_{T,x} \left(\frac{\partial h}{\partial T} \right)_{p,x} + T \left(\frac{\partial v}{\partial T} \right)_{p,x}^2} + \frac{m \left(\frac{\partial h}{\partial T} \right)_{p,x} + \left(\frac{\partial v}{\partial p} \right)_{T,x} \left(\frac{\partial v}{\partial T} \right)_{p,x}^2} \quad (4.4)$$

$$\frac{dp}{d\varphi} = \frac{1}{\left(\frac{\partial v}{\partial p} \right)_{T,x}} \left(\frac{v}{m} \left(\sum_{k=1}^n \left(\frac{dm_{out}}{d\varphi} \right)_k - \sum_{k=1}^l \left(\frac{dm_{in}}{d\varphi} \right)_k \right) + \frac{1}{m} \frac{dV}{d\varphi} - \left(\frac{\partial v}{\partial T} \right)_{p,x} \frac{dT}{d\varphi} \right) \quad (4.5)$$

Now that the full equations are available, the suction and discharge phases are added as well. The mass flow per rotation is found with Equation 4.6, which uses Equation 4.7 [26], in order to calculate the mass flow rate.

$$\frac{dm}{d\varphi} = \frac{CA\rho a}{\omega} \quad (4.6)$$

$$a = \sqrt{2 * v * \Delta p} \quad (4.7)$$

The mass flow is calculated for the flow that leaks in and out of the cavity and the mass entering or leaving during suction. As said before the pressure difference drives the flow and is the main component in the

velocity calculations, it looks at the pressure from the previous or next cavity and the pressure in the current position. As the suction and discharge phases were considered constant during the first cycle they don't have any velocity calculated since there is no pressure difference, except in the cavity next to the compression phase.

In the initial cycle calculation the total mass was assumed, as shown in Equation 4.1. When the suction and discharge phases are taken into account the mass is calculated. With the suction and discharge ports it is possible to calculate the mass in or out of the compressor. Equation 4.6 is used for this calculation, same as for leakage paths except different areas. This calculates the change in mass over the change in rotation, $\frac{dm}{d\varphi}$, then by multiplying with the current step size the difference in mass at that point is found. This difference is then added for each step in the respective phase to see how much mass has entered or left the system.

However, at these phases the ports are still open so both during suction and discharge it is necessary to assume that mass can leak in or out. Mass already inside the compressor can leak out during suction and some mass outside the compressor can leak in as well during discharge.

Then the whole process is iterated until it converges, using the results from the previous run to calculate the next cycles values. With these iterations the pressure difference in the suction and discharge is influenced more and more with each iteration. When the pressure differences cover more of the suction and discharge the leakages can be calculated throughout the whole process

The iteration runs until the pressure difference around half way through the compression between iterations is less than 0.01 Pa. With the current simple approaches used in the model the whole process is relatively quick.

When the cycle has converged with an acceptable small difference between runs, the final property values are obtained and can be used for further calculations. Next step is to calculate the efficiencies of this process, the models from Zaytsev [26] and Chamoun et al. [4] use almost the same equations to calculate the various efficiencies. However, since the latter model has more assumptions the equations are also simpler and not as relevant to the conservation equations used in the model, therefore, the equations from Zaytsev [26] are used, see Chapter 3.

The first step is to find the mass flow rate inside the compressor, this is done with Equation 4.8.

$$\dot{m} = z_1 \frac{n}{60} \int \frac{dm}{d\varphi} d\varphi \quad (4.8)$$

Here the change in mass for each step during suction is added and multiplied with the number of lobes and angular rotation speed in order to get the mass flow of the compressor. The total mass added during suction should be the same as if the total mass during discharge would be added up.

Next the efficiencies are found, see in Chapter 3 the equation and explanations. The isentropic and indicated power are found with Equations 3.15 and 3.16. The isentropic enthalpy, h_{is} , is found by calculating the entropy during suction, this entropy would stay constant under isentropic compression, so by using the discharge pressure and this entropy the isentropic enthalpy is found. To find the indicated installation power, in Equation 3.16, the pressure is integrated over the volume, this can be done similarly as how the mass was integrated earlier.

When considering the power losses due to friction it is possible to calculate them as Zaytsev did. However, that does need some detailed information about the bearings and seals. Regularly in this sort of studies the mechanical efficiency is assumed, Chamoun et al. [4] used a mechanical efficiency of 90% and that corresponds to many other studies such as Tang [19].

Finally the compressor efficiencies are calculated. Equations 3.20 and 3.21 are the isentropic efficiencies of the compressor and compression installation respectively and 3.22 is for the volumetric efficiency [26].

4.3. VALIDATION OF THE MODEL

Finally the model needs to be validated to see if the results are comparable to reality and can be trusted. Generally there are three approaches to validate a model, expert intuition, real system measurement and theoretical results or analysis [9].

The original plan was to validate the compressor model with experiments as the compressor is a prototype. Currently there is not any available data for this sort of compressor and the chosen mixture. Unfortunately the experimental part of this study is as of writing this report not yet viable, so it cannot be conducted.

With this rises a problem, how can the model be validated. For now the most suitable approach is a comparison of some trends, such as efficiency calculations. For these comparisons the book "The design and application of rotary twin-shaft compressors in the oil and gas process industry" by Arbon [2] is used. There he examined how various twin shaft compressors, including the oil free screw compressors, behave for different conditions.

Arbon explored how the efficiencies, internal and volumetric, change with increased pressure ratios or rotational speed. These parameters can also be examined with the model made in this study. However, the working fluid that Arbon uses is in the gas phase, not the two phase region as is examined in this study. Also the mixture used in the current study is a mix of ammonia and water not a pure fluid. Nonetheless the trends should be similar between the two, thus it can be used as a form of validation.

First the efficiencies at different pressure ratios were examined. The discharge pressure was varied while the suction pressure remained constant for both the reference case and the model. Figure 4.3 has the isentropic and volumetric efficiencies for different pressure ratios as presented by Arbon [2]. While the volumetric efficiency curve has a small decline it is still rather stable. The isentropic curve is more parabolic, with the efficiency rising quickly until it reaches a maximum around the pressure ratio 3 and then a slower decrease in efficiency with higher ratios. The internal pressure ratio is 3, which is where the peak is, this shows how the efficiency is effected when the compressor is operated outside that point.

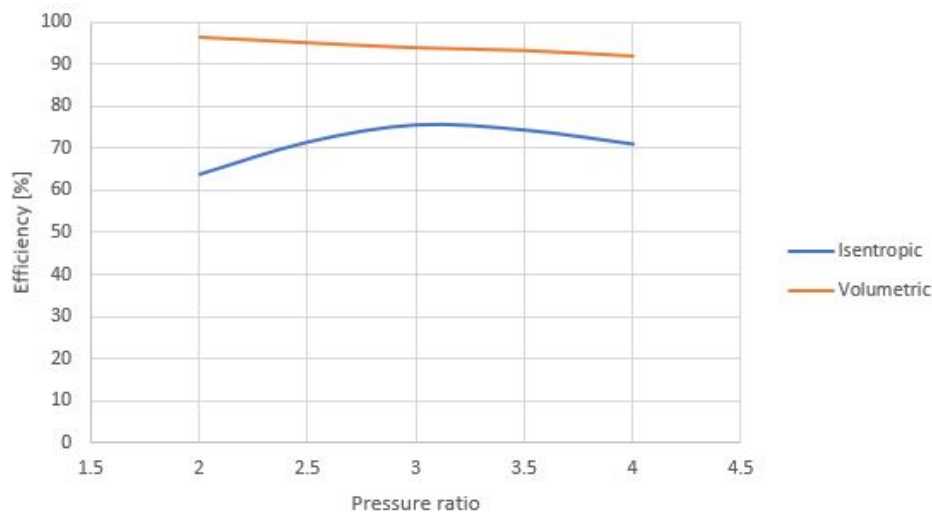


Figure 4.3: The isentropic and volumetric efficiency for different pressure ratios as estimated by Arbon [2]. The volumetric efficiency decreases slightly with increased pressure ratio. While the isentropic efficiency has more of a curve, with it increasing quickly until a maximum is reached at a pressure ratio of 3, then it starts decreasing slowly with higher ratios.

Figure 4.4 shows the efficiencies obtained with the model. A similar trend is seen here with the isentropic efficiency, where it gets a peak and the under- and overcompressed points result in lower efficiencies. The same trend is seen where the efficiency increases quickly until it reaches the peak and then slowly decreases. The volumetric efficiency is however very stable for the different ratios. As the volumetric efficiency is acquired from the suction phase, this could be due to the initial mass flow assumptions as the first values during suction are stable and do not vary a lot during the process. This could also be due to different working fluids, that the suction phase is less steady for other fluids.

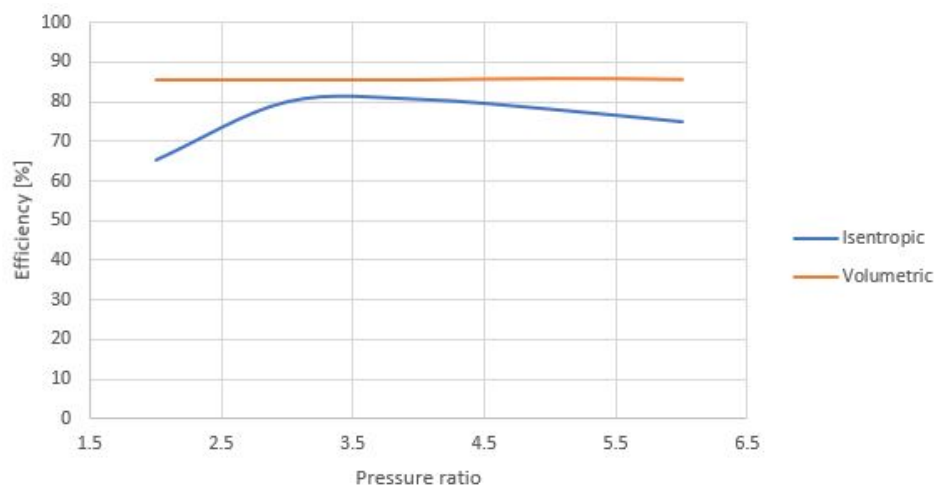


Figure 4.4: The isentropic and volumetric efficiencies at different pressure ratios, for the current model. The volumetric efficiency is rather stable for all the different pressure ratios. The isentropic efficiency reaches a maximum around 3.5 with a small decline in efficiency for higher ratios.

In Figure 4.5 the isentropic efficiency curves for both versions are shown together. While they are not identical they do follow the same trend.

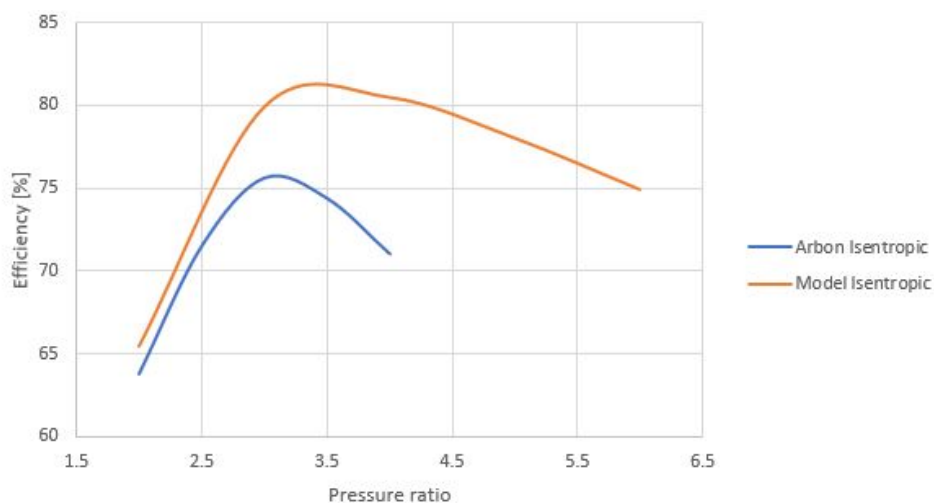


Figure 4.5: A comparison of the isentropic efficiency between the generated model and the values from Arbon [2]. The model has higher efficiencies than the ones from Arbon. However, both curves seem to follow the same trend. Both reach a maximum quickly, at pressure ratio around 3-3.5, then the efficiency slowly declines with higher ratios.

Next the change in discharge temperature with varying rotational speeds is examined. Arbon [2] uses percentages to show the speed, with the range 70-100% as the normal operation range. This is seen in Figure 4.6, where a clear decrease in discharge temperature is distinct. The temperature decline gets smaller when the rotational speed is in the higher values.

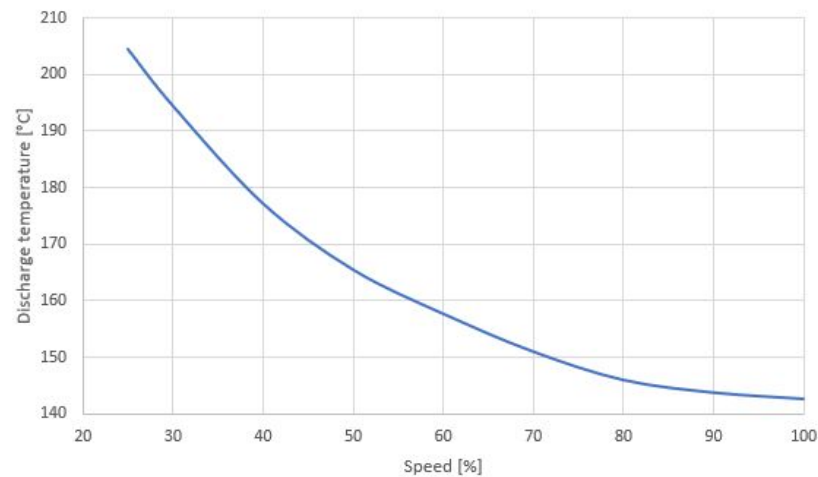


Figure 4.6: The discharge temperature as a function of the rotational speed [2]. [Arbon](#) expresses the speed as percentages with a range between 70 - 100% being the norm. A steady decline is seen in the curve with lower compressor rotational speeds resulting in higher discharge temperatures. The temperature starts to stabilize at the higher speeds.

Figure 4.7 presents the discharge temperature as a function of the rotational speed as calculated with the model. Here a similar trend can be seen. The temperature decreases considerably with a small increase in rotational speed in the beginning and then the temperature starts to level out with increased rotational speed.

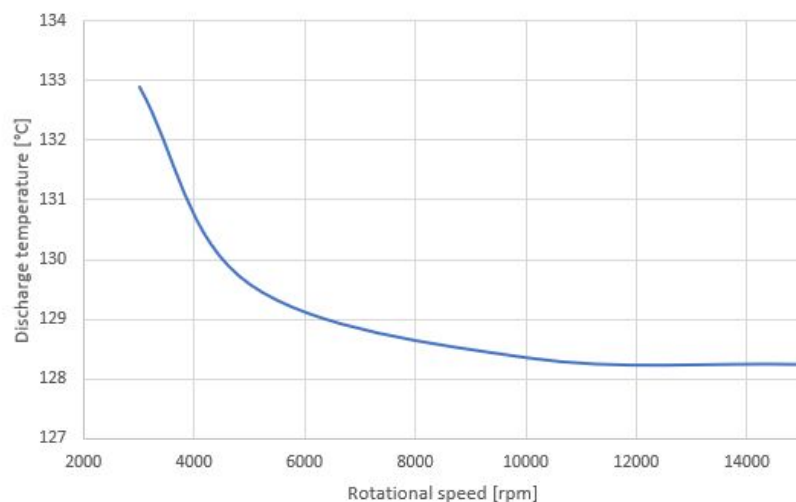


Figure 4.7: Discharge temperature as a function of the rotational speed. Here the rotational speed is shown in rotations per minute with the typical operating speed around 10000rpm. A quick decrease in temperature is seen in the beginning when the speed is increased, which starts to stabilize with higher rotational speeds.

After comparing these different variables, a similar trend can be seen between the model and the results from [Arbon](#). Based on this it can be estimated that the compressor model represents the behavior of an oil-free twin-screw compressor adequately. The values themselves are not identical, as the working fluid and conditions are different, but do follow the same trends.

5

MODEL RESULTS

When the implementation of the model is complete the results of the model can be examined. With the lack of geometry information on the compressor used in the study the initial calibration of the model was done with the larger geometry explained in Chapter 3.

When the volume of the compressor used in the study was known, the geometry was scaled to fit the new volume in order to use the model. A difference from the geometry explained in Chapter 3 is in the discharge port, the compressor used in the study is much smaller than the compressor used by Tang and so it will most likely not be able to account for an axial discharge port so that has been left out and only a radial discharge port is used.

The leakage paths have been estimated by using the ratio to the maximum volume per cavity as calculated from Zaytsev [26].

The model was tested for a few different conditions that are shown in the following section.

5.1. EFFECT OF AMMONIA CONCENTRATION

First the effect of ammonia concentration was examined, the properties used for the following calculations can be seen in Table 5.1.

Table 5.1: Properties used for comparing calculations under different ammonia concentration conditions. After the stop angle the properties are assumed stable. The ammonia concentration is varied from 20 to 40 % while other variables are kept stable.

Maximum volume per cavity	0.000058m ³
Discharge opens at	690 °
Stop angle	780 °
Clearances	50 μm
Suction pressure	1 bar
Suction temperature	Varies
Suction vapor quality	48%
Discharge pressure	5 bar
Ammonia concentration	20 wt%, 30 wt%, 40 wt%
Number of cavities	5
Rotational speed	10000

The pressure as a function of the male rotational angle for the whole process is shown in Figure 5.1. The suction vapor quality, suction and discharge pressure are constant for all three curves. As can be seen in the figure the three curves overlap completely, so the pressure is not really effected by the concentration.

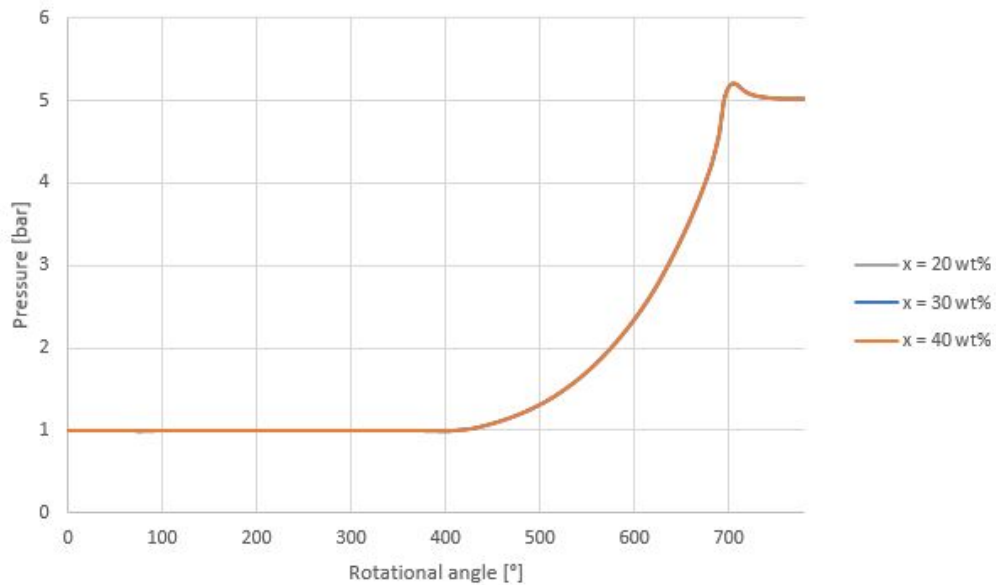


Figure 5.1: Pressure as a function of the male rotational angle for different ammonia concentrations. Three different ammonia weight percentages were examined, 20, 30 and 40 wt%. All three have the same inlet conditions and discharge pressure. As can be seen the pressure curves overlap almost completely.

Figure 5.2 shows the temperature change over the process. To keep the same suction vapor quality for comparisons the inlet temperature is varied a bit. The overall trend seems to be very similar between the different concentrations, except with lower ammonia concentration the temperature increases more to reach the same discharge pressure.

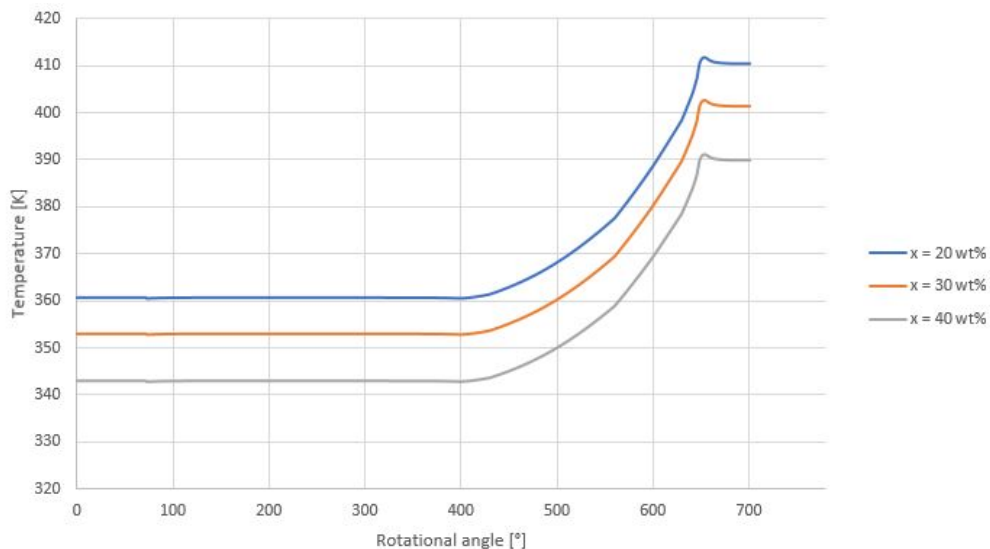


Figure 5.2: Temperature as a function of the male rotational angle for different ammonia concentrations. Three different ammonia weight percentages were examined, 20, 30 and 40 wt%. All three have the same inlet conditions and discharge pressure. In order to have the same suction vapor quality the temperature varies after that the trend seems similar between the different mixtures.

The same is noticed in the vapor quality, shown in Figure 5.3, that the trend is similar with a slightly larger increase for the lower ammonia concentrations. However the increase in vapor quality over the compression process is very low, only around 1% increase.

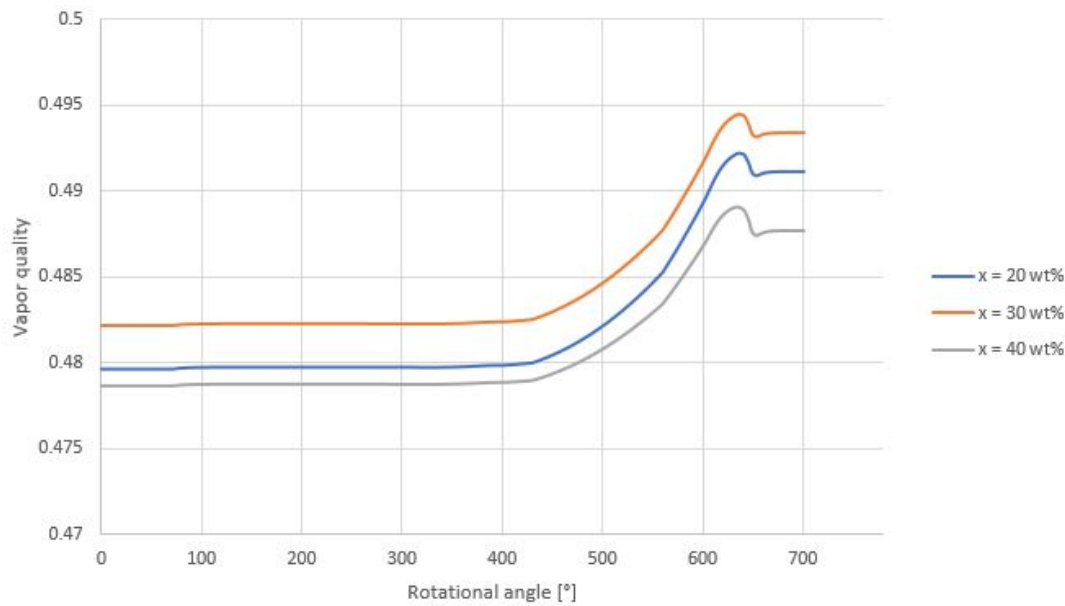


Figure 5.3: Vapor quality as a function of the male rotational angle for different ammonia concentrations. Three different ammonia weight percentages were examined, 20, 30 and 40 wt%. All three have the same inlet conditions and discharge pressure. The rise in vapor quality is minimal, however it seems to be a slightly larger difference with more ammonia concentration.

Finally the efficiencies are considered, an overview of the isentropic and volumetric efficiencies for the three different ammonia concentrations. For all following isentropic efficiency calculations Equation 3.20 is used and mechanical efficiency is not included.

Table 5.2: Overview of the different isentropic and volumetric efficiencies for the three different ammonia concentrations explored before. The isentropic efficiency is around 75% with a small decrease for higher concentration. The same can be seen in the volumetric efficiency with a slightly smaller decrease with increased ammonia concentration.

Ammonia Concentration [wt%]	20	30	40
$\eta_{is,com}$ [%]	75.14	74.90	74.80
η_{vol} [%]	85.97	85.97	85.96

Overall the efficiencies are almost the same for different ammonia concentrations, with a slight decrease with higher ammonia concentrations. This is more noticeable in the isentropic efficiency but can also be noticed in the volumetric efficiency. The reason for this is the amount of water, as with less ammonia the vapor quality is more sensitive to changes and in proportion to the others the 20wt% ammonia concentration curve has a larger increase in vapor quality.

5.2. EFFECT OF CLEARANCES

In Table 5.3 is an overview of the properties used for calculating the effect of different clearances in the leakage paths.

Table 5.3: Properties used for comparing calculations for different clearances for leakage paths. After the stop angle the properties are assumed stable. The clearances are examined at 50, 100 and 200 micrometers.

Maximum volume per cavity	0.000058m ³
Discharge opens at	690 °
Stop angle	780 °
Clearances	50 μm , 100 μm, 200 μm
Suction pressure	1 bar
Suction temperature	70°C
Suction vapor quality	31%
Discharge pressure	5 bar
Ammonia concentration	40 wt%
Number of cavities	5
Rotational speed	10000
Flow coefficient for leakage paths	0.8

Figure 5.4 has the pressure for the different clearances. Here a difference can be seen during the compression phase as more leakages occur for larger clearances. Figure 5.5 shows the temperature which has a similar trend a noticeable difference during the compression phase, resulting in a higher temperature need for larger clearances

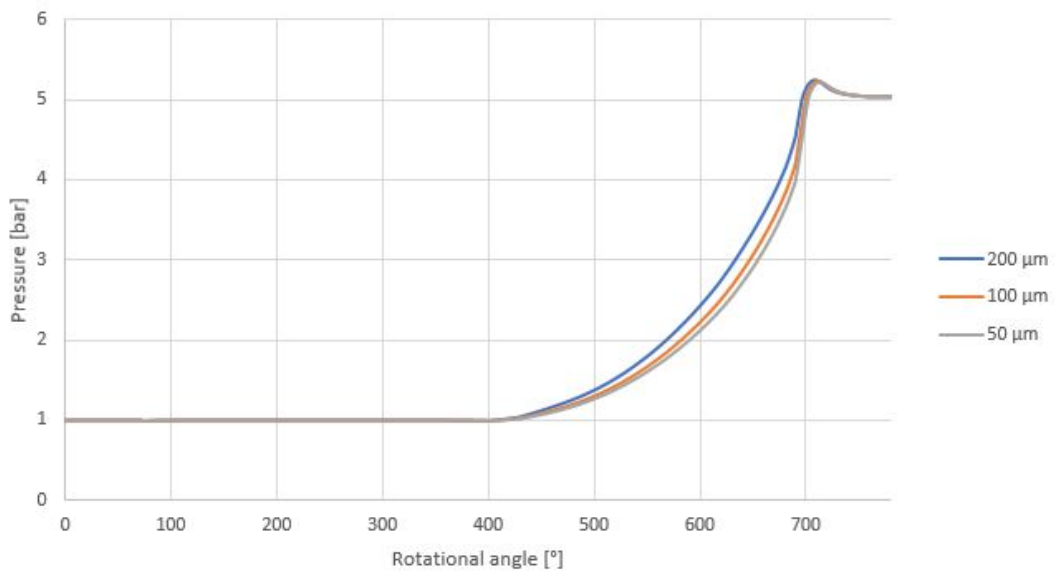


Figure 5.4: Pressure as a function of the male rotational angle for different clearances for the leakage paths. Three clearances were studied, 50, 100 and 200 micrometer. Suction properties and discharge pressure are kept constant for the different clearances.

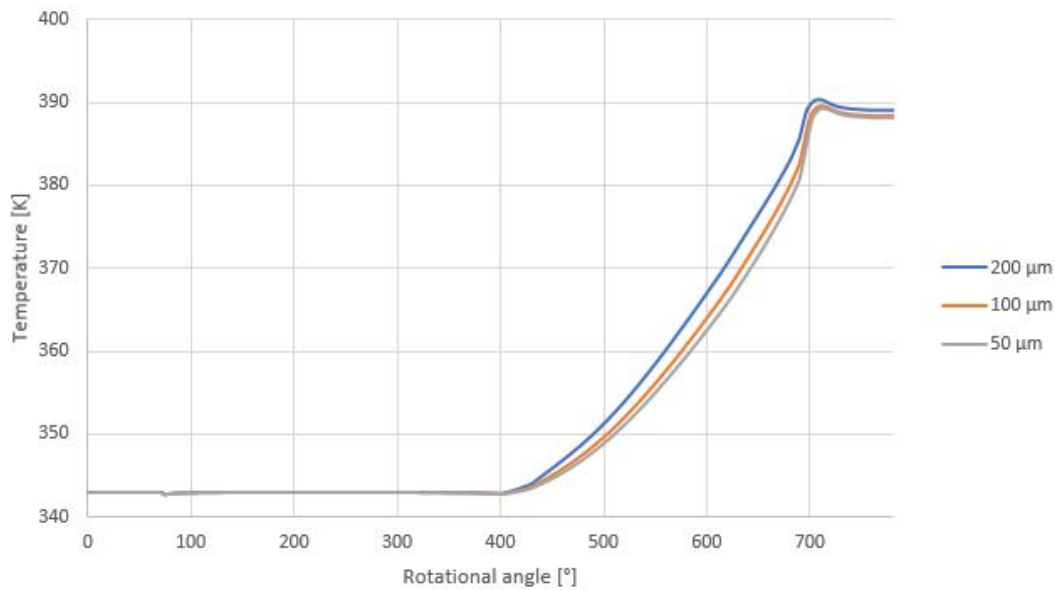


Figure 5.5: Temperature as a function of the male rotational angle for different clearances for the leakage paths. Three clearances were studied, 50, 100 and 200 micrometer. Suction properties and discharge pressure are kept constant for the different clearances.

The most noticeable difference can be seen in Figure 5.6 where the vapor quality decreases less with increased clearances.

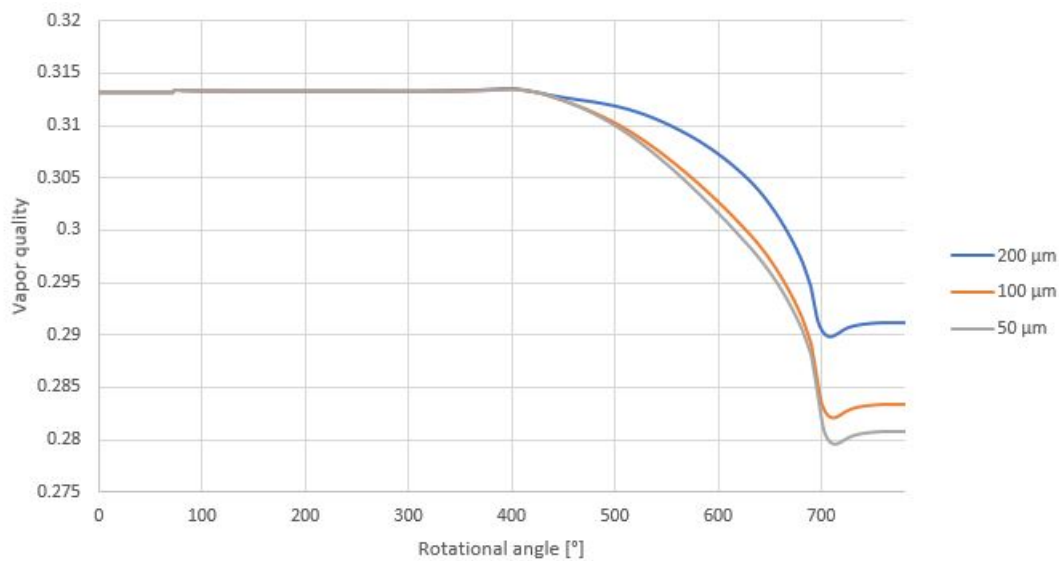


Figure 5.6: Vapor quality as a function of the male rotational angle for different clearances for the leakage paths. Three clearances were studied, 50, 100 and 200 micrometer. Suction properties and discharge pressure are kept constant for the different clearances.

The efficiencies for this can be seen in Table 5.4. It is clear that the efficiency decreases with increased clearances as was expected. From 50 to 200 micrometer the isentropic efficiency decreases almost 10% and the volumetric is steadier but still loses about 2% with the same clearance increase.

Table 5.4: Overview of the isentropic and volumetric efficiency with different clearances. With larger clearances there are more leakages leading to less efficient processes.

Clearance [μm]	50	100	200
$\eta_{is,com}$ [%]	78.05	74.87	69.50
η_{vol} [%]	85.81	85.13	83.81

5.3. EFFECT OF DISCHARGE PRESSURE

Until now the discharge pressure has been kept constant but now the discharge pressure will be changed while all other properties are kept constant to see how that can effect the system. Table 5.5 has an overview of the properties used for the following calculations.

Table 5.5: Properties used for comparing calculations for different discharge pressure with constant inlet properties.

Maximum volume per cavity	0.000058m ³
Discharge opens at	690 °
Stop angle	780 °
Clearances	50 μm
Suction pressure	1 bar
Suction temperature	70°C
Suction vapor quality	31%
Discharge pressure	Varies
Ammonia concentration	30 wt%
Number of cavities	5
Rotational speed	10000

The pressure as a function the male rotational angle is shown in Figure 5.7. As expected with different discharge pressures the value at the discharge varies quite a bit. The initial calculation, with constant suction and discharge phases had the final pressure at these inlet conditions between 3 and 4 bar. As the curves show when the discharge pressure is forced to be lower the pressure decreases quickly as clear for the 2 bar discharge pressure. When the difference is smaller, see the 3 bar, the curve is smoother but still with a larger slope than the other cases.

When the discharge pressure is pushed to be higher the discharge curve is very similar for the pressures over 4 bar. The discharge pressure from the initial run, with discharge and suction assumed constant, is just under 4 bar. The pressure curves show clearly the overcompression, with a quick drop in pressure to reach the discharge pressure. The undercompression is not as obvious but can be seen in the discharge pressures above 4 bar.

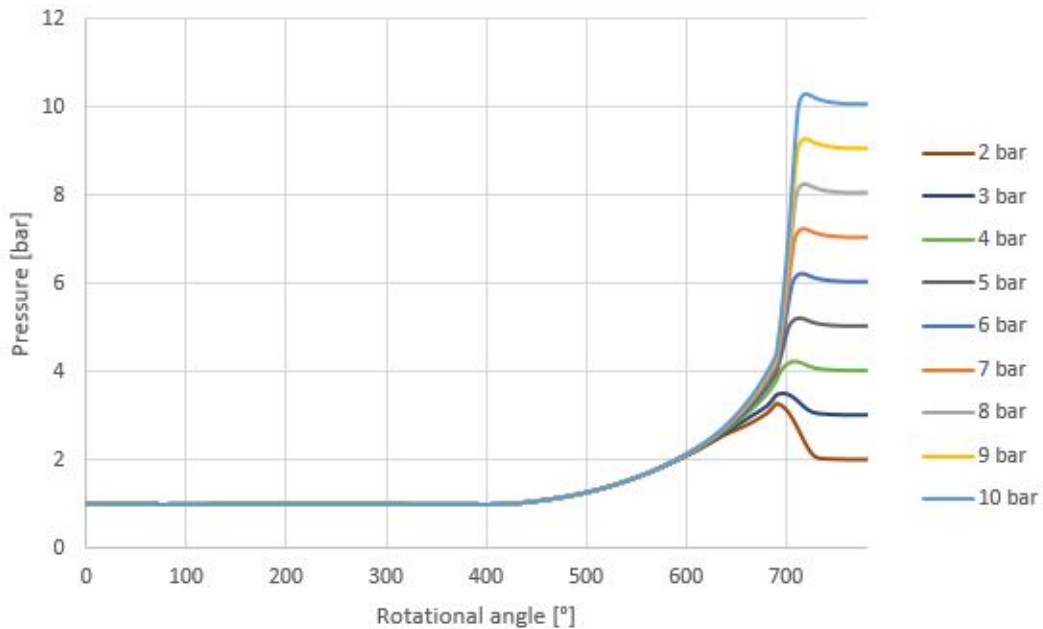


Figure 5.7: Pressure as a function of the male rotational angle with different discharge pressures. The inlet qualities are constant between all cases. The initial case where the discharge phase is not considered reaches pressures between 3 and 4 bars at these inlet conditions. As can be seen when the discharge pressure is below that it decreases quickly while the change is not as noticeable for higher discharge pressures.

The same trend as for the pressure is seen in the temperature distribution, shown in Figure 5.8. With increased discharge pressure the temperature must increase as well as they are connected.

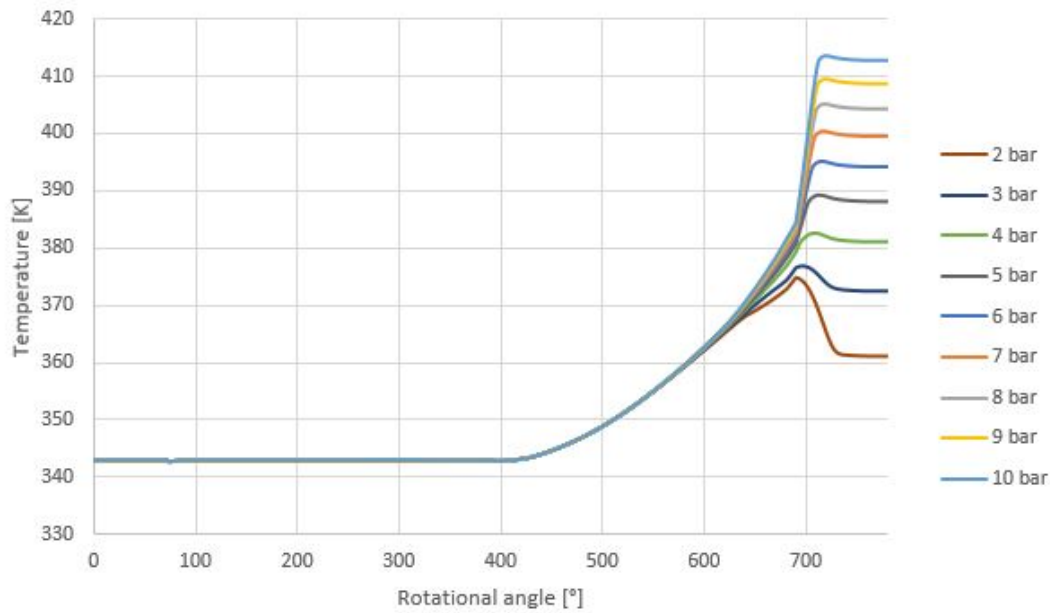


Figure 5.8: Temperature as a function of the male rotational angle with different discharge pressures. The inlet qualities are constant between all cases. The initial case where the discharge phase is not considered reaches pressures between 3 and 4 bars at these inlet conditions. As can be seen when the discharge pressure is below that the temperature decreases quickly while the change is not as noticeable for higher discharge pressures.

The vapor quality is seen in Figure 5.9, there is some difference in the quality with different discharge pressure. With increased discharge pressure the vapor quality decreases more and has a smaller increase when the mass starts to leave the compressor.

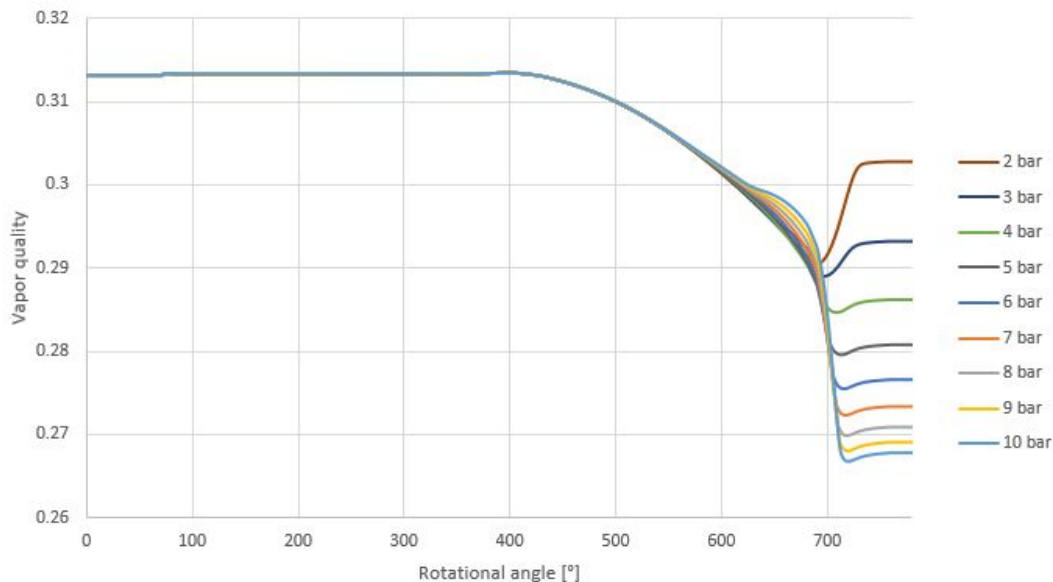


Figure 5.9: Vapor quality as a function of the male rotational angle with different discharge pressures. The inlet qualities are constant between all cases. The initial case where the discharge phase is not considered reaches pressures between 3 and 4 bars at these inlet conditions. As can be seen when the discharge pressure is below that, the vapor quality increases a lot while the mass is discharged while it is significantly less for higher discharge pressures.

To get a better idea of the isentropic and volumetric efficiencies for this large variety of discharge pressures they have been plotted and can be seen in Figure 5.10. While the volumetric efficiency is almost a straight line the isentropic efficiency has more of a curve. The peak is when the discharge pressure is kept at values similar to what the initial calculations calculated, with it decreasing with lower and higher discharge pressure. The decrease is larger when the discharge pressure is lower than the initial value. In the isentropic efficiency the over and undercompression can clearly be seen. While the compressor is subjected to overcompression the decrease in efficiency from the peak is very quick, small changes lead to large efficiency losses. While in undercompression the decrease in efficiency happens much slower, or around 2.5 times slower.

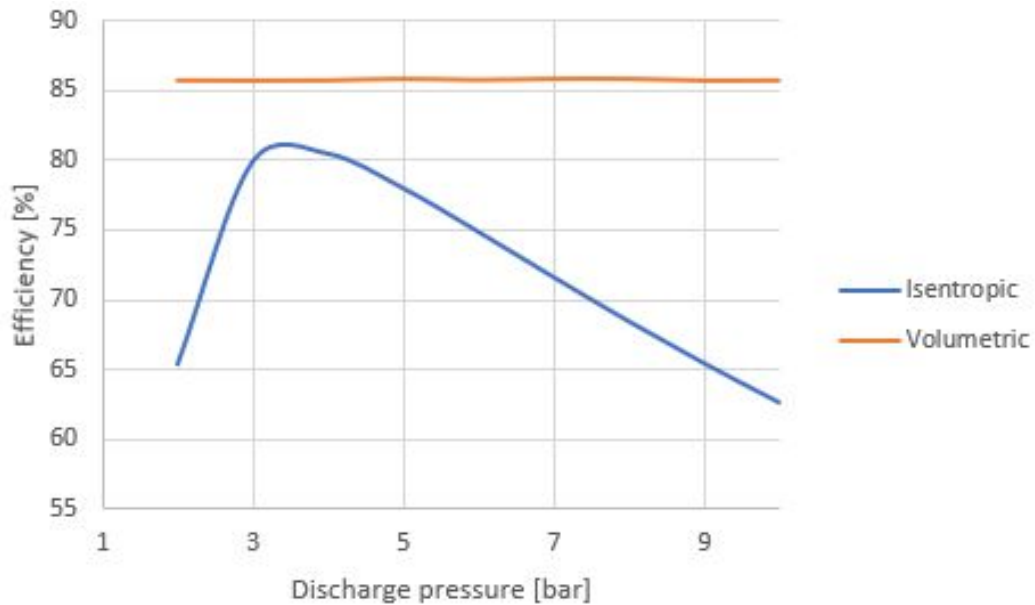


Figure 5.10: Overview of the isentropic and volumetric efficiency at different discharge pressures.

5.4. EFFECT OF VAPOR QUALITY AT SUCTION

After seeing what the effect of changing the discharge pressure had the initial conditions are the next step. In Table 5.6 the properties used for the following calculations are shown.

Table 5.6: Properties used for comparing calculations for different vapor quality at the suction port.

Maximum volume per cavity	0.000058m ³
Discharge opens at	690 °
Stop angle	780 °
Clearances	50 μm
Suction pressure	1 bar
Suction temperature	Varies
Suction vapor quality	Varies
Discharge pressure	5 bar
Ammonia concentration	30 wt%
Number of cavities	5
Rotational speed	10000

In Figure 5.11 the pressure is shown at different suction vapor qualities. With higher vapor qualities the higher pressure is reached during compression and so the discharge of mass seems to start earlier. This is noticeable mostly in the small discharge curve, as it shifts to the left with increased vapor quality. This is because with more vapor quality the higher pressure is reached quicker and thus induces more leakages, also the fact that vapor expands more thus taking more place and pushing back flow through the leakage paths. When the quality has reached superheating the pressure increases very quickly and reaches higher values.

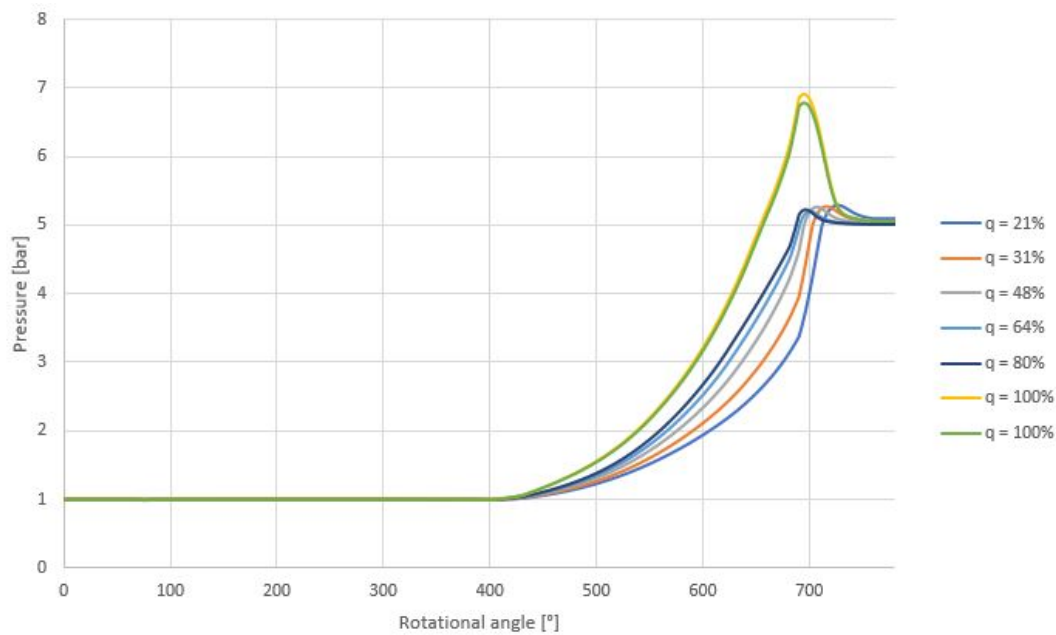


Figure 5.11: Pressure as a function of the male rotational angle for different vapor quality at the suction. All cases use the same discharge pressure. As can be seen the pressure has a steeper curve with higher vapor quality at the suction. When superheating is reached the pressure has a larger spike.

A similar trend is seen in the temperature in Figure 5.12 except slightly less obvious. With increasing vapor quality the temperature rises quicker until it reaches superheating where it increases much quicker.

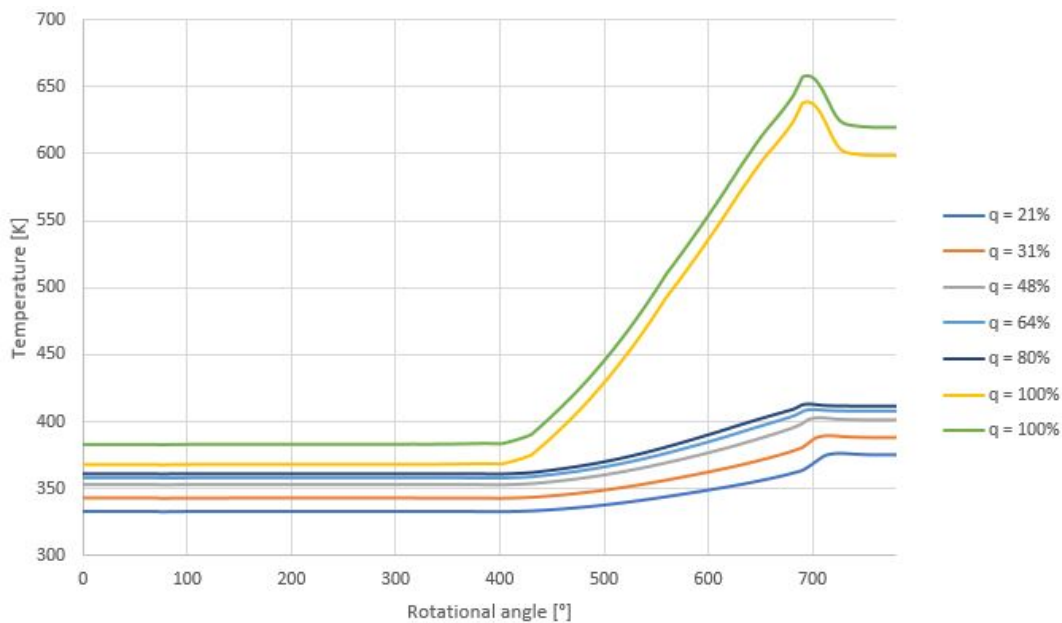


Figure 5.12: Temperature as a function of the male rotational angle for different vapor quality at the suction. All cases use the same discharge pressure. As can be seen the temperature has similar trends between the different qualities. When superheating is reached the temperature rises quickly and reaches much higher values.

In Figure 5.13 the vapor quality is presented. A transition can be seen around the 50% vapor quality, where lower values decrease during compression and higher increase. When there is too much liquid in the mixture the amount of liquid increases during compression, while when the vapor quality is higher than 50% then the vapor increases during compression. This fits with the trend seen in the T-s diagrams for ammonia-water where the vapor quality is inclined upwards after the 50% line and before that has an incline downwards.

leading to lower qualities.

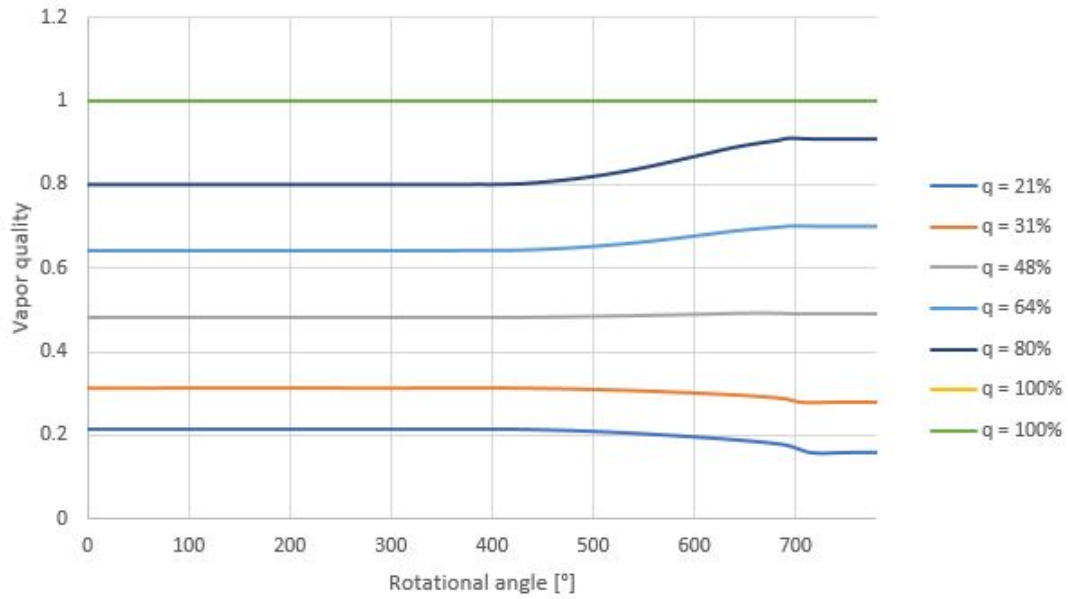


Figure 5.13: Vapor quality as a function of the male rotational angle for different vapor quality at the suction. All cases use the same discharge pressure. For lower suction vapor qualities the quality decreases slightly while when the quality is over 50% the quality rises slightly during compression.

Table 5.7 presents an overview of the efficiency at different vapor qualities at the suction inlet. For the isentropic efficiency a familiar trend can be seen, where increasing the vapor quality of the mixture has a decreasing effect on the efficiency. With the total drop being around 17% from the least amount of vapor to the highest. The only outlier from this trend is the second superheated value, which was slightly higher, then the efficiency increased slightly. Meanwhile the volumetric efficiency stays around the same value with a maximum difference of 0.5%.

Table 5.7: Overview of the isentropic and volumetric efficiency for the different suction vapor qualities. With increased vapor quality at the suction the efficiency decreases, except for a small increase when the mixture is superheated even more.

Suction vapor quality [%]	21	31	48	64	80	100	100
$\eta_{is,com}$ [%]	81.20	78.04	74.82	72.83	71.24	64.20	64.94
η_{vol} [%]	85.61	85.81	85.97	86.04	86.08	86	86

5.5. EFFECT OF ROTATIONAL SPEED

Finally the effect of different rotational speeds was examined. While the compressor used for this study is rather small it can handle very high rotational speeds. With the maximum value around 23000rpm, that however needs higher mass flows than the current system will handle. Table 5.8 presents an overview of the properties used in the following calculations.

Table 5.8: Properties used for comparing calculations under different rotational speeds. After the stop angle the properties are assumed stable. four different rotational speeds are examined, 3000, 5000, 10000 and 15000 rpm while the other properties are kept stable.

Maximum volume per cavity	0.000058m ³
Discharge opens at	690 °
Stop angle	780°
Clearances	50 μm
Suction pressure	1 bar
Suction temperature	80°C
Suction vapor quality	48%
Ammonia concentration	30 wt%
Number of cavities	5
Rotational speed	3000, 5000, 10000, 15000

Figure 5.14 presents the pressure as a function of the male rotational angle. Its is clear that the pressures curve is better with increased rotational speed. When at very low values, such as 3000rpm, the pressure curve is rather unsteady.

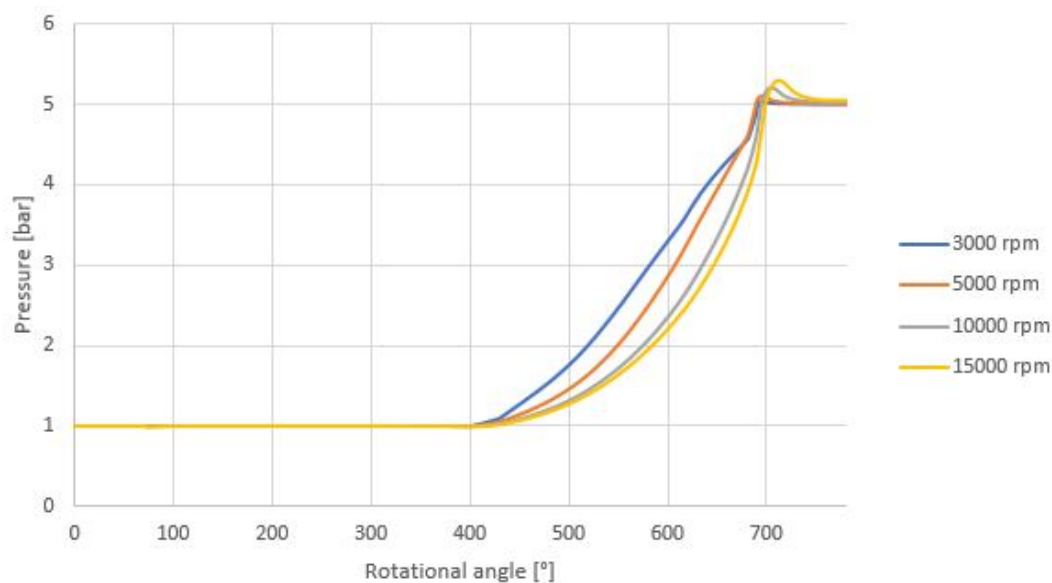


Figure 5.14: Pressure as function of the male rotational angle for different rotational speeds. With constant inlet properties and discharge pressure of 5 bar. At higher rotational speeds there is a smoother discharge process while the lower speeds have a bit more difficulty reaching higher pressures.

The same trend is seen in the temperature plot, presented in Figure 5.15. It is clear from the temperature plot that the lower rotational speed needs higher temperatures to reach the intended discharge pressures. This is because at lower rotational speeds there is more time for leakages to go back in the system and increased leakages lead to higher temperatures as there is more flow going back

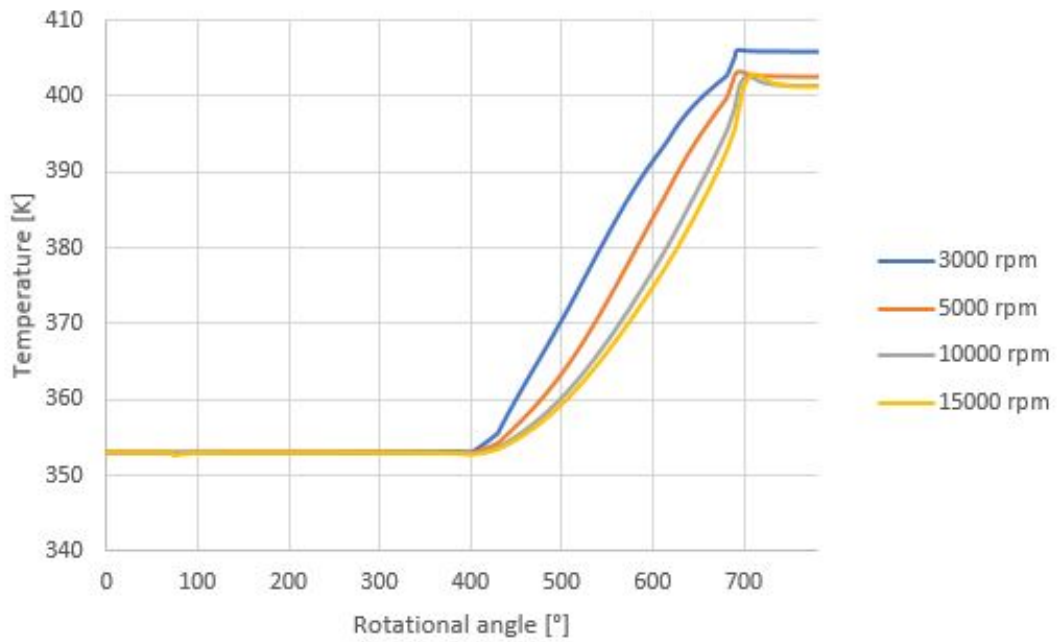


Figure 5.15: Temperature as function of the male rotational angle for different rotational speeds. With constant inlet properties and discharge pressure of 5 bar. At higher rotational speeds there is a smoother discharge process while the lower speeds have a bit more difficulty reaching higher pressures. For lower speeds the temperature also reaches higher values.

A large difference is then seen in the vapor quality, while the higher rotational speeds don't experience a large difference in vapor quality during suction the curves are noticeably bigger for the 5000 and 3000rpm curves. Meaning that with lower rotational speeds more vapor is formed, as expected with the increased leakages.

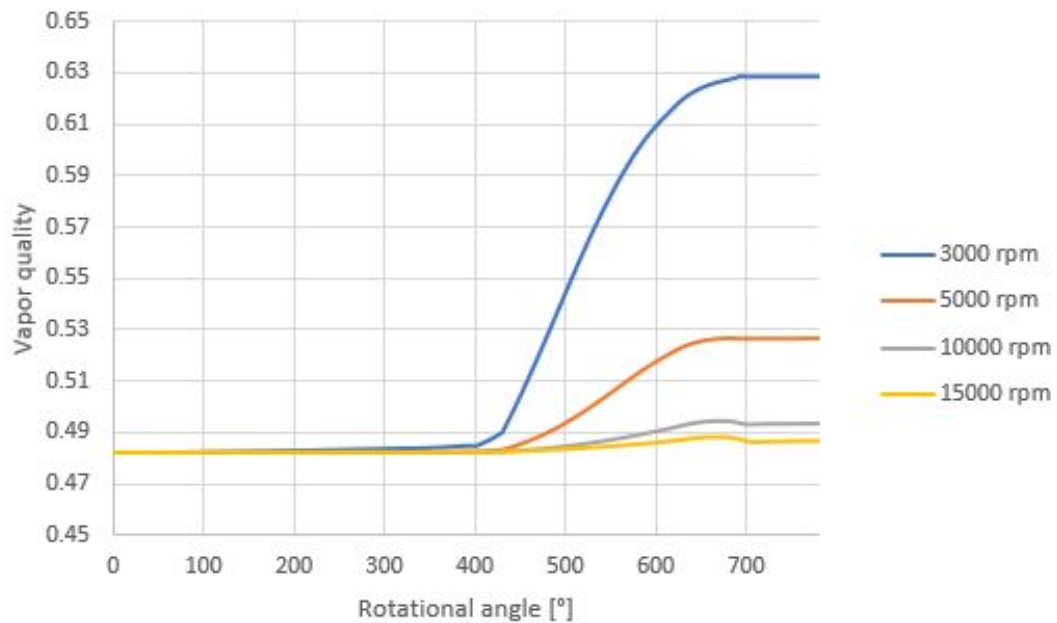


Figure 5.16: Vapor quality as function of the male rotational angle for different rotational speeds. With constant inlet properties and discharge pressure of 5 bar. At lower speeds the vapor quality increases quite a lot

Table 5.9 presents the efficiencies for the different rotational speeds. While overall the volumetric efficiency is in the same range, around 86%, the isentropic efficiency has quite a difference. With increased

rotational speed the isentropic efficiency also increases quite a bit. With the difference from highest to lowest rotational speed being around 18%.

Table 5.9: Overview of the isentropic and volumetric efficiency at different rotational speeds. At higher rotational speeds the leakages are less prominent thus leading to a bit more efficient process.

Rotational speed [<i>rpm</i>]	3000	5000	10000	15000
$\eta_{is,com}$ [%]	61.83	67.64	74.90	77.79
η_{vol} [%]	85.93	86.18	85.97	85.68

6

EXPERIMENTAL SETUP

In this chapter the experimental set-up used to validate the compressor model is introduced. Figure 6.1 shows a simplified version of the setup used in this project.

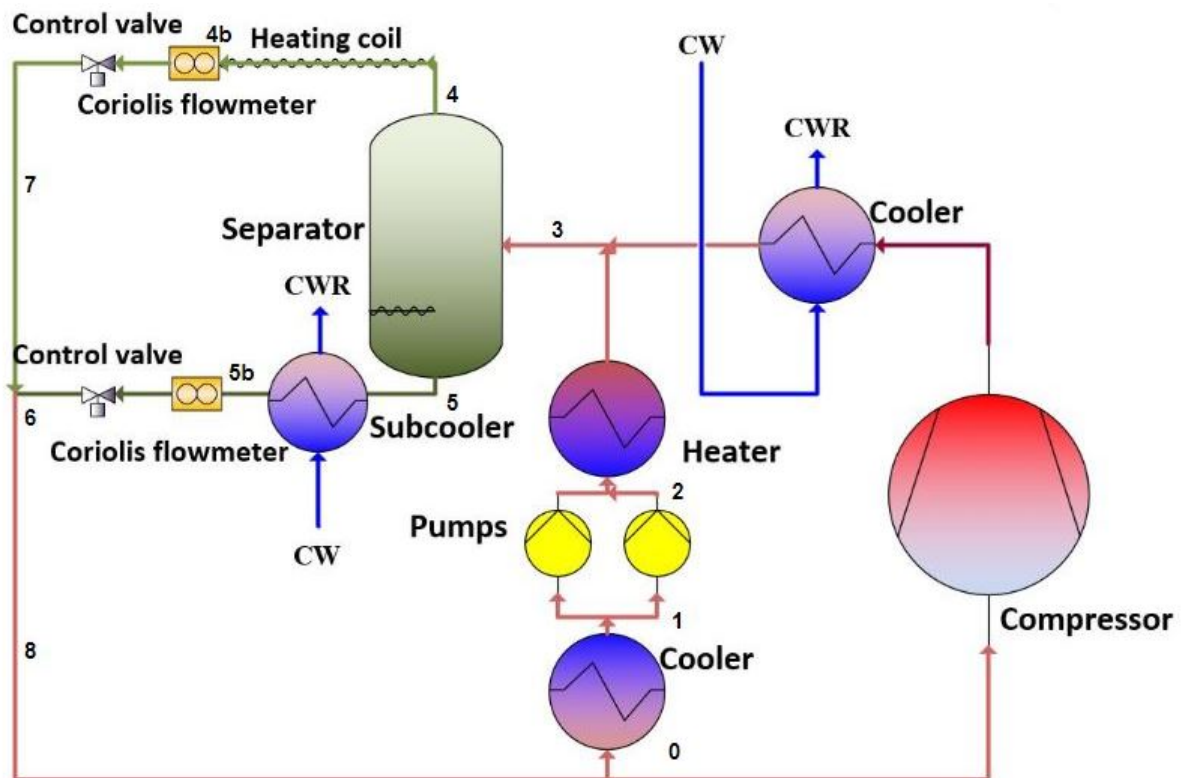


Figure 6.1: Simple representation of the experimental setup. The inlet conditions of the compressor are obtained by making use of a separator. The desired vapor quality is obtained by separately adding the liquid and vapor phases from the separator.

Here both possible versions of the setup are shown, the final version uses a compressor to compress the mixture while the other uses a series of parallel pumps to achieve similar results. For the current study the pumps will be used instead of the compressor as they are readily available and can be used to adapt the cycle for the compressors' requirements.

This setup is used in order to validate which values must be obtained at certain points during the cycle to achieve the desired outcome from the compressor, when it is connected instead of the pumps. These desired values have been determined with the model introduced in Chapter 3.

Currently the compressor line is not connected and the flow goes straight to the first cooler. This cools the flow until it reaches subcooled liquid state so that the pumps can operate it. With the pumps a higher pressure is reached and to obtain the conditions required in the separator the flow is first heated to a higher temperature. With this similar separator inlet conditions should be achieved as with compressor and cooler. The separator splits the flow into vapor and liquid phases which exit through the top and bottom. The vapor leaving through the top passes through a heating coil which allows it to superheat slightly. While the liquid is subcooled in another heat exchanger in order to be certain that the flow is completely in the liquid phase. This is necessary as the liquid flow is sprayed into the gas flow where the two meet, and the spray nozzle cannot handle a two phase flow. This is also true for the control valve and flow meter, additionally the flow meter has a temperature limit.

Now the flow has come to a full circle, here it is important to check the properties, such as temperature, pressure and vapor quality to ensure that the compressor can handle the fluid conditions. This is important to check since the compressor can be ruined if there is more vapor or liquid than it was designed for.

6.1. PREPARING THE EXPERIMENTS

Before the start of any actual experiments, it is good practice to go over everything to confirm that all is working as it should.

First the temperature sensors were calibrated to see if they were all measuring correctly. This was done by using a water bath for temperatures up to 80 degrees and then for the sensors that need to cover a higher range an oil bath was used for temperatures from 80 to 160 degrees. A standalone temperature sensor with accuracy of $\pm 0.01K$, which is not connected to the Lab-View of the setup, is also put into the hot bath with the sensors that are being tested. As the bath may not be at a completely consistent temperature throughout the bath it is important to keep all the sensors at a similar place within it.

The temperature sensors had all been calibrated at the production company as well, therefore, this was only a test to see if real measurements matched with the calibration given by the production company. They did calibrations at three different temperatures 60°C, 120°C and 180°C and the difference should be $\pm 0.06K$.

Table 6.1: Average difference and maximum difference between temperature sensors

Temperature Sensor	Average difference [°C]	Maximum difference [°C]
TI_401	0.0149	0.0756
TI_403	0.1533	0.3049
TI_405	0.0727	0.1468
TI_406	0.0306	0.0983
TI_407	0.1116	0.2076
TI_701	0.0583	0.1468
TI_702	0.1043	0.1905
TI_720	0.0189	0.0451
TI_721	0.0190	0.039
Maximum	0.15	0.30
Average	0.06	0.12

After calibration the accuracy of the sensors can be expected to be $\pm 0.06 K$, which has been proved by calibration by the production company and validated by tests in the setup as explained here.

Next step was to check if all the pressure sensors were comparable, that is if they all show similar values. First the system was filled with nitrogen gas until it reached 11 bar, then that pressure was held and logged for a few minutes to see how much pressure was lost. This was done at an one bar interval until atmospheric pressure was reached. In the system there are four pressure sensors, with the system closed, filled with nitrogen and the pumps not active all the sensors should have shown close to the same value. With this it was possible to estimate how the sensors compare to each other to see how accurate they are.

In Table 6.2 the average difference between the sensors is presented. Overall they are rather comparable to each other and thus should be considered reliable for the experiments.

Table 6.2: Average difference of each pressure sensor compared to the other sensors and if they are considered to be comparable to each other.

Pressure Sensor	Type of sensor	Average difference [bar]	Comparable to other sensors
PI_202	SITRANS P DS III / P410	<0.06	Yes
PI_401	SITRANS P DS III / P410	<0.05	Yes
PI_402	SITRANS P DS III / P410	<0.05	Yes
PI_403	SITRANS P DS III / P410	<0.06	Yes

At the same time it was possible to see if there were any leakages in the closed system. This has to be done for two main reasons, firstly ammonia is a poisonous gas so leakages can be dangerous and also leakages could alter the pressure within the system during experiments. This was done with some pressure testing and making use of raw data available from the lab-view.

After this test it was clear that overall the system was fairly leak tight but still with some leakages, of a few millibar every 10-20 seconds at high pressures and every few minutes at lower pressures. As this was not enough to find the location of leakages the next step was to pressure test using water. The system was filled with water, up to around 4 bar pressure and left to settle for 2 whole days. During this time, due to temperature changes, the pressure rose to almost 11 bar, which did make finding leakages easier. After the pressure had been logged for two days, the whole system could be checked for any droplets that could point towards leakages.

Two small leakages were found in the system, which should account for the small amount of leakages measured with nitrogen. These connections were tightened before the actual experiments. Later the system was left over a weekend, this time at 20 bar. At this point there were hardly any leakages, the pressure drop was well within 0.1 bar per hour. Therefore, the setup should be considered leak proof at pressures at and under 20 bar, with the highest operating pressure at around 14 bar the setup should not be affected by leakages.

There are some heating elements in this setup, the most convenient way to test if they are working is to turn them on and see if the correct components start heating up. A similar approach is used for the level and flow sensors. There are level sensors in the separator, to measure the liquid level. Also in the tank where the ammonia water mixture is released there is a minimum and maximum amount of liquid that must be in the tank at all time. This is done with two level sensors where one sounds an alarm when the level is below it and the other when the level is above the sensor. These sensors were tested by filling the tank with water and seeing if the alarms went on and off at correct times.

6.2. MATLAB PREDICTION CYCLE

To get a rough idea which values give which results the cycle explained here is set up in a Matlab [13] script. By calculating state points at various points during the cycle, a loop can be formed that uses previous points to calculate the next.

Figure 6.2 shows an overview of the points being examined.

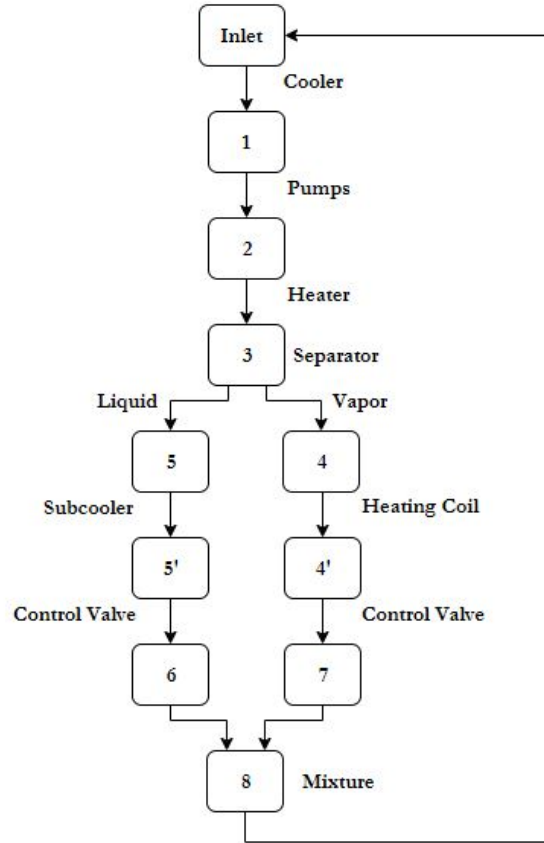


Figure 6.2: Overview of state points calculated in Matlab. Each point corresponds to respective point in the cycle shown in Figure 6.1. When all points have been calculated point 8 becomes the inlet of the compressor or cooler for pumps.

Between the start and point 1 the flow goes through the cooler. Here the pressure is stable and the temperature is lowered until the flow is subcooled liquid. The heat required for this step is found with Equation 6.1

$$\dot{Q}_{cooler} = \dot{m}(h_0 - h_1) \quad (6.1)$$

Between points 1 and 2 the pressure is induced to a higher level with the pumps that keep a certain Δp between these two points. To find the properties after this pressure change the isentropic enthalpy and efficiency of the pumps are used. Equation 6.2 can be rearranged to find h_2 which is the enthalpy after the pumps and where $h_{is} = f(p_2, s_1)$. Here the entropy from point 1 is used to find the isentropic value. This method does require that the pressure after the pumps is known, or assumed to start with.

$$\eta_p = \frac{h_{2,is} - h_1}{h_2 - h_1} \quad (6.2)$$

With the enthalpy and pressure known after the pumps the other properties can be found. With Equation 6.3 the pumping power can be found.

$$\dot{W} = \dot{m}(h_2 - h_1) \quad (6.3)$$

From 2 to 3 there is another heat exchanger, this time intended to heat the mixture. This uses the same principals as the cooler explained before, except now it adds heat.

When the mixture goes through the separator it is divided into two sections. So the first step is to find the concentration of the vapor and liquid phases in the mixture, this can be done with Refprop [11]. This gives the concentrations of the two new streams out of the separator, which are used in calculations for the next points.

Next the properties of the new flows are found. The pressure and temperature remain the same during separation and with the concentration of the new flows the other properties, such as enthalpy and density, can be found using Refprop.

With the properties of all sides known it is possible to do mass and enthalpy balances to find how the flow was divided. These balances can be seen in Equations 6.4 and 6.5. The enthalpy is known for all phases, by solving for q in Equation 6.5, it can be put into Equation 6.4 to find the amount of mass that goes into each phase.

$$\dot{m} = \dot{m}_G + \dot{m}_L = q\dot{m} + (1 - q)\dot{m} \quad (6.4)$$

$$\dot{m}h_3 = q\dot{m}h_4 + (1 - q)\dot{m}h_5 \quad (6.5)$$

The subcooler between points 5 and 5b is used to cool the liquid phase flow from the separator. This flow is subcooled so it is definitely in complete liquid phase, this has to be done for the spray nozzle, control valve and flow meter. This is done with another heat exchanger working the same way as the other cooler.

The heating coil receives the gas phase from the separator, this is only a heating element so the pressure stays the same.

Both streams go through control valves that can influence the flow through them, influencing a pressure drop to the original value before the pumps increased the pressure. Next they are combined, with the liquid sprayed over the gas phase. When they combine another mass and enthalpy balance is required to find the enthalpy of the new mixture as is shown in Equation 6.6

$$h_8 = \frac{\dot{m}_G h_7 + \dot{m}_L h_6}{\dot{m}} \quad (6.6)$$

And finally to ensure that the vapor quality is high enough for the compressor the vapor quality is calculated from the properties found in point 8. This can be found with either Refprop[11] or the model of [Rattner and Garimella](#) [17].

6.3. CYCLE PREDICTIONS

By using the Matlab script introduced in the previous section some predictions can be made about how the cycle could behave under different conditions. These predictions can be used to estimate the inlet conditions for the compressors, as they need to be within certain vapor quality limits.

For these predictions only the process around to the separator will be examined, the pumps and heat exchangers around them will be ignored. With this the inlet condition of the separator, which will later be the compressor outlet after some cooling, will be varied. Along with the amount of superheating and subcooling, the effect of these variables on the properties at the compressor inlet will be examined.

First the effect of ammonia concentration is explored. In Table 6.3 the properties used for comparing the different concentrations are presented. For all three ammonia concentrations checked the inlet to the separator, point 3, has the same vapor quality and pressure so the temperature is the only variable varying. To be certain that the mixture is superheated and subcooled respectively those values are kept slightly higher than is the minimum and constant between the different concentrations.

Table 6.3: Overview of the properties used for comparing calculations for different ammonia concentration.

q_3 [%]	63
p_3 [bar]	8
p_8 [bar]	1
Subcooling [K]	72
Superheating [K]	10
Ammonia concentration [wt%]	20, 30, 40

Figure 6.3 presents the vapor quality after the vapor and liquid mixtures have been mixed, point 8. This will also be the inlet of the compressor. While the vapor quality does decrease with increased ammonia concentration the difference is barely noticeable. With the total difference from highest to lowest being lower than 0.5%.

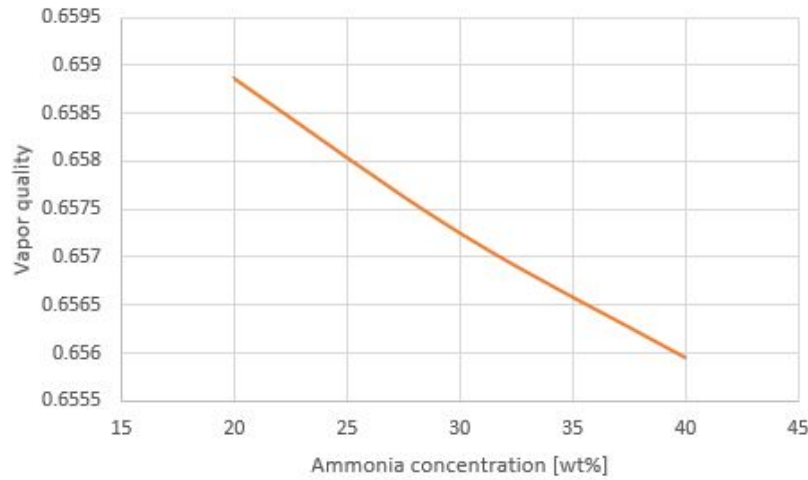


Figure 6.3: Vapor quality at the end of the process as a function of the ammonia concentration. The resulting vapor quality is almost the same between the different concentrations. There is however a small decrease noticeable with increased ammonia concentration.

Next the temperature into the separator is varied, this results in varying vapor quality in point 3 as well. Table 6.3 shows an overview of the properties used in the calculations.

Table 6.4: Overview of the properties used for comparing the vapor quality at the beginning and end for different inlet temperatures.

q_3 [%]	Varies
p_3 [bar]	8
p_8 [bar]	1
Subcooling [K]	72
Superheating [K]	10
Ammonia concentration [wt%]	40

In Figure 6.4 the vapor qualities in points 3 and 8 are presented as functions of different inlet temperature. It is clear that the vapor quality does not change a lot after going through the separation process, there is a small difference in vapor quality after mixing and at the inlet of the separator.

When the vapor quality of the mixture going in to the separator is less than 30% then the quality decreases slightly after mixing. While if the vapor quality is higher when it enters the separator the vapor quality after mixing is slightly higher. This is understandable as when the vapor quality is very low when it enters the separator, the mixture is mostly liquid so not a lot of vapor exits the separator and much more liquid is subcooled, thus resulting in lower temperature in the end as it does not mix with as much superheated vapor.

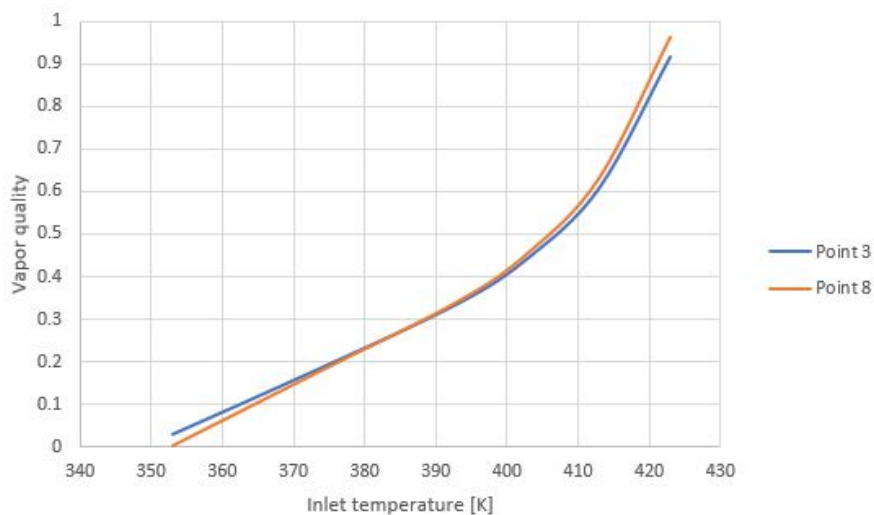


Figure 6.4: Vapor quality as a function of the inlet temperature, point 3. The vapor quality is examined for both point 3 the inlet and point 8 where the two streams have mixed.

Next the effect of the degree of superheating in the vapor line on the quality after mixing is examined. The properties used for the comparison are listed in Table 6.5.

Table 6.5: Overview of the properties used for comparing the effect of superheating. To see the maximum effect, minimum subcooling is used

q_3 [%]	25.3
p_3 [bar]	8
T_3 [°C]	110
p_8 [bar]	1
Subcooling [K]	65
Superheating [K]	Varies
Ammonia concentration [wt%]	40

The changing variables can be seen in Table 6.6. For the properties used in the calculations a minimum superheating of 2 degrees was necessary. Two higher values were examined as well, all using the same value of subcooling of 65 degrees, which was the minimum for this mixture. It is clear that increasing the temperature after reaching superheated values does not have a large increase on the mixed stream, neither on temperature or vapor quality.

Table 6.6: Overview how the mixture is affected if the vapor is superheated at different values. For the properties in Table 6.5 there was a minimum of 2 degree heating in order for the mixture to reach superheating

Superheating [K]	T_8 [K]	q_8 [%]
2	320.05	26.03
10	320.32	26.22
15	320.48	26.34
25	320.81	26.57

A similar test was done for the subcooling effectiveness, the properties used are presented in Table 6.7. As was done before the minimum value of superheating is used for both versions to see the effect unaffected.

Table 6.7: Overview of the properties used for comparing the effect of subcooling. To see the maximum effect minimum superheating is used

q_3 [%]	44.5
p_3 [bar]	8
T_3 [°C]	130
p_8 [bar]	1
Subcooling [K]	Varies
Superheating [K]	1
Ammonia concentration [wt%]	40

In Table 6.8 the subcooling and the temperature and vapor quality of the mixture are presented. The effect is slightly more noticeable here, with roughly 2% decrease in the mixture quality when the subcooling is increased from the minimum, also a almost 2 degree drop in the temperature of the mixture.

Table 6.8: Overview how the mixture is affected if the liquid portion is subcooled at different values. For the properties in Table 6.7 there was a minimum of 68 degree cooling in order for the mixture to be subcooled. Point 8 is after the liquid has mixed with the vapor. There is a noticeable effect, around 2% decrease in vapor quality when excessive subcooling is used.

Subcooling [K]	T_8 [K]	q_8 [%]
68	341.76	46.10
90	340.09	43.92

7

DISCUSSION

In the following chapter the model results and how they might effect the rest of the heat pump cycle will be discussed.

7.1. PERFORMANCE OF COMPRESSOR

A reoccurring conclusion is that the isentropic efficiency decreases with increased suction vapor quality. This is constant between the three different ammonia concentrations that were explored. For each ammonia concentration the results were very similar at the same suction vapor quality with increased quality resulting in higher pressure and temperature at the cost of the efficiency.

To see what effect these properties might have on the entire heat pump cycle, the Coefficient Of Performance (COP) has been examined for the 30 wt% ammonia mixture. To calculate the COP Equation 7.1 has been used, where point 1 is before the compressor, point 2 is after the compressor and point 3 is after the condenser at saturated liquid conditions (see Figure 7.1).

$$COP = \frac{h_2 - h_3}{h_2 - h_1} \quad (7.1)$$

Figure 7.1 presents a typical schematic diagram of the compression resorption heat pump cycle that is part of this study. To give an example of how the heat pump cycle might be a closer look is taken around the maximum COP shown in Figure 7.2. There the temperatures are as follows, $T_1 = 80 \text{ }^\circ\text{C}$, $T_2 = 128.4 \text{ }^\circ\text{C}$, $T_3 = 79.8 \text{ }^\circ\text{C}$ and $T_4 = 43 \text{ }^\circ\text{C}$. In the resorber the temperature decreases around 48 degrees while the desorber would add 37 degrees to the mixture. Theses values of course vary for the different operating conditions this only gives an idea of the temperature range.

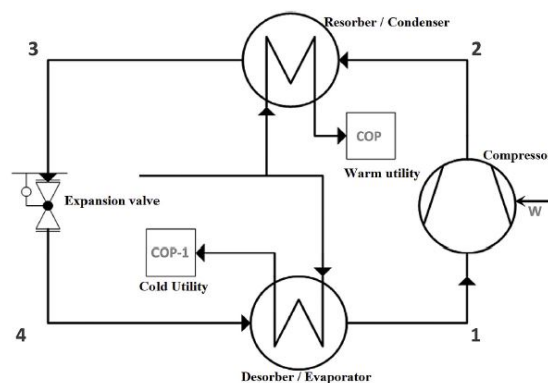


Figure 7.1: A schematic of a Compression-Resorption Heat Pump [7]. This diagram is referenced for the coefficient of performance calculations. Point 3 is assumed to be at saturated liquid conditions.

Figure 7.2 shows the COP for different ammonia concentrations at fixed discharge pressure of 5 bar and vapor quality of 48% at the inlet. It increases rather steadily until it reaches a maximum around 35% ammonia where it starts decreasing again.

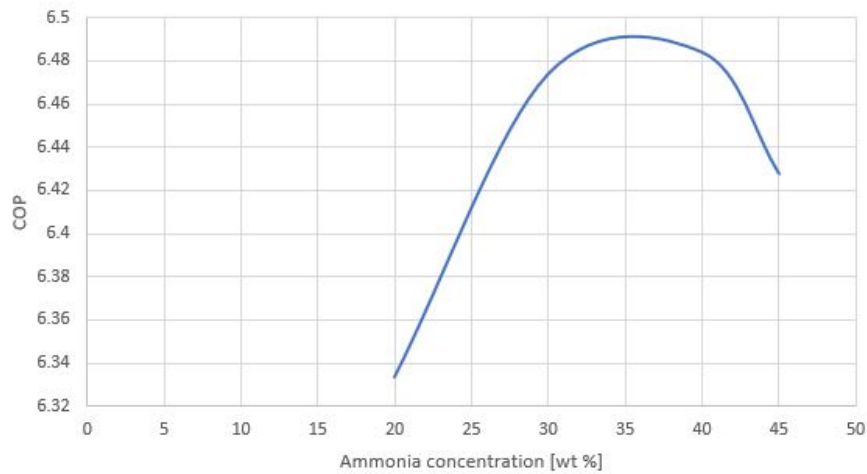


Figure 7.2: Coefficient of performance for different ammonia concentration in the mixture. For a discharge pressure of 5 bar the COP increases up until around 35% ammonia concentration and from that point it starts decreasing again.

Figure 7.3 presents the temperature lift in the compressor for different ammonia concentrations. The curve is rather linear, with the lower ammonia concentrations needing higher temperatures to reach the same discharge pressure.

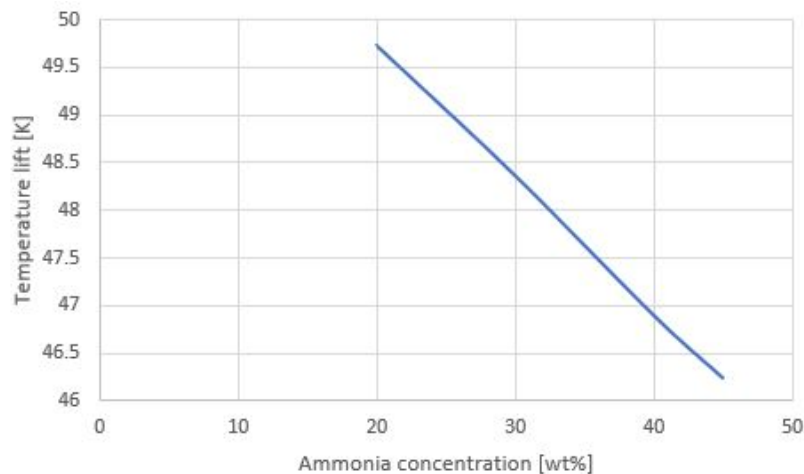


Figure 7.3: Temperature lift in compressor for different ammonia concentrations. As expected the lower ammonia concentrations need higher temperatures to reach the same pressure.

To compare, Figure 7.4 represents the COP when the temperature lift is kept constant and the ammonia concentration varied. This results in a small difference in discharge pressure as well. The curve however is very similar to the curve shown in Figure 7.2. The only difference is that the peak has shifted slightly and is closer to 33wt% ammonia concentration now.

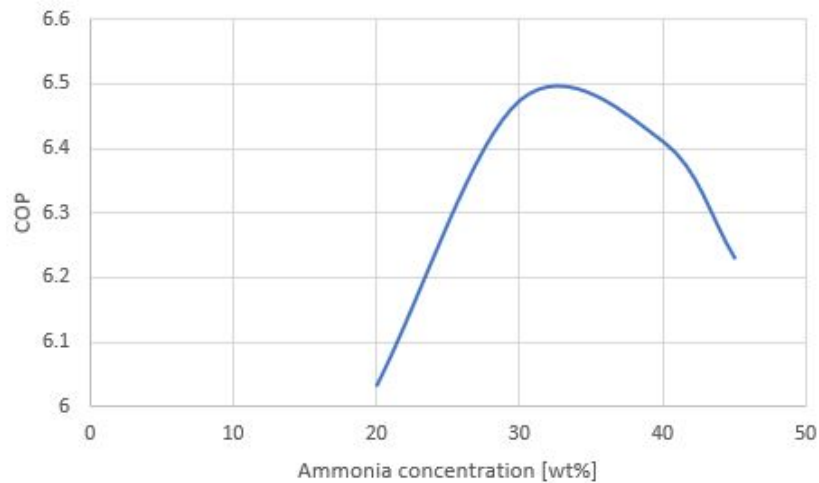


Figure 7.4: Coefficient of performance for different ammonia concentrations, where the temperature lift is kept constant. The curve turns out to be very similar as when the temperature lift varied slightly between ammonia concentrations. With a parabolic shape the maximum is slightly lower even, closer to 30wt% ammonia concentrations

The efficiencies for the stable temperature lift can be seen in Figure 7.5. The same trend as before is seen, where higher ammonia concentrations result in lower isentropic efficiencies.

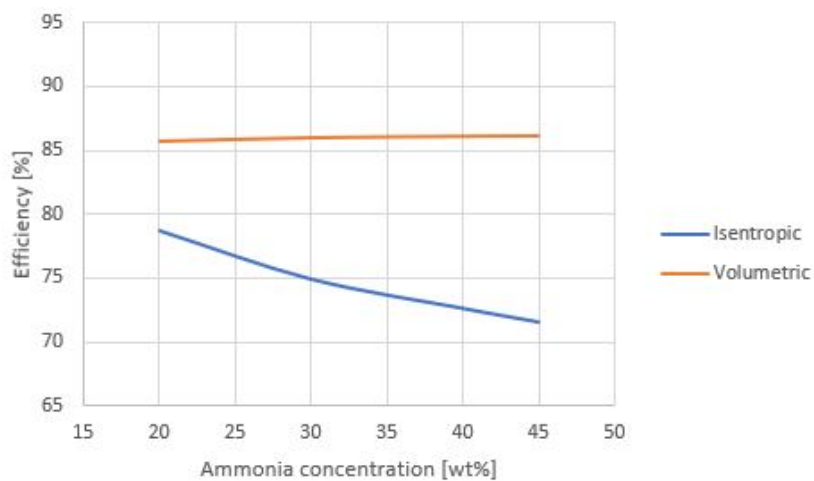


Figure 7.5: The isentropic and volumetric efficiencies when the temperature lift is constant. The same trend can be seen here that higher ammonia concentrations result in lower isentropic efficiencies while the volumetric efficiency is rather stable for different concentrations.

Figure 7.6 presents the COP as a function of different leakage path clearances. As expected higher clearances, lead to lower efficiencies leading to higher final temperatures and lower COP compared to the lower clearance cases. The decrease is practically linear with increased clearances.

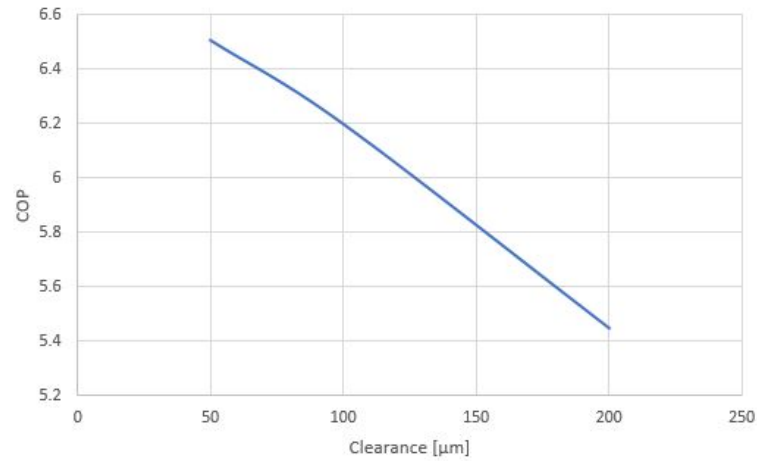


Figure 7.6: Coefficient of performance for different clearances in the leakage paths. As can be expected the COP decreases steadily with increased clearances, around 1 with a fourfold increase in clearance.

Figure 7.7 presents the temperature lift changes with different clearances. While the difference is not very large, around one degree, it does increase with increased clearances.

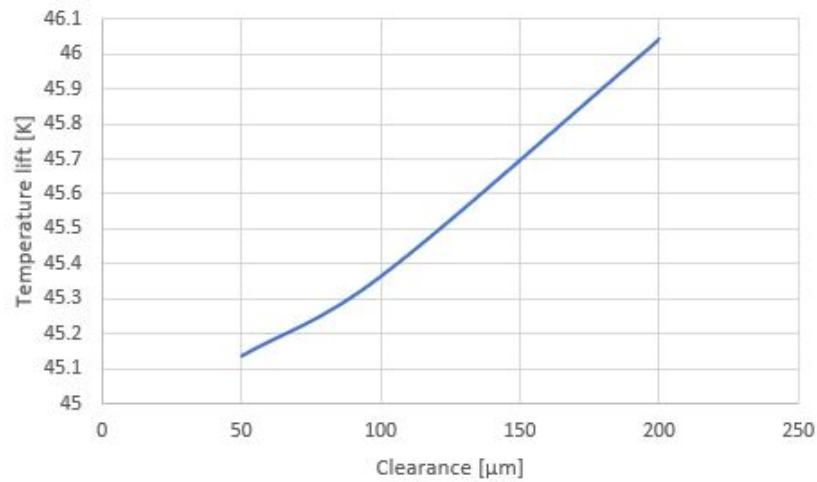


Figure 7.7: Temperature lift in the compressor for different clearances in the leakage paths. With a fourfold increase in clearance the temperature only rises one degree.

Next the difference in discharge pressure was examined, as presented in Figure 7.8. Here a steady decrease in COP is observed, with a larger slope at lower discharge pressures which then starts to level out slightly with higher pressures. While the COP is very high for the lowest discharge pressure values, that does not tell the full story as for these pressures the temperature glide is very small and the efficiency has started to decrease as well.

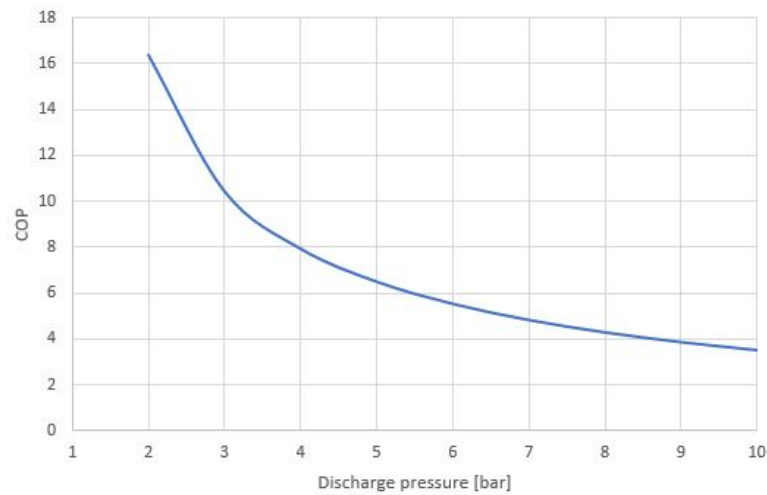


Figure 7.8: Coefficient of performance for different discharge pressures, with constant suction pressure. With higher pressure ratios the COP decreases steadily. However at the lowest pressure ratios the temperature lift is very small so the results could be a bit skewed.

Figure 7.9 presents the temperature lift at different discharge pressures. The temperature increases with higher pressures, until between 5 and 6 bar the increase is quicker than for higher discharge pressures.

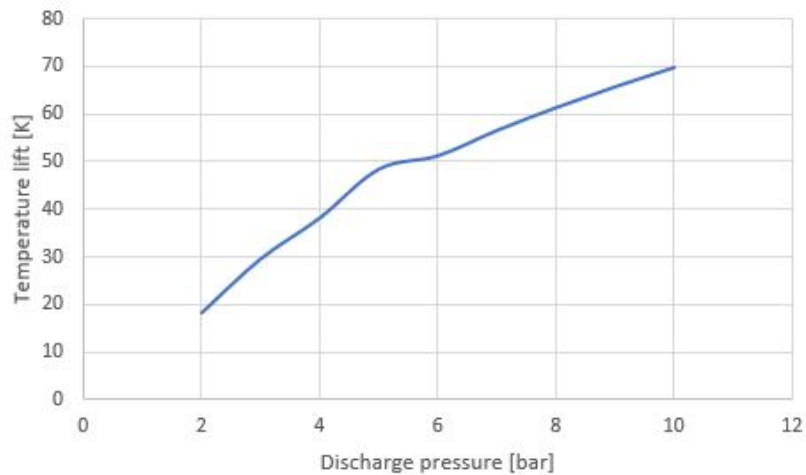


Figure 7.9: Temperature lift in the compressor for different discharge pressures. As expected the temperature increases with higher pressures and so the lift increases. For the lower discharge pressures the rise is slightly more than for higher discharge pressures.

When observing the COP for different suction vapor qualities, in Figure 7.10, there is a maximum around 40% for a discharge pressure of 5 bar and 30 wt% ammonia concentration. For lower suction qualities the COP decreases rapidly. While if the suction vapor quality is increased the COP increases but at a slightly slower pace.

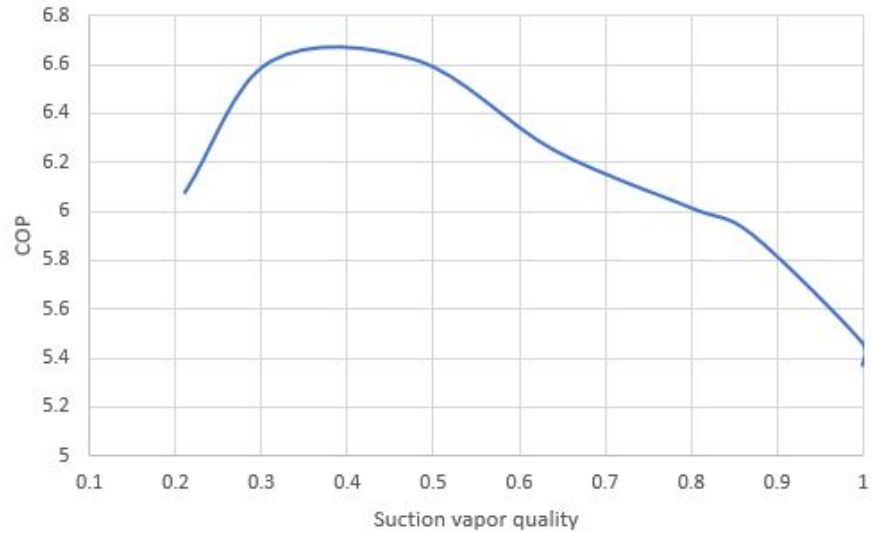


Figure 7.10: Coefficient of performance for different vapor quality at the suction. The best results seem to be achieved around 40% quality, with the curve decreasing on either side.

Figure 7.11 presents the temperature lift for the different vapor qualities. The temperature increases slightly with the vapor quality until it reaches superheating when it spikes up.

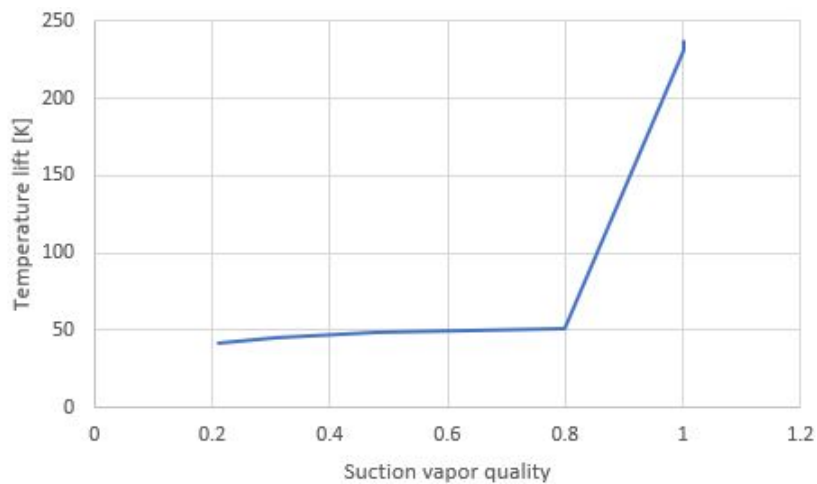


Figure 7.11: Temperature lift under different suction vapor qualities. The temperature increases slowly until it reaches superheated values, there the temperature spikes up.

Now to compare how the curve is effected when the temperature lift is constant, to achieve this the discharge pressure is varied slightly. Figure 7.12 presents the result of different suction vapor quality with the same temperature lift. When the mixture reaches superheated values the temperature spikes, thus the temperature lift will not be similar without large pressure changes and is left out for this calculation.

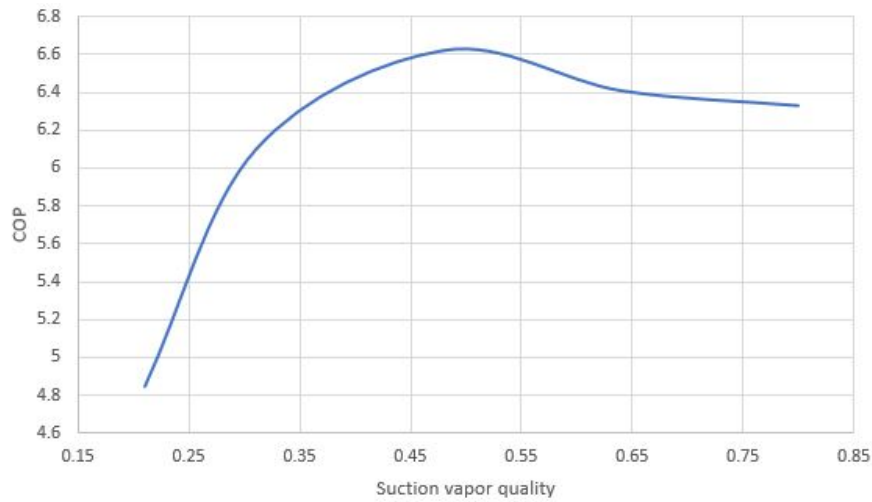


Figure 7.12: Coefficient of performance for different vapor qualities at the suction, with the discharge pressure varying slightly to maintain the same temperature lift

It is clear that the curve has shifted slightly to the right and the peak COP moved from 40 to 50%. Both reach around the same maximum COP of roughly 6.6, however, keeping the temperature lift around the same value higher suction quality gives the optimum performance.

Finally the rotational speed was examined, and the coefficient of performance for the different speeds are shown in Figure 7.13. A rather linear curve is seen, with the COP increasing with increased rotational speed of the compressor. This fits with the efficiency as well which increased with the speed.

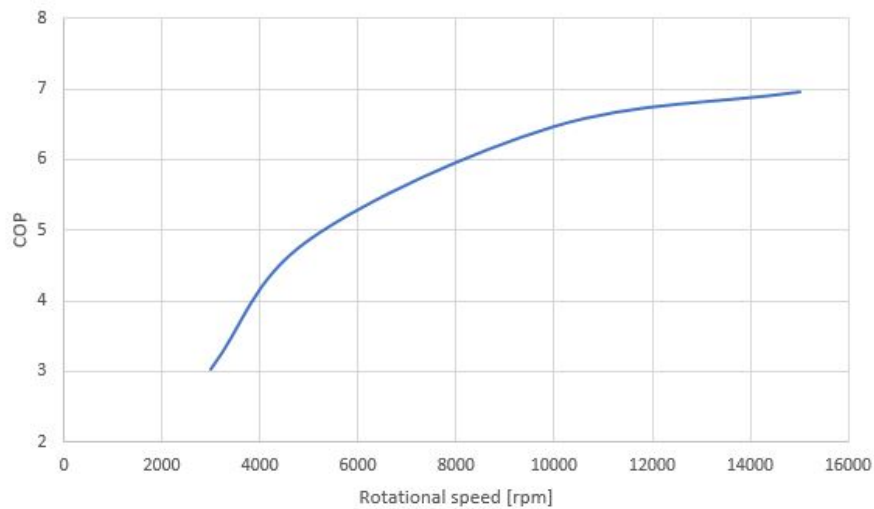


Figure 7.13: Coefficient of performance for the different rotational speeds examined. As expected it rises with increased speeds as the process becomes more efficient.

The temperature lift in Figure 7.14 is similar as to what was expected. Higher lift for the lower speeds as the temperature rises more there to reach the same pressure. The lift becomes smaller as the speed is increased until it starts to stabilize at higher rotational speeds.

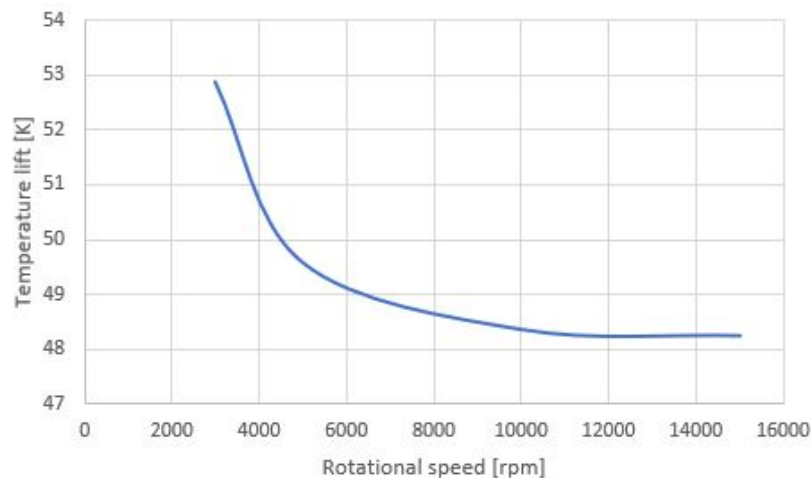


Figure 7.14: The temperature lift for different rotational speeds. The lower the rotational speed the higher temperatures are needed. Then the temperature lift stabilizes at higher rotational speeds.

7.2. MODEL DISCUSSION

Now that the model results have been presented and examined for various cases the next step is to compare which properties are optimal.

With lower concentrations of ammonia there was a slightly higher efficiency, with slightly higher temperature needs. However, the COP as seen in Figure 7.2 has a curve with the peak around 35 wt%.

The clearances are beyond control as they depend on the manufacturing of the compressor. They do still have quite an effect on how efficient the system is. If the leakages are much higher than expected it will be difficult to reach the aspired limit of around $\eta_{is} = 70\%$ including mechanical losses.

While the compressor is built for two phase flow it cannot handle excessive amount of liquid. An estimated value is maximum 15 l/s of liquid. With an ammonia-water mixture the density quickly decreases when it reaches the two phase region. For example a 20wt% ammonia mixture at 10% vapor quality, which is lower than this study should go, has density around 6 kg/m^3 and the maximum mass flow in the compressor is $400 \text{ m}^3/\text{h}$. Using these values to convert the maximum liters per second estimated in the compressor, would give around 0.7 l/s which is much lower than the liquid limit so should not be a problem.

Previously, the effect of suction vapor quality was explored. There a clear trend showed that when the quality at suction was lower than around 50% the vapor quality tended to decrease slightly during compression while at higher qualities it rose slightly. Therefore, this should be kept in mind if the vapor quality cannot drop beneath a certain value to keep it higher than 50% at the inlet.

However, the COP had a peak with around 40-50% vapor quality at the suction so if possible that should be the attempted value to get the highest efficiency.

This connects also to the rotational speed. With higher rotational speeds both the efficiency and COP increased. Higher rotational speeds result in increased mass flow which can be a limiting factor. Additionally, while the mechanical losses are assumed constant in this study, at 90%, it has been shown that with increased rotational speed the mechanical losses increase as well. So while the efficiency and COP increase with higher rotational speed, the increase stabilizes as the speed gets higher. Thus smaller increases in values and then

there are more losses so too high rotational speeds are not ideal.

When looking into the rest of the heat pump cycle the properties don't differ from the inlet of the separator and after the vapor and liquid streams have been mixed. Except there is a small increase in vapor quality, when the inlet quality is higher than 30%. With this trend it can be assumed that if the mixture at the compressor outlet is cooled down to just below the proposed vapor quality needed at the inlet of the compressor, that the small increase in vapor after mixing will help obtain the expected value at the inlet.

8

CONCLUSIONS AND RECOMMENDATIONS

8.1. CONCLUSIONS

In this section the most significant conclusions are summarized. For this study the main objective was to develop a thermodynamic model to simulate the two phase compression with minimal computational time. To achieve this the geometry is kept rather simple and a quick solving method used as well.

After studying various different compressor models during the literature study a few possible models were examined more thoroughly. The end result was that different aspects from a few models should be combined. [Chamoun et al. \[4\]](#) used a simple fixed control volume approach, constant suction and discharge phases and governing equations incorporating leakages during compression. Originally the model consisted mainly of this model, however, in practice there was a converging problem with the governing equations. To correct for this the governing equations presented by [Zaytsev \[26\]](#) were used, while still using the finite control volume approach.

The assumptions from [Chamoun et al. \[4\]](#) were used for the initial run of the compressor, where the suction and discharge phases are assumed to be constant and no leakages included, to acquire values that could be used for mass flow and leakage calculations. [Tang \[19\]](#) had calculated a possible geometry for twin-screw compressor, which also scaled nicely with the geometry used by [Zaytsev](#), which was used as a base for the geometry of the compressor for this study. With this base it was possible to estimate port sizes and leakage paths and how they would scale with the volume curve. The volume curve shape was used the same trend as [Tang](#) and [Zaytsev](#), and was scaled so that the maximum volume corresponded to the maximum volume of the compressor.

With the finite control volume approach the step size needed to be rather small in order for the model to represent stable values. With smaller geometries the compressor model was slightly more unstable and needed even smaller steps in some phases. To start with, the model calibration and troubleshooting was done with the large geometry from [Tang](#). After troubleshooting the geometry was scaled down to the correct size for the studied compressor and then the results from Chapter 5 were computed.

As not much information was available to validate the model different approaches had to be used for validation. [Hillston \[9\]](#) has presented various trends for twin shaft compressors, including the oil free twin screw compressor. While not using the same working fluid nor working in the two phase region it is still viable to compare the trends seen from the data. The efficiency changes over different pressure ratios as well as the discharge temperature for different rotational speeds were compared. For both cases the trend was very comparable, the efficiency had a peak when it is not affected by under or over compression. Also that there is a steady decrease in discharge temperature with higher rotational speeds.

Next the model was used to study the effects of different operating conditions. In Chapter 7 the results were discussed. By looking into the coefficient of performance the optimum ammonia concentration is slightly higher than 30wt%, around 33-35wt% resulted in the highest COP. The estimated clearance size ac-

ording to design should be around 50 micrometer, with increased clearances the efficiency and COP of the compressor decreases. With 200 micrometer clearance the efficiency decreased almost 10% compared the 50 μm clearance. Clearly this has an effect and cannot be controlled after manufacturing, but when those clearances are confirmed the model can be used to estimate more accurate values.

A clear trend can be seen in the suction vapor quality, the higher suction vapor qualities can reach higher pressures without trouble. However, the efficiency decreases steadily with increased vapor quality and just like for the ammonia concentration the COP becomes a parabolic curve. Where after the peak, around 40% vapor quality, the COP decreases quickly for lower qualities while if the quality is higher the decrease is slightly slower. According to this data it is best to keep the vapor quality around 40-50% in order to reach the best compressor performance.

Finally there was some preliminary work done for the experimental setup. Sensors were tested and calibrated where possible. Other components were tested in the setup to make sure the correct variables were being read by the computer. In order to make sure that the inlet conditions for the compressor are as expected a Matlab script was made to estimate how the rest of the cycle would act. This mostly included the separator inlet, the vapor and liquid streams and how they would mix to form the compressor inlet. As long as the vapor quality into the separator is over 30% the quality of the mixture rises a few percentage, with lower inlet quality it tends to decrease slightly. Excessive superheating or subcooling does not have a large influence on the final mixture quality. While it was usually enough to only superheat the mixture a few degrees the necessary subcooling was closer to 70 degrees to ensure safe operation.

8.2. RECOMMENDATIONS

First of all once the compressor has been connected to the experimental setup and all problems solved the compressor model should be validated with experimental data. As for now the model is only validated by comparing trends with other oil free twin screw compressors as there was no experimental data for two phase ammonia vapor flow available. It would be good to test the compressor for all the different property changes, to see if all are working as expected. Such as rotational speed, different suction conditions and different discharge pressures.

When available the model could be updated with more accurate geometry. Such as at what rotational angle the suction and discharge ports open and close, sizes of ports and leakage paths. The size of clearances should be measured if possible to keep accurate values in the model.

For future experimental setups there are a few possible recommendations. If older components are used they should be tested before installation whenever possible. Some times smaller parts decay over time or when not in use, leading to the component possibly not working. This can take quite some time to realize as the installation itself takes time and the problem will not be discovered until after experiments are about to start. If the component can be tested separately, at least partly, that could speed up the troubleshooting process.

Also while the importance of leak proofing the system has been discussed before, to make sure that nothing is escaping the system, it is just as important to make sure nothing can leak into the system that should not be there. This can possibly happen if an inlet valve is not completely tight. However this can be hard to notice as the changes can be very small when the system is ready to operate. The best way to notice is to let the system be empty, after it is leak tight, and watch the pressure or temperatures over some time to see if any unexplainable changes happen.

Finally as there are so many variables that need to be accounted for in experimental setups, and many items that must be ordered or repaired, along with the time needed to physically set up the system. It is always recommended to start as early as possible, aiming to have the system ready a couple months before experiments are expected to start gives two months for troubleshooting, possibly ordering new equipment and making arrangements. With this buffer the experimental time-line should not be effected too much by unavoidable delays.

A

APPENDIX

A.1. COEFFICIENTS USED FOR FREE ENTHALPY METHOD BY MEJBRI AND BELLAGI

In this appendix the coefficients used in the free enthalpy model obtained from [Mejbri and Bellagi](#) are given.

Table A.1: Coefficients used for Gibbs function for pure ammonia and water [14]

Coefficient	H_2O	NH_3
b_1	0.106168	0.120834
b_2	-0.122078	-0.181358
b_3	0.120045	0.174711
c_0	4.010379	4.097430
c_1	0.863163	3.030304
c_2	0.789193	0
θ_1	-3.407465	-4.832867
θ_2	-6.162301	0
a_1	$2.3937 * 10^{-2}$	$3.0971 * 10^{-2}$
a_2	$-3.0015 * 10^{-6}$	$2.3494 * 10^{-6}$
a_3	$-2.7000 * 10^{-2}$	$-3.8196 * 10^{-2}$
a_4	$3.1177 * 10^{-2}$	$4.7007 * 10^{-2}$
β_1	$-7.2839 * 10^{-2}$	$-5.0641 * 10^{-3}$
β_2	3.148082	6.275148
β_3	$-1.3485 * 10^{-4}$	$-1.0099 * 10^{-1}$
β_4	10.33048	2.5100570
β_5	$-6.2708 * 10^{-3}$	$-3.8130 * 10^{-3}$
β_6	6.7679000	6.8581180
τ_0	2.3689350	1.4831370
$p_0(\text{bar})$	$6.1183 * 10^{-4}$	$4.3250 * 10^{-1}$
$\bar{h}_{L,0}(kJmol^{-1})$	$8.6048 * 10^{-6}$	5.8192800
$\bar{h}_{G,0}(kJmol^{-1})$	45.053940	27.327990
$\bar{s}_{G,0}(kJmol^{-1}K^{-1})$	$1.6494 * 10^{-1}$	$1.0365 * 10^{-1}$
$T_c(K)$	647.1	405.4

Table A.2: Coefficients used for excess free enthalpy [14]

i	γ_i
1	4.602295
2	$-4.8937 * 10^{-4}$
3	$-2.4040 * 10^{-4}$
4	-4.124661
5	$-5.5352 * 10^{-3}$
6	$9.8221 * 10^{-4}$
7	$2.2916 * 10^{-3}$
8	$-2.0762 * 10^{-3}$
9	$-1.1837 * 10^{-6}$
10	$3.3508 * 10^{-1}$
11	$-1.4627 * 10^{-4}$
12	$1.1017 * 10^{-5}$
13	$1.4779 * 10^{-2}$
14	$-6.6991 * 10^{-4}$
15	$-2.7568 * 10^{-1}$
16	$-1.1782 * 10^{-5}$
17	$4.7944 * 10^{-1}$
T_b (K)	500

A.2. COEFFICIENTS FOR PATEK AND KLUMFAR CORRELATIONS

In this appendix the exponents and coefficients needed for the five equations obtained from [Patek and Klumfar](#)

Table A.3: Exponents and coefficients for calculating bubble point temperature [16]

i	m_i	n_i	a_i
1	0	0	$0.322302 * 10^1$
2	0	1	$-0.384206 * 10^0$
3	0	2	$0.460965 * 10^{-1}$
4	0	3	$-0.378945 * 10^{-2}$
5	0	4	$0.135610 * 10^{-3}$
6	1	0	$0.487755 * 10^0$
7	1	1	$-0.120108 * 10^0$
8	1	2	$0.106154 * 10^{-1}$
9	2	3	$-0.533589 * 10^{-3}$
10	4	0	$0.785041 * 10^1$
11	5	0	$-0.115941 * 10^2$
12	5	1	$-0.523150 * 10^{-1}$
13	6	0	$0.489596 * 10^1$
14	13	1	$0.421059 * 10^{-1}$

$T_0 = 100$ K $p_0 = 2$ MPa

Table A.4: Exponents and coefficients for calculating dew point temperature [16]

i	m_i	n_i	a_i
1	0	0	$0.324004 * 10^1$
2	0	1	$-0.395920 * 10^0$
3	0	2	$0.435624 * 10^{-1}$
4	0	3	$-0.218943 * 10^{-2}$
5	1	0	$-0.143526 * 10^1$
6	1	1	$0.105256 * 10^1$
7	1	2	$-0.719281 * 10^{-1}$
8	2	0	$0.122362 * 10^2$
9	2	1	$-0.224368 * 10^1$
10	3	0	$-0.201780 * 10^2$
11	3	1	$0.110834 * 10^1$
12	4	0	$0.145399 * 10^2$
13	4	2	$0.644312 * 10^0$
14	5	0	$-0.221246 * 10^1$
15	5	2	$-0.756266 * 10^0$
16	6	0	$-0.135529 * 10^1$
17	7	2	$0.183541 * 10^0$

$T_0 = 100 \text{ K}$ $p_0 = 2 \text{ MPa}$

Table A.5: Exponents and coefficients for calculating the vapour composition [16]

i	m_i	n_i	a_i
1	0	0	$1.98022017 * 10^1$
2	0	1	$-1.18092669 * 10^1$
3	0	6	$2.77479980 * 10^1$
4	0	7	$-2.88634277 * 10^1$
5	1	0	$-5.91616608 * 10^1$
6	2	1	$5.78091305 * 10^2$
7	2	2	$-6.21736743 * 10^0$
8	3	2	$-3.42198402 * 10^3$
9	4	3	$1.19403127 * 10^4$
10	5	4	$-2.45413777 * 10^4$
11	6	5	$2.91591865 * 10^4$
12	7	6	$-1.84782290 * 10^4$
13	7	7	$2.34819434 * 10^2$
14	8	7	$4.80310617 * 10^3$

$p_0 = 2 \text{ MPa}$

Table A.6: Exponents and coefficients for calculating the saturated liquid enthalpy [16]

i	m_i	n_i	a_i
1	0	1	$-0.761080 * 10^1$
2	0	4	$0.256905 * 10^2$
3	0	8	$-0.247092 * 10^3$
4	0	9	$0.325952 * 10^3$
5	0	12	$-0.158854 * 10^3$
6	0	14	$0.619084 * 10^2$
7	1	0	$0.114314 * 10^2$
8	1	1	$0.118157 * 10^1$
9	2	1	$0.284179 * 10^1$
10	3	3	$0.741609 * 10^1$
11	5	3	$0.891844 * 10^3$
12	5	4	$-0.161309 * 10^4$
13	5	5	$0.622106 * 10^3$
14	6	2	$-0.207588 * 10^3$
15	6	4	$-0.687393 * 10^1$
16	8	0	$0.350716 * 10^1$

$h_0 = 100 \text{ kJkg}^{-1}$ $T_0 = 273.16 \text{ K}$

Table A.7: Exponents and coefficients for calculating the saturated vapour enthalpy [16]

i	m_i	n_i	a_i
1	0	0	$0.128827 * 10^1$
2	1	0	$0.125247 * 10^0$
3	2	0	$-0.208748 * 10^1$
4	3	0	$0.217696 * 10^1$
5	0	2	$0.235687 * 10^1$
6	1	2	$-0.886987 * 10^1$
7	2	2	$0.102635 * 10^2$
8	3	2	$-0.237440 * 10^1$
9	0	3	$-0.670515 * 10^1$
10	1	3	$0.164508 * 10^2$
11	2	3	$-0.936849 * 10^1$
12	0	4	$0.842254 * 10^1$
13	1	4	$-0.858807 * 10^1$
14	0	5	$-0.277049 * 10^1$
15	4	6	$-0.961248 * 10^0$
16	2	7	$0.988009 * 10^0$
17	1	10	$0.308482 * 10^0$

$h_0 = 1000 \text{ kJkg}^{-1}$ $T_0 = 324 \text{ K}$

BIBLIOGRAPHY

- [1] Annex, I. I. E. r. S. and Technologies (2014). Application of Industrial Heat Pumps.
- [2] Arbon, I. (1994). *The design and application of rotary twin-shaft compressors in the oil and gas process industry*. Mechanical Engineering Publications.
- [3] Cao, F., Gao, T., Li, S., Xing, Z., and Shu, P. (2011). Experimental analysis of pressure distribution in a twin screw compressor for multiphase duties. *Experimental Thermal and Fluid Science*, 35(1):219–225.
- [4] Chamoun, M., Rulliere, R., Haberschill, P., and Peureux, J.-l. (2013). Modelica-based modeling and simulation of a twin screw compressor for heat pump applications. *Applied Thermal Engineering*, 58(1-2):479–489.
- [5] Dong, J. T. and Lu, R. S. (2012). A five-point stencil based algorithm used for phase shifting low-coherence interference microscopy. *Optics and Lasers in Engineering*, 50(3):502–511.
- [6] Energieonderzoek Centrum Nederland (2017). Nationale Energieverkenning 2017.
- [7] Gudjonsdottir, V., Ferreira, C. A. I., Rexwinkel, G., and Kiss, A. A. (2017). Enhanced performance of wet compression-resorption heat pumps by using NH₃-CO₂-H₂O as working fluid. *Energy*, 124:531–542.
- [8] Heinz P Bloch, A. G. (2006). *Compressors and Modern Process Applications*.
- [9] Hillston, J. (2017). Performance Modelling — Lecture 16 : Model Validation and Verification. (March).
- [10] Itard, L. C. M. (1995). Wet compression versus dry compression in heat pumps working with pure refrigerants or non-azeotropic mixtures . *International Journal of Refrigeration*, 18(7):495–504.
- [11] Lemmon, E. W., Huber, M. L., and McLinden, M. O. (2010). NIST Standard Reference Database 23: Reference Fluid Thermodynamic and Transport Properties-REFPROP, Version 9.0, National Institute of Standards and Technology.
- [12] M. Conde Engineering (2006). Thermophysical Properties of { NH₃ + H₂O } Mixtures for the Industrial Design of Absorption Refrigeration Equipment Formulation for Industrial Use.
- [13] MATLAB (2017). *version 9.3.0 (R2017b)*. The MathWorks Inc., Natick, Massachusetts.
- [14] Mejbri, K. and Bellagi, A. (2006). Modelling of the thermodynamic properties of the water – ammonia mixture by three different approaches. *International Journal of Refrigeration*, 29:211–218.
- [15] O'Neill, P. (1981). The development of the screw compressor and its application in the petrochemical and related industries. *A paper presented to the European Congress Fluid Machinery for the Oil Petrochemical and Related Industries in The Hague on 24th March 1981*.
- [16] Patek, J. and Klomfar, J. (1995). Simple functions for fast calculations of selected thermodynamic properties of the ammonia-water system. *International Journal of Refrigeration*, 18(4):228–234.
- [17] Rattner, A. S. and Garimella, S. (2016). Fast , stable computation of thermodynamic properties of ammonia-water mixtures . *International Journal of Refrigeration*, 62:39–59.
- [18] Shen, J., Xing, Z., Zhang, K., He, Z., and Wang, X. (2016). Development of a water-injected twin-screw compressor for mechanical vapor compression desalination systems. *Applied Thermal Engineering*, 95:125–135.
- [19] Tang, Y. (1995). *Computer Aided Design of Twin Screw Compressors*. PhD thesis, University of Strathclyde.

- [20] Tian, Y., Yuan, H., Wang, C., Wu, H., and Xing, Z. (2017). International Journal of Thermal Sciences Numerical investigation on mass and heat transfer in an ammonia oil-free twin-screw compressor with liquid injection. *International Journal of Thermal Sciences*, 120:175–184.
- [21] Türkmen, Ö. S. (2012). *Design and analysis of a heat pump applied to old apartment buildings*. PhD thesis.
- [22] U.S. Energy Information Administration (2016). International Energy Outlook 2016. Technical Report May.
- [23] U.S. Energy Information Administration (2017). International Energy Outlook 2017 Overview.
- [24] van de Bor, D. M., Infante Ferreira, C. A., and Kiss, A. A. (2014). Optimal performance of compression e resorption heat pump systems. *Applied Thermal Engineering*, 65(1-2):219–225.
- [25] Wu, Y.-r. and Tran, V.-t. (2016). Dynamic response prediction of a twin-screw compressor with gas-induced cyclic loads based on multi-body dynamics Prévission de la réponse dynamique d ' un compresseur bi-vis à des charges cycliques induites par du gaz basée sur la dynamique multi-corps. *International Journal of Refrigeration*, 65:111–128.
- [26] Zaytsev, D. (2003). *Development of Wet Compressor for Application in Compression - Resorption Heat Pumps*. PhD thesis, TU Delft.
- [27] Ziegler, B. and Trepp, C. (1984). Equation of state for ammonia-water mixtures. *International Journal of Refrigeration*, 7(2):101–106.